2019

Electronic Properties of Two-Dimensional Van Der Waals Systems

Yohanes Satrio Gani
William & Mary - Arts & Sciences, gani.satrio8@gmail.com

Electronic Properties of Two-Dimensional van der Waals Systems

Yohanes Satrio Gani

Bandung, West Java, Indonesia

Master of Science, College of William & Mary, 2013
Bachelor of Arts, Institut Teknologi Bandung, 2009

A Dissertation presented to the Graduate Faculty
of The College of William & Mary in Candidacy for the Degree of
Doctor of Philosophy

Department of Physics

College of William & Mary
May 2019

APPROVAL PAGE

This Dissertation is submitted in partial fulfillment of
the requirements for the degree of

Doctor of Philosophy

Yohanes Satrio Gani

Approved by the Committee April 2019

Committee Chair
Associate Professor Enrico Rossi, Physics
College of William & Mary

Associate Professor Seth Aubin, Physics
College of William & Mary

Professor Henry Krakauer, Physics
College of William & Mary

Associate Professor Mumtaz Qazilbash, Physics
College of William & Mary

Dr. David Abergel, Associate Editor
Nature Physics

ABSTRACT

In this dissertation we study the electronic structure of van der Waals systems. A van der Waals systems is a heterostructure in which the different constituents are held together by van der Waals forces. We study two different types of van der Waals systems: van der Waals systems formed by graphene and a monolayer of NbSe2, van der Waals systems obtained by placing graphene nanoribbons on a two-dimensional crystal. For the first type of systems we build a continuous low-energy effective model that takes into account the presence of a twist angle between graphene and NbSe2, and of spin-orbit coupling and superconducting pairing in NbSe2. We then obtain how the superconducting pairing induced by proximity into the graphene layer depends on the twist angle. For the second type of systems we obtain using ab-initio methods the electronic structure of graphene nanoribbons placed on hexagonal boron nitride, and of graphene nanoribbons placed on monolayers of transition metal dichalcogenide. For both cases we show how the electronic structure depends on the stacking configuration.

TABLE OF CONTENTS

ACKNOWLEDGMENTS

I am extremely grateful to my PhD advisor, Dr. Enrico Rossi for his valuable guidance, research inputs, and consistent encouragement that I received during the research work. My research has not been possible without his expertise and experience in the condensed matter field. He also provided many support during the completion of this study. I thank to the committee of my annual review each year, Dr. Seth Aubin, Dr. Henry Krakauer and Dr. Shiwei Zhang for ensuring the progress that I have made each year during my study. I would like to express my deepest appreciation to my thesis committee for generously offering their time, support and guidance throughout the defense, review of this thesis and useful inputs to improve the manuscript. I sincerely thank to my collaborators, Dr. David Abergel, Dr. Eric Walter and Dr. Hadar Steinberg, for the contributions and revision in the research projects. Through their feedback, I can enhance and justify my research works. Special thanks to Dr. Eric Walter for many useful discussion about the first principal calculation. I thank High Performance Computing team (Jayasurya Kanukurthy and Laura Hild) at William & Mary for their help and assistance when I used the computing facility in WM clusters.

I also thank to the students and postdocs in Theoretical Condensed Matter group for great times and discussions. Many thanks to the bible study group ISF, all the prayer and their kindness.

I would like to thank my parents for their advice, love and pray. I am also very grateful to my sisters (Johana, Ina, Ira, and Tassya) for their support. I also thank Yuting, Aunt Helen, Aunt Lucy, and their family.

I present this thesis in honor of my parents and my sisters.

LIST OF TABLES

LIST OF FIGURES

ELECTRONIC PROPERTIES OF TWO-DIMENSIONAL VAN DER WAALS SYSTEMS

CHAPTER 1

Introduction

1.1 Two-Dimensional and van der Waals Heterostructures

Rapid advances in the fabrication of very thin layers down to monolayer thick have allowed the study of new phenomena and opened several new technological opportunities. They also provide the ability to combine layers of different materials with different properties to form heterostructures with unique features.

Graphene is an atom thick layer of carbon atoms in a hexagonal arrangement with unique properties [1]. In graphene, the electrons behave as massless Dirac fermions, a fact that makes graphene an ideal platform to study analogies between relativistic quantum effects and solid state phenomena. The carriers mobility and thermal conductivity in graphene are very high reaching up to $2 \times 10^5 \mathrm{cm}^2\mathrm{V}^{-1}\mathrm{s}^{-1}$ [2] and $(5.30 \pm 0.48) \times 10^3 \mathrm{W/mK}$ [3], respectively. Following the discovery of graphene, there has also been a lot of activity in isolating and studying other two-dimensional materials such as transition metal dichalcogenides (TMD). Monolayer TMDs can exhibit semiconducting or metallic

electronic properties depending on the species of transition metal atom. Some of the main interesting features of these systems arise from the presence of large spin orbit coupling (SOC) and broken inversion symmetry. The monolayer of semiconducting TMDs such as MoS_2 or $MoSe_2$ has a direct band gap between 1 eV and 2 eV making these materials good for solar cell technology applications. Metallic TMDs, such as $NbSe_2$, can exhibits superconductivity at low temperatures. Due to SOC, the superconductivity pairing is very robust against the presence of in-plane magnetic fields.

There is a lot of theoretical work suggesting the existence of topological phases such as the Quantum Spin Hall Effect [4] in graphene. This phase can be realized when a band gap with band inversion, generated for example by the presence of SOC. However, SOC is naturally very weak in pristine graphene with a magnitude on the order of 50 μeV [5]. We can enhance the SOC interaction with the proximity effect by realizing heterostructures composed by graphene and monolayer transition metal dichalcogenides (TMD) [6]. At low temperature, graphene also does not exhibit superconductivity. Hence, it is interesting to see if we can introduce the superconductivity pairing together with SOC interaction in graphene via the proximity effect in graphene-$NbSe_2$ heterostructures.

By exchanging two indistinguishable fermions or bosons, the total wavefunction acquires additional phase π or 2π, respectively. In 2D, it is possible to have particle, anyons, for which the exchange of two particles results in a phase factor $e^{i\theta}$ for the total wavefunction with θ different from π and 2π. One example of anyons are Majorana fermions which are particles that are their own antiparticles. Kitaev [7] showed the emergence of Majorana bound states in a finite spinless one-dimensional chain with p-wave pairing. These Majorana bound states have been proposed as states for encoding information for topological quantum computing [8]. The Kitaev model can be realized in one-dimensional InAs nanowire with strong SOC in proximity of a s-wave superconductor in the presence of an external magnetic field [9]. There are several challenges to realizing Majorana fermions

in these systems, especially due to the presence of several sub-bands [10]. If the required magnetic field is too large, it can also destroy the superconducting pairing in the nanowire.

Motivated by these facts, we suggest an alternative system to host Majorana bound states formed by graphene-nanoribbons and monolayer $NbSe_2$. It is known that graphene can be confined into a one-dimensional periodic system to form graphene nanoribbons (GNR). In a GNR, due to the almost 1D confinement, the higher energy bands are separated from the lowest energy bands with a large energy difference, thus preventing the annihilation of two Majoranas from different sub-bands. However, the spin orbit coupling and superconducting pairing are ingredients that are still missing in pristine GNRs. We can add these ingredients by utilizing monolayer $NbSe_2$ as a substrate for GNRs.

In solids, van der Waals interaction arise due to the correlated fluctuation of the electron polarization which is a non-local and long range correlation. The van der Waals (vdW) force is relatively much weaker compared to other forces for instance ionic or covalent bonding. Because of many body interactions, vdW force is difficult to estimate accurately. A second order perturbation expansion of the Coloumb interaction is often used. However, this approximation does not capture the non-trivial many body effect which can be crucial for real material simulations [11]. There is also a model that describes each nucleus and its electron clouds as a single dipole oscillator. Hence, there is an arrangement of the dipoles in the crystal. The response function of each dipole can be significantly normalized as a result of many body interaction.

The interaction between two dipoles with finite distance R has a leading order term proportional to F/R^6 with F, a constant that depends on the system. The dipole interaction between two carbon atoms gives rise to a binding energy ≈ 46 meV. The hopping energy between two pz orbital of carbon atoms is about 2.5 eV [1] which is much larger magnitude than the vdW energy between two dipoles. Hence, we see that to study the electronic properties, we can neglect this interaction. However, the vdW interaction is

crucial to determine the crystal structure.

The weak vdW interaction between layers of two dimensional vdW systems in heterostructures preserves the electronic properties of the individual layers. This allows the possibility to combine different layer materials to produce some interesting electronic properties. For example, the combination of high carrier mobility of graphene and semiconducting nature of $MoSe_2$ can be engineered to fabricate a high quality photovoltaic device [12].

1.2 Density Functional Theory

Density functional theory (DFT) has been successfully utilized to simulate the electronic structure of molecules and solids. It is an efficient method to investigate the electronic properties of systems such as bandstructure, optical response, binding energy, and work function. Because of this, DFT has become one of the main tools to study the electronic properties of two-dimensional systems. In this section, I give short review about DFT.

Consider the many body Hamiltonian with Couloumb interaction that describes N electrons in a solid crystal.

$$H = \sum_{i=1}^{N} \left[\frac{p_i^2}{2m} - \sum_{R_j} \frac{eQ_j}{|r_i - R_j|} \right] + \sum_{i<j}^{N} \frac{e^2}{|r_i - r_j|} \tag{1.1}$$

The first term is the kinetic energy operator. The second term is the Coulomb interaction V between electrons at position r_i with charge e and the nuclear atoms at position R_j with charge Q_j. This term depends explicitly on the crystal structure being considered. The third term is the electron-electron interaction. We assume that the nuclear atoms are stationary considering their mass is much heavier than the electron's mass (Born-Oppenheimer approximation) so that we can neglect the nuclear kinetic energy.

The many body wavefunctions can be used to obtain all the system's observable such as electron density, polarization, etc. However, finding the wavefunctions is a difficult task and computationally expensive given that the size of Hilbert space increase exponentially with the number of electrons.

DFT offers a solution to this problem by mapping the many body problem with electron-electron interaction U to a single electron problem without U [13]. The key principle is based on the Hohenberg-Kohn theorem which states that the ground state density $n(r)$ will determine uniquely the non-degenerate ground state wavefunction $\Psi(r_1...r_n)$. This also means that the wavefunction can be written as a functional of electron density. It should be noted that this wavefunction has to minimize the energy of the system beside producing the charge density $n(r)$. Hence, the problem can be reformulated to find the corresponding Hamiltonian as a functional of $n(r)$ that minimizes the total energy. This method provides tremendous reduction of computational cost. Further consequence of this theorem is the expectation value of observables will also be functional of ground state density $n(r)$. The system total energy is written as:

$$E[n] = T[n] + U[n] + V[n] \tag{1.2}$$

The ground state can be obtained by minimizing this energy functional of $n(r)$. The challenge is that the functional $U[n]$ is unknown and can only be approximated.

Hence, the orbital wavefunction of the non-interacting particle has to satisfy:

$$\left[-\frac{\hbar^2\nabla^2}{2m} + \frac{\delta(U+V)}{\delta n}\right]\phi(r) = \epsilon\phi(r) \tag{1.3}$$

The orbital wavefunctions can be calculated by finding the solution of this equation. The

new density can be computed by:

$$n(\boldsymbol{r}) = \sum_{1}^{N} |\phi_i(\boldsymbol{r})| \tag{1.4}$$

The steps are repeated until convergence is achieved.

The functional is not known exactly. There has been several approaches to estimate the form by using pertubation theory [14], Quantum-Montecarlo calculation [15], and parametrization [16].

1.3 Superconductivity

A superconducting system exhibits zero electrical resistance at temperatures below some critical temperature (Tc). A superconductor is not a perfect conductor. It can be distinguished by its different behavior under an external magnetic field. In a superconductor, the magnetic field is always expelled showing a perfect diamagnetism (Meissner effect). However, the magnetic field still can penetrate through a perfect conductor.

There are two types of superconductors based on the magnetic properties. We will refer as first and second kind superconductors. For the first kind, the complete magnetic field expulsion (B) is observed for a weak external field (H). Note that the field H can be controlled by varying the external current. When the field H is increased to reach some critical value ($H_C(T)$) with fixed temperature T, the magnetic flux can penetrate the system and the resistivity is not zero anymore. For the second kind, there are two transitions when an external field H is applied to the system. For the field strength in the range $0 \leq H \leq H_{C1}(T)$, the magnetic field and resistance inside the superconductor are still zero. If the field H is increased above $H_{C1}(T)$, the magnetic field can weakly penetrate the superconductor. This magnetic flux appears as vortex states inside the

superconductor. The total magnetic flux for each vortex can only take discrete values $n\frac{hc}{2e}$ where h is the Planck constant, c the speed of light, e the electron charge, and n is some integer. This phase exists for external fields within the range $H_{C1}(T) \leq H \leq H_{C2}(T)$. Above $H_{C2}(T)$, the system goes to a normal state.

Cooper showed that the Fermi sea of the electrons is unstable when there is an attractive potential $U_O < 0$ between two electrons [17]. Even in the limit of weak interaction, the bound state of these electron pairs still exist. One of the possible origin of this attractive interaction is from electron-phonon coupling where the electron-electron interaction can be screened by the positive ions in the lattice. The positive cloud around electron 1 can be attracted by the electron 2 which can contribute to indirect attraction between the two electrons.

The microscopic theory of superconductors was successfully developed by Barden et al [18]. In this theory, the interaction pairs the electrons with opposite spin and momentum. The spins are chosen to be opposite forming a spin singlet in order to satisfy antisymmetric property of fermions as the real space component has an even parity. The interaction hamiltonian to describe the electron pairing can be written as:

$$H_I = \sum_{k_1,k_2} U(k_1,k_2) c^\dagger_{k_1\uparrow} c^\dagger_{-k_1\downarrow} c_{k_2\downarrow} c_{k_1\uparrow} \tag{1.5}$$

The total hamiltonian consist of kinetic term and interaction hamiltonian H_I.

$$H = \sum_{k,\sigma} \epsilon_k c^\dagger_{k,\sigma} c_{k,\sigma} + H_I \tag{1.6}$$

The mean field approach can be used to simplify the interaction term which yields:

$$H_I \approx -\sum_k \left(\triangle^*_k c_{-k\downarrow} c_{k\uparrow} + \triangle_k c^\dagger_k c^\dagger_{-k\downarrow} \right) \tag{1.7}$$

In this equation, we define the gap function $\triangle_k$ as:

$$\triangle_k = -\sum_{k'} U(k,k') < c_{-k'\downarrow} c_{k'\uparrow} > \tag{1.8}$$

where we average the correlation of all electron pairs in the ground state. We also can write the Hamiltonian in Nambu space where the bases are formed by the electron and hole $(c^\dagger_{k\uparrow}, c_{-k\downarrow})$. We also use the fermion commutation rule to change the kinetic energy of spin down electron $\epsilon_k c^\dagger_{k\downarrow} c_{k\downarrow}$ to be $\epsilon_k \left(1 - c_{k\downarrow} c^\dagger_{k\downarrow}\right)$. We will neglect the constant term unless we want to compare the total energy of the system with the normal state. Hence, we can write the total Hamiltonian in matrix notation to be:

$$H = \begin{bmatrix} c^\dagger_{k\uparrow} & c_{-k\downarrow} \end{bmatrix} \begin{bmatrix} \epsilon_k & -\triangle_k \\ -\triangle^*_k & -\epsilon_k \end{bmatrix} \begin{bmatrix} c_{k\uparrow} \\ c^\dagger_{-k\downarrow} \end{bmatrix} \tag{1.9}$$

If we diagonalize this hamiltonian, we will obtain the energy spectrum of the system to be $\pm\sqrt{\epsilon_k^2 + |\triangle_k|^2}$. This means that there is an opening gap on the fermi surface of the system. It is also obvious that the wavefunction will be linear combination of electron and hole.

1.4 Outline

In Chapter 2, we review the electronic properties of the systems that we consider in this work. First, we discuss transition metal dichalcogenides system such as MoS_2 and $NbSe_2$. We also discuss the electronic features of graphene including the spin orbit coupling and topological phase. Then, we introduce graphene nanoribbons.

In Chapter 3, we study heterostructures formed by graphene and $NbSe_2$. We are especially interested in the electronic properties at low temperatures for which $NbSe_2$

becomes a superconductor, robust to external in-plane magnetic fields. In this system, we study the nature of the induced superconducting gap in a graphene layer via the proximity effect. Despite the large lattice mismatch, our calculation shows the robustness of the induced superconductivity pairing on graphene. Moreover, the results of our work address the most pressing questions about graphene-NbSe2 twisted systems: they show for which twist angles, and how strongly, the bands of graphene and NbSe2 hybridize. They also show the amount of spin-orbit coupling and superconducting pairing that graphene inherits due to its proximity to NbSe2. In particular, they show how all of these quantities depend on the twist angle.

In Chapter 4, we investigate the electronic structure of systems composed by graphene nanoribbons (GNR) placed on two-dimensional hexagonal boron nitride (hBN). Hexagonal boron nitride has emerged as the ideal substrate for graphene-based systems, and it is therefore also the natural optimal substrate for systems based on graphene nanoribbons. In this work we systematically study the effect of hexagonal boron nitride as a substrate for graphene nanoribbons. Our results, obtained via ab-initio approaches, quantify the modifications of the GNR energy spectrums and show that for zigzag graphene nanoribbons, hexagonal boron nitride can induce a significant spin-splitting of the conduction and valence bands.

In Chapter 5, we study the heterostructures formed by GNR and monolayer TMD. We consider semiconducting and metallic TMDs as the substrate. By obtaining the electronic structure via ab-initio calculations, we assess the magnitude and stacking dependence of the induced SOC on GNRs. Our results also demonstrate the potential of these heterostructures to become a new platform for realizing Majorana fermions.

CHAPTER 2

Review of Two-Dimensional and One-Dimensional Systems

2.1 Transition Metal Dichalcogenides

2.1.1 MoS_2

A single layer MoS_2 has a hexagonal crystal structure formed by a single layer plane of Mo atoms between two layer planes of S atoms. Each Mo atom is coordinated by six S atoms in a trigonal prismatic geometry. The primitive cell consists of one Mo atom and two S atoms. We take the out of plane direction along the z axis. Hence, the MoS_2 plane is parallel to xy plane. The symmetry group of the crystal is D^1_{3h} with trigonal rotation symmetry C_3, reflection by yz plane σ_v and reflection by xy plane σ_h. The experimental lattice constant of the hexagonal plane or magnitude of primitive bases vectors $\boldsymbol{a_1}$ and $\boldsymbol{a_2}$ shown in Fig.2.1 in bulk MoS_2 is 3.16Å [19]. The vertical distance between two neighbor Mo planes h is about 6.14 ± 0.01Å. The thickness of the primitive cell c is approximated to be 2h.

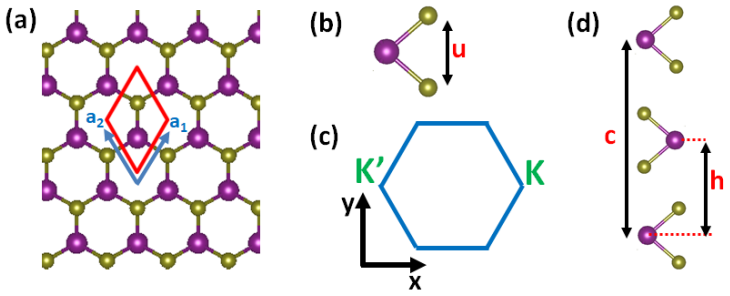

FIG. 2.1: (a) shows the structure of monolayer MoS_2 seen from out of plane axis (z). Mo and S atoms are represented by purple and brown color, respectively. The primitive translation vectors are denoted by $\boldsymbol{a_1}$ and $\boldsymbol{a_2}$. The primitive cell is given by red parallelogram. (b) shows the atoms within the primitive cell. (c) shows the first Brillouin Zone (BZ) in the reciprocal lattice vector space. (d) layers of atoms in bulk MoS_2 in 2H structure.

The MoS_2 monolayer is a semiconductor with a direct band gap about 1.8 eV [20, 21]. The low energy bands are positioned at the corner of its hexagonal brillouin zone (valley K/K'). The maximum valence band (MVB) and minimum conduction band (MCB) are located at these two valleys K $\left(\frac{4\pi}{3a}[1,0]\right)$ and K' $\left(-\frac{4\pi}{3a}[1,0]\right)$. The second maximum of the valence band is located at Γ point. The second minimum of the conduction band is at Q $\left(\frac{2\pi}{3a}[1,0]\right)$ located between $\Gamma - K$ path. In the multilater or bulk structure, MoS_2 exhibits a transition to an indirect band gap semiconductor [22, 23]. The energy gap is also reduced to 1.3 eV in the bulk from the experimental data [20]. The interlayer coupling between the p_z orbital from the S atoms of the adjacent layers raises up the energy of the valence band second maximum at Γ [23]. In addition, the conduction band second minimum at Q is also lowered in energy as the number of layers increases. The transition from direct bandgap in the monolayer to indirect bandgap in the bulk is exemplified in Fig. 2.2. Note that the bandstructures are calculated using DFT with Perdew-Burke-Ernzerhof (PBE) functional [24] which underestimates the bandgap for MoS_2 bulk [25].

The inversion symmetry is broken in monolayer structure as the sublattices are occupied by two different atoms. This lack of inversion symmetry results in a strong spin

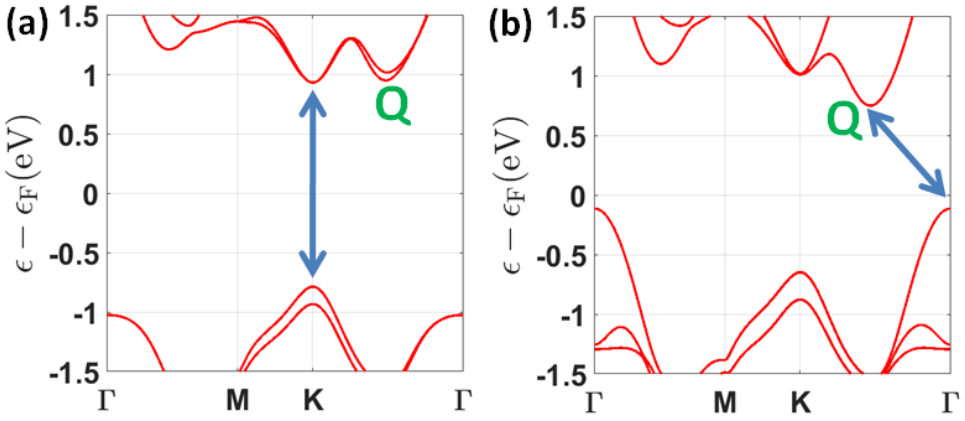

FIG. 2.2: Bandstructure of MoS_2 for monolayer (a) and bulk structure (b).

orbit coupling with the spin splitting energy about 150 meV at the MVB of each valley. The time reversal symmetry dictates that the two degenerate valleys K and K' have opposite spin structure with respect to each other, indicating the coupling between spin and valley. Moreover, the z component of the angular momentum of the electron occupying the valence and conduction bands have an opposite value between valley K and K'. As a consequence, it is possible to control the electronic excitation at the particular valley by optical pumping using circular polarized light [26].

The effective low energy band hamiltonian for valley K and K' can be built by using the d and p orbital atomic wavefuntions from Mo and S atoms as the bases. The Mo atom has five d orbitals for instance: $d_{z^2}, d_{x^2-y^2}, d_{xy}, d_{xz}, d_{yz}$. The hybridization is only allowed between d_{z^2} and $d_{x^2-y^2}, d_{xy}$ due to the reflection symmetry in z direction. This hybridization causes an opening of the band gap at both valley K and K' [27]. The MVB orbital characters are mostly from $d_{x^2-y^2}$ and d_{xy} orbital of Mo mixed with p_x and p_y orbital of S. The MCB is mainly constructed by d_{z^2} and a small percentage of pz orbital.

From C_{3h} symmetry, the effective hamiltonian for the low energy bands at valley K

or K' can be formulated below [27]:

$$\hat{H} = at\left(\tau k_x \hat{\sigma}_x + k_y \hat{\sigma}_y\right)\hat{s}_0 + \frac{\triangle}{2}\hat{\sigma}_z \hat{s}_0 - \lambda\tau\frac{\hat{\sigma}_z - 1}{2}\hat{s}_z \tag{2.1}$$

The bases of this hamiltonian are $|d_{z^2}>$ and $\frac{1}{\sqrt{2}}\left[|d_{x^2-y^2} + i\tau|d_{xy}>\right]$ with $\tau = \pm$ corresponding to valley K and K'. $\hat{\sigma}$ denotes the Pauli matrices for these two bases functions. The parameter lattice constant a, effective hopping t, energy gap $\triangle$, and SOC potential λ can be determined by fitting the bands with a DFT calculation. This effective hamiltonian, excluding the SOC potential, has a similar structure to graphene's Dirac hamiltonian with a staggered sublattice potential that can be introduced by stacking graphene on hBN substrate. The first term represents the kinetic term and is similar structure with the Dirac bands of graphene. The second term causes the energy gap between MVB and MCB. The hybridization between d_{z^2} and $(d_{x^2-y^2}, d_{xy})$ states results in the potential energy difference between these states. The last term is the SOC term which has a finite amount only for the valence band.

When an in-plane electric field is applied to the monolayer MoS_2, the charge will flow transversely to the field. The charge is moving in the opposite direction for the opposite valley. We can explain this by examining the electron velocity of the Bloch states. It is known that the electron velocity [28] can be written as:

$$\boldsymbol{v}_n(\boldsymbol{k}) = \frac{\partial\epsilon_n(\boldsymbol{k})}{\hbar\partial\boldsymbol{k}} - \frac{e}{\hbar}\boldsymbol{E}\times\boldsymbol{\Omega}_n(\boldsymbol{k}) \tag{2.2}$$

with n stands for the band index. The first term corresponds to the group velocity of the Bloch states wave packet. In an insulator, this term will have zero contribution to the electric current as we integrate out all the states in the Brillouin zone (BZ). The second term is geometry dependent, and uniquely determined by the material with $\boldsymbol{\Omega}_n(\boldsymbol{k})$, defined

as a Berry curvature [28, 29, 30]. This term can be calculated for the Bloch states [31] by:

$$\boldsymbol{\Omega}_n(\boldsymbol{k}) = i < \nabla_{\boldsymbol{k}} u_n(\boldsymbol{k})| \times |\nabla_{\boldsymbol{k}} u_n(\boldsymbol{k}) > \tag{2.3}$$

with $u_n(\boldsymbol{k})$ is the periodic part of the Bloch wave function for band n. We see that the second term always contributes to the velocity in a transversal direction to the applied electric field. Now, if we consider a system with time reversal symmetry, it requires the transformation $\boldsymbol{v}_n(-k) = -\boldsymbol{v}_n(k)$ and $\boldsymbol{k} \rightarrow -\boldsymbol{k}$ while electric field is constant under time reversal operation. With these relations, the Berry curvature has to satisfy:

$$\boldsymbol{\Omega}_n(-\boldsymbol{k}) = -\boldsymbol{\Omega}_n(\boldsymbol{k}) \tag{2.4}$$

for the system with time reversal symmetry. We also can deduce the property for a system obeying inversion symmetry where we have $\boldsymbol{v}_n(-k) = -\boldsymbol{v}_n(k)$, $\boldsymbol{k} \rightarrow -\boldsymbol{k}$, and $\boldsymbol{E} \rightarrow -\boldsymbol{E}$. This gives:

$$\boldsymbol{\Omega}_n(-\boldsymbol{k}) = \boldsymbol{\Omega}_n(\boldsymbol{k}) \tag{2.5}$$

for system with inversion symmetry. Therefore, the Berry curvature will be zero in a system satisfying both time reversal symmetry and inversion symmetry. On the contrary, the inversion symmetry is broken in monolayer MoS_2 which gives non-zero magnitude of Berry curvature. We also see from Eq.2.4 that the magnitude of the Berry curvature at valley K and K' is opposite to each other as the time reversal symmetry holds. From this relation too, we can see that the Berry curvature at Γ is zero. The Berry curvature within the first BZ of MoS_2 has been calculated using first principle calculation by Feng et al [32].

Large spin orbit coupling, time reversal symmetry and broken inversion symmetry in MoS_2 also can lead to a spin current, which is the net flow of spin transport [27]. In a normal metal, the spin current is usually zero as the spin up and spin down electrons move

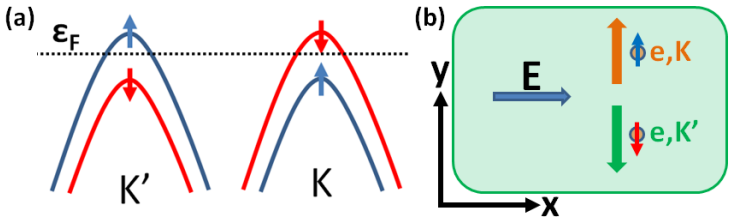

FIG. 2.3: (a) shows the Fermi energy is set to intersect the valence band to have full filled band for the higher valence bands. (b) the transversal spin current emerges when the in-plane electric field is applied. The electron propagates transverse to the field and in opposite direction between the two valleys.

in the same direction. It is possible to have a non-zero total spin current in MoS_2 by tuning the Fermi level of the system. Figure 2.3(a) shows a Fermi level that is set to be between two valence bands on each valley producing half filling for the lowest valence bands and full occupation for the higher valence bands. As a consequence, we will have more particular spin concentration at each valley. When we apply the in-plane electric field, the carriers from opposite valley will have transversal velocity in the opposite direction. The spin down of valley K' and spin up of K carriers dominate the flow of this transversal current giving finite spin current conductivity.

2.1.2 $NbSe_2$

We can replace the transition metal atom from group VI to V of the atomic periodic table to form metallic TMD material such as $NbSe_2$. The crystal structure of monolayer $NbSe_2$ is similar with MoS_2 depicted in Fig. 2.1(a) and (b). The bandstructure for the monolayer $NbSe_2$ is given in Fig. 2.4(a). There is a spin splitting with the maximum value about 155 meV at valley K and K' caused by SOC and broken inversion symmetry. The spin splitting at Γ is zero due to the time reversal symmetry. There are several pockets at the Fermi level constructing the Fermi surfaces located around Γ, K, and K' shown in Fig. 2.5(a). We see the trigonal shape of the Fermi surfaces around valley K and K'. The

orbital character around valley K and K' are from $d_{x^2-y^2}$ and d_{xy} orbital of Nb atoms. Meanwhile, the orbital character in pocket Γ is from d_{z^2} of Nb atoms.

When we add one more layer to form a bilayer system, the inversion symmetry is reproduced. As a result, the bands become spin degenerate. So in general, when we have an odd number of layers, the inversion symmetry is broken causing the spin splitting on the bands. Figure 2.4(a-d) show the bandstructure for 1 layer through 4 layers $NbSe_2$. We see that there will be more bands at the Fermi level associated with these layers. Moreover, the p_z orbital band energy below the highest valence band is increasing toward the Fermi level at Γ. When we have bulk structure, this p_z derived band will cross the Fermi level as shown in Fig. 2.4(e). Hence, in bulk $NbSe_2$, the low energy bands are formed by the p_z orbital of Se atoms and d orbital of Nb atoms constructing several pockets centered at Γ, K, and K' within the Brillouin Zone (BZ) shown in Fig. 2.5. From this figure, we see that pz orbital contributes to a pocket with ($k_z = 0$) and an ellipsoid Fermi surface (pancake) with $k_z \neq 0$ center at Γ.

When we lower the temperature down below the critical point, bulk $NbSe_2$ will become a superconductor with several gap values as an indication of the multiband nature in this system. The mechanism of the SC gap is still questionable. Multigap superconductivity in a bulk $NbSe_2$ was studied using tunneling measurement along different crystal orientation by Noat [33]. They investigated the tunneling conductance of $NbSe_2$ when it was placed with the a/b axis (parallel plane) orthogonal or parallel to the metallic tip where the current flow. By controlling the relative position to the tip, they probed the low energy band that contributed to the conductance. They observed two different gaps with different values. These results obviously show the nature of multigap superconductor in the bulk $NbSe_2$. The $\frac{dI}{dV}$ curve was perfectly fitted within McMillan model [34] suggesting the mechanism of two gaps carried out by the quasiparticle interband scattering. One of the main questions is the identification of the bands associated with these gaps. By analyzing

density of states (DOS) results from tunneling STM images [33], they proposed a three bands model to explain the nature of the two gap superconductor in the bulk $NbSe_2$. So in this model, not only did they allow the scattering between d bands at pocket K and Γ, but they also included the scattering to pz band at pocket and pancake Γ. The supporting argument is the charge density wave can connect the d band in pocket K to pz band at Γ which occurred in $NbSe_2$ with a critical temperature of about 30 K [35].

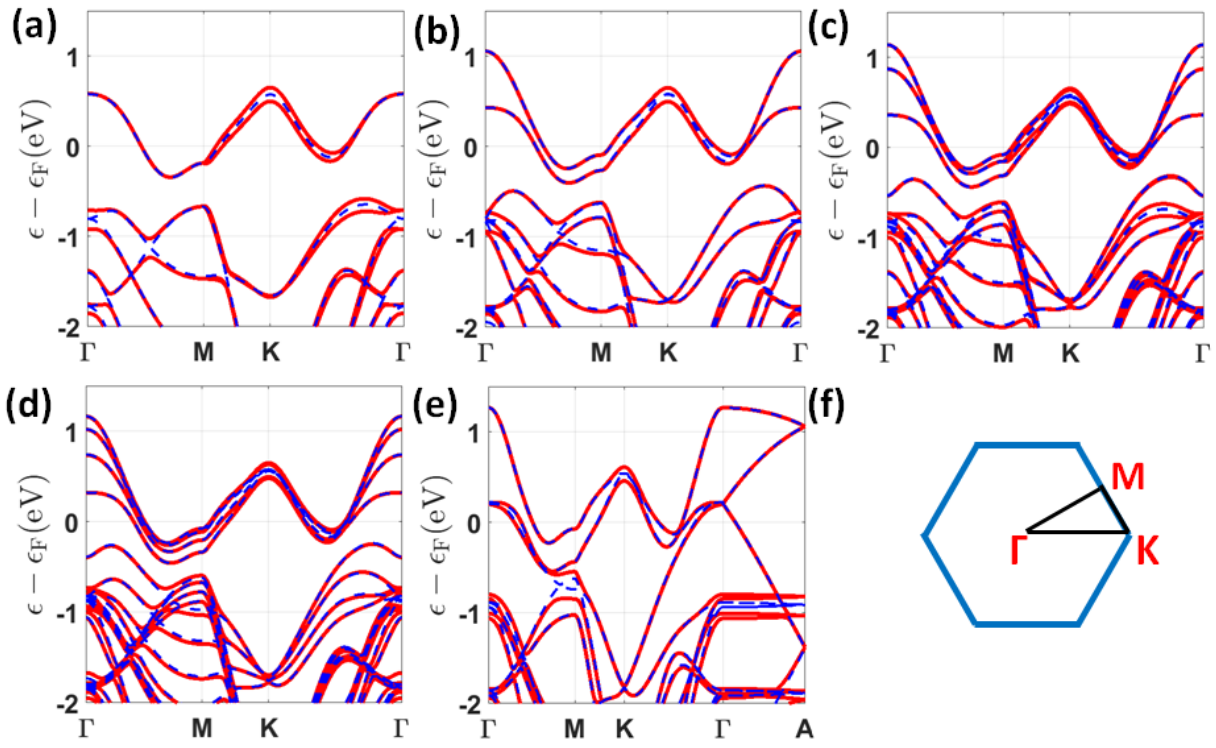

FIG. 2.4: Bandstructure of $NbSe_2$ are given in (a) for 1 layer, (b) for 2 layers, (c) for 3 layers, (d) for 4 layers, and (e) for bulk. Red(solid) and blue (dash) lines are corresponding to bands calculated using SOC and non-SOC pseudopotential, respectively. (f) shows the first BZ of multilayer $NbSe_2$.

The role of pz or d orbital derived bands in the bulk or multilayer $NbSe_2$ is still questionable since another experimental work suggests a different interpretation. From the tunneling experiment on Normal-Insulator-Superconductor tunnel junction [36] comprised

of 2H-$NbSe_2$ (normal metal), MoS_2 (the insulating barrier), and multilayer $NbSe_2$ (superconductor), the smaller gap is identified from pz orbital of Se derived bands. Without an external magnetic field, Dvir et al [36] demonstrate that the two-band model [34] gives good curve fitting to differential conductance $\frac{dI}{dV}$ data. When the number of layers is reduced to four or three layers from the bulk structure, the superconducting gap also decreases. Furthermore, to determine the corresponding band associated with each SC gaps, the in-plane magnetic field is applied to the system. Hence, the McMillan equation is modified to include the orbital depairing due to magnetic field through Abrikosov-Gor'kov depairing parameter Γ^{AG} [37]. This parameter can be determined by fitting to the experimental data which provides information about diffusion coefficient D via $\Gamma^{AG} = \frac{De^2H_{||}^2d^2}{6\hbar c^2}$. The calculated value of the diffusion coefficient in the three layer device yields a large Fermi velocity that leads the identification of Se derived Γ band associated with the smaller gap. We also see that the orbital depairing is proportional to the layer thickness d implying smaller value for three or four layer device comparing to the bulk value. However, they still observe a quite large value for the larger gap in the thin layer device. The reasonable explanation is the Ising SOC emerging on the thin layer device gives the depairing parameter to be $\Gamma^{AG} \approx 2\mu_B \frac{H_{||}^2}{H_{SO}}$ with H_{SO} as the effective magnetic field due to Ising SOC.

We see that these experiments give two different interpretations in the determination of the band corresponding to the smaller gap in the bulk or multilayer $NbSe_2$. However, DFT calculation suggest the pz derived band has higher energy for thinner layer suggesting the smaller gap might not be associated with the Se derived band for thin-layer $NbSe_2$. This is in contrast with the interpretation given by Dvir et al [36].

For monolayer $NbSe_2$, things become simplified as the Se derived band has energy far from the Fermi level. In this system, pocket K and Γ are constructed by the d orbital of Nb atoms. The broken inversion symmetry and strong SOC from Nb atom create strong Ising SOC which lock the spin out of plane direction. This can be pictured by recalling

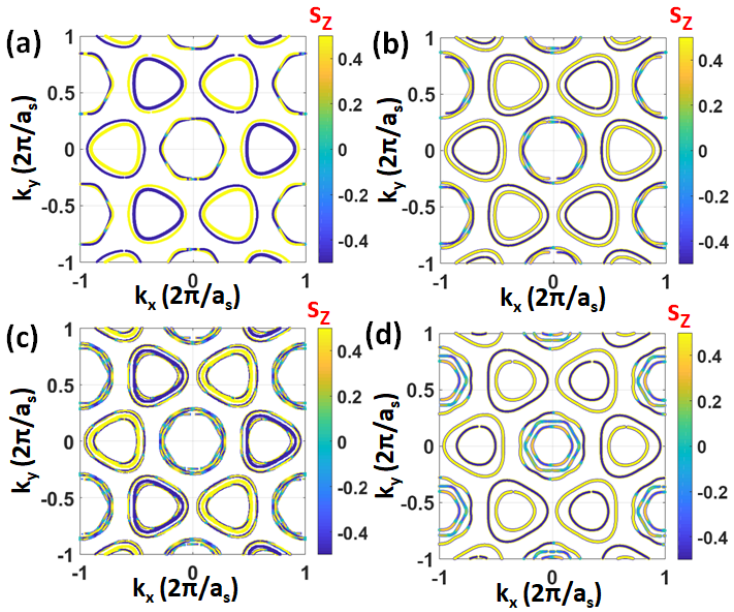

FIG. 2.5: The fermi surface of $NbSe_2$ are given in (a) for 1L, (b) for 2L, (c) for 3L, and (d) for bulk. Note that we show the fermi surface with $k_z = 0$ for bulk system. The corresponding spin projection along z axis are also shown.

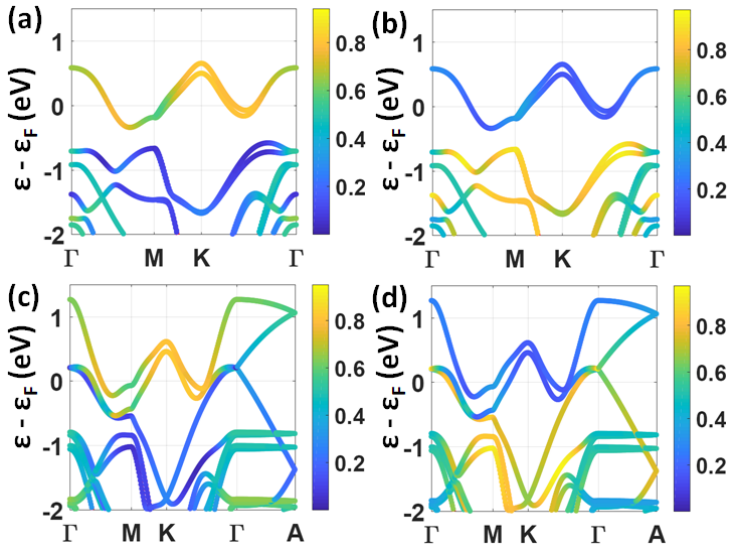

FIG. 2.6: The projection to Nb atoms and Se atoms are given by the left and right panels. (a-b) are for monolayer $NbSe_2$. (c-d) are for bulk $NbSe_2$.

SOC is proportional to $\vec{k} \times \vec{E}$ where $\vec{k}$ is the Bloch momentum and $\vec{E}$ is the electric field experienced by this electron. The electric field is restricted to the plane due to mirror symmetry along z direction especially for the electron near Nb atoms forming the low energy band. Hence, we can regard this SOC as a strong effective magnetic field along z direction, since H_{SO} couples to the Bloch momentum illustrated in Fig. 2.7. Similar with the Zeeman interaction, the electron spin will be aligned in the direction of the magnetic field. Pocket K and K' also have opposite effective magnetic field directions resulting in opposite spin structures between these valleys. From DFT calculation, the spin splitting at K is about 155 meV. The spin splitting energy is becoming smaller for k away from K. Time reversal symmetry dictates the spin degeneracy is protected at the symmetry point Γ leading to zero spin splitting energy. Away from this point, the splitting energy is slowly increasing.

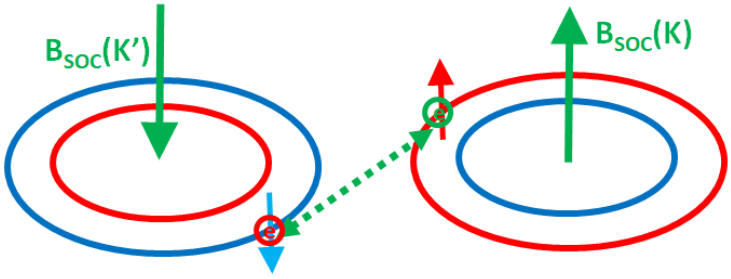

FIG. 2.7: The illustration of Ising pairing in $NbSe_2$ is shown. We see the Fermi surfaces of monolayer $NbSe_2$ at K(right) and K' (left). The SOC splits the spin up and spin down Fermi surface. We see the pairing is between the electrons from opposite valley, spin, and momentum. The SOC interaction can be represented as an effective magnetic field parallel to the z axis with momentum dependence. The direction of the effective magnetic field is opposite between two valleys.

In an isotropic BCS superconductor, the critical magnetic field (H_p) at zero temperature can destroy the pairing when the Zeeman splitting energy matches the superconducting gap, known as the Pauli paramagnetic limit $\mu_B H_p = \triangle$. It should be noted that this is valid when the orbital effect is negligible. Due to the strong Ising SOC, the superconduc-

tivity pairing in monolayer $NbSe_2$ is persistent under strong in-plane magnetic field. We can roughly estimate the critical field by calculating the shift of energy difference between spin up and spin down. Suppose the Hamiltonian that model the electron at valley K can be written as $H = E\sigma_0 + V_{SOC}\sigma_z + \mu_B H_{||}\sigma_y$ with σ as the Pauli matrix in the spin space. The first term is the kinetic part, the second term is the Ising SOC part, and the third term is the Zeeman effect with the in-plane magnetic field along the y axis. Then, by diagonalization, the Zeeman splitting energy is equal to $\frac{2\mu_B^2 H_{||}^2}{2V_{SOC}}$. Therefore, the critical field can be found to be $H_{||} \approx \sqrt{\frac{V_{SOC}}{\mu_B} H_p}$. From the temperature dependence of four point resistance measurements [38], the critical in-plane magnetic field in monolayer can reach up to 31.5 T, which is about 5 to 6 times the Pauli limit.

2.2 Graphene

2.2.1 Low Energy Bands

The primitive bases vectors for the triangular structure are denoted by $\boldsymbol{a_1} = a_g e^{i\pi/3}$ and $\boldsymbol{a_2} = a_g e^{i2\pi/3}$. The corresponding primitive vector in the reciprocal space can be calculated to be $\boldsymbol{b_1} = \frac{4\pi}{\sqrt{3}a_g} e^{i\pi/6}$ and $\boldsymbol{b_2} = \frac{4\pi}{\sqrt{3}a_g} e^{i5\pi/6}$. We will see below that the Dirac bands are positioned at the six corner of BZ of hexagonal structure:

$$\boldsymbol{K_n} = \alpha_1(n)\boldsymbol{b_1} + \alpha_2(n)\boldsymbol{b_2} \tag{2.6}$$

$$\alpha_1(n) = \frac{1}{3}\cos\left(\frac{n\pi}{3}\right) + \frac{1}{\sqrt{3}}\sin\left(\frac{n\pi}{3}\right) \tag{2.7}$$

$$\alpha_2(n) = -\frac{1}{3}\cos\left(\frac{n\pi}{3}\right) + \frac{1}{\sqrt{3}}\sin\left(\frac{n\pi}{3}\right) \tag{2.8}$$

with $n = 0, 2, 4$ for valley K and $n = 1, 3, 5$ for valley K'.

The low energy band of graphene can be modeled accurately within tight binding

approximation with pz orbital serving as the basis wavefunction. The primitive cell is constructed by two carbon atoms occupying different sites which we will denote here as sublattice A and sublattice B with their position:

$$\boldsymbol{d}_A = 0 \tag{2.9}$$

$$\boldsymbol{d}_B = \frac{1}{3}\boldsymbol{a_1} + \frac{1}{3}\boldsymbol{a_2} \tag{2.10}$$

The pz orbital from each carbon atom hybridized in π bonding with the nearest neighbor carbon atoms where the hopping energy t about 2.8 eV [39]. Hence, the electron creation and annihilation operator at position R can be expressed as $c^{\dagger}_{\tau\sigma}(R)$ and $c_{\tau\sigma}(R)$ with τ and σ denoting the sublattice (A/B) and spin index. When we restrict the hopping only to the nearest neighbor, we can write the Hamiltonian for graphene as:

$$H_G = \sum_{R,\delta_i,\sigma} t c^{\dagger}_{B,\sigma}(\boldsymbol{R} + \boldsymbol{\delta_i}) c_{A,\sigma}(\boldsymbol{R}) + h.c. \tag{2.11}$$

$\boldsymbol{\delta_i}$ is a vector connecting to the nearest primitive cell with the value $(0, -\boldsymbol{a_1}, -\boldsymbol{a_2})$ for index i range from 1 to 3.

The hamiltonian in Eq. 2.11 can be diagonalized in the reciprocal space as a consequence of the translation invariance in the periodic structure which implies Bloch momentum k is a good quantum number. Hence, we perform the transformation from r to k space governed by:

$$\begin{aligned} c^{\dagger}_{\tau\sigma}(\boldsymbol{R}) &= \frac{1}{\sqrt{N}} \sum_{\bar{\boldsymbol{k}}} e^{-i\bar{\boldsymbol{k}}\bullet(\boldsymbol{R}+\boldsymbol{d_\tau})} c^{\dagger}_{\tau\sigma}(\bar{\boldsymbol{k}}) \\ c_{\tau\sigma}(\boldsymbol{R}) &= \frac{1}{\sqrt{N}} \sum_{\bar{\boldsymbol{k}}} e^{i\bar{\boldsymbol{k}}\bullet(\boldsymbol{R}+\boldsymbol{d_\tau})} c_{\tau\sigma}(\bar{\boldsymbol{k}}) \end{aligned} \tag{2.12}$$

$\bar{\boldsymbol{k}}$ is the Block momentum relative to the origin Γ. Substituting this transformation leads

to the hamiltonian formulation in the k space:

$$H_G = t \sum_{\bar{\boldsymbol{k}},\sigma} e^{-i\bar{\boldsymbol{k}}\bullet\boldsymbol{d_B}} \left(1 + e^{i\bar{\boldsymbol{k}}\bullet\boldsymbol{a_2}} + e^{i\bar{\boldsymbol{k}}\bullet\boldsymbol{a_3}}\right) c^{\dagger}_{B\sigma}(\bar{\boldsymbol{k}}) c_{A\sigma}(\bar{\boldsymbol{k}}) \tag{2.13}$$

Most of the observable electronic properties of graphene can be associated with the electron dynamics in the low energy band. This motivates us to expand the hamiltonian, given above, around the valley K and K' where the low energy band is located. Within the first BZ, we have seen that there are six valleys which three valleys are associated with K and the remaining three valleys are associated with K'. We usually can choose one for each type valleys n = 0 (K) and n = 3 (K') to represent the complete bases for the electron at the low energy. In this particular case, we will also need the expansion around other valleys for instance in the discussion of incommensurate system. Hence, the expansion of Eq. 2.13 around these valleys yields:

$$H_G(\boldsymbol{K_n} + \boldsymbol{k}) = -v_g \begin{bmatrix} 0 & e^{-i\phi_n}\left(\xi_n k_x - i k_y\right) \\ e^{i\phi_n}\left(\xi_n k_x + i k_y\right) & 0 \end{bmatrix} \otimes \sigma_0 \tag{2.14}$$

with Fermi velocity of graphene $v_g = \frac{\sqrt{3}}{2} a_g t$.The matrix in the first term of the right hand side is written in the sublattice (A/B) space. σ_0 is Pauli matrix in the spin space indicating the spin degeneracy on the bands. ξ_n has value +1 for K (n = 0,2,4) and -1 for K' (n = 1,3,5). Note that there is a phase dependence $e^{i\phi_n}$ on the hamiltonian coming from the expansion of $e^{-i\bar{\boldsymbol{k}}\bullet\boldsymbol{d_B}}$ in Eq. 2.13 with $\phi_n = \frac{4\pi}{3\sqrt{3}} \sin\left(\frac{n\pi}{3}\right)$.

Common choice of the valley to represent the electron at the low energy are n = 0 for $K\left(\frac{4\pi}{3a_g}, 0\right)$ and n = 3 for $K'\left(-\frac{4\pi}{3a_g}, 0\right)$. For these two valleys, we can write their low

energy hamiltonian as:

$$H_{G,K}(\boldsymbol{k}) = -v_g(\boldsymbol{\tau} \bullet \boldsymbol{k}) \otimes \sigma_0 \tag{2.15}$$

$$H_{G,K'}(\boldsymbol{k}) = v_g(\boldsymbol{\tau}^* \bullet \boldsymbol{k}) \otimes \sigma_0 \tag{2.16}$$

where $\boldsymbol{\tau}$ is Pauli matrices in sublattice space. It is obvious that the hamiltonian in Eq. 2.11 preserves time reversal symmetry. Hence, we see that these two hamiltonians in Eq. 2.15 and Eq. 2.16 are related to each other by time reversal symmetry. If time reversal operator is denoted by $\boldsymbol{\theta}$, then we can check that $-\boldsymbol{\theta} v_g(\boldsymbol{\tau} \bullet \boldsymbol{k})\boldsymbol{\theta}^{-1} = v_g(\boldsymbol{\tau}^* \bullet \boldsymbol{k})$ holds.

By diagonalizing the hamiltonian in Eq. 2.15 and Eq. 2.16, the low energy band is formed by two cones where their vertices meet at a point on each valley. This intersection point is usually called as a Dirac point. The energy dispersion of these cones has linear dependence with respect to momentum k:

$$\epsilon_{\pm}(k) = \pm v_g k \tag{2.17}$$

with $\pm$ referring to the conduction and valence bands. We see that graphene is a semimetal with zero band gap and zero density of states at Fermi level. The eigenfunctions will have two components (spinor) in the sublattice space which is commonly called a pseudospin. They can be expressed as:

$$\psi_{\xi,\pm}(k) = \frac{1}{\sqrt{2}} \begin{bmatrix} \pm e^{-i\xi\theta(k)/2} \\ -\xi e^{i\xi\theta(k)/2} \end{bmatrix} \tag{2.18}$$

ξ has value +1 or -1 for the states at K and K', respectively. $\theta(k)$ is the angle between momentum k and the x axis given by $\tan(\theta(k)) = k_y/k_x$. Anologous to the spin, we also can define pseudospin operators τ_x, τ_y, τ_z as Pauli matrices in pseudospin space. If we

calculate the expectation value of this operator $< \psi|\tau_i|\psi >$ for the eigenfunctions given in Eq. 2.18, we obtain two different pseudospin chiralities between valley K and K':

$$< \psi_{\xi,\nu}(k)|\tau_x|\psi_{\xi,\nu}(k) > = -\xi\,\nu\cos\theta(k) \tag{2.19}$$

$$< \psi_{\xi,\nu}(k)|\tau_y|\psi_{\xi,\nu}(k) > = -\xi\sin\theta(k) \tag{2.20}$$

$$< \psi_{\xi,\nu}(k)|\tau_z|\psi_{\xi,\nu}(k) > = 0 \tag{2.21}$$

with $\nu = \pm$ for conduction and valence band, respectively.

The chiral electrons can have unique propagation through potential barrier which is different from a regular electron in two dimensional electron gas. If the scattering from the barrier prohibits intervalley mixing, the electron can tunnel through the barrier without being reflected at normal incidence. Suppose the barrier is modeled as a constant potential along yz plane for $x > 0$. At valley K, the electron with momentum $\boldsymbol{k} = k_x\hat{i}$ is moving to the left as its group velocity $v = d\epsilon/dk$ is negative. In contrast, the electron with momentum $\boldsymbol{k} = -k_x\hat{i}$ is moving to the right toward the barrier. Note that these two electrons have opposite pseudospins. The barrier is preserving the pseudospin if it is proportional to τ_0 which is true for a constant potential. Hence, we see that the backscaterring is prohibited in this case this is commonly known as Klein tunneling [39].

2.2.2 Spin Orbit Coupling in Graphene

Previous studies using TB and DFT reveal that small finite gap at Dirac point can emerge with the range from 1μeV to 200μeV [4, 40, 41, 42, 43, 5]. The main mechanism that responsible to this small gap is the intrinsic spin orbit interaction (SOI) originally from the carbon atom. In addition to the time reversal symmetry, graphene has an inversion symmetry with the symmetry axis at the center of hexagon. As a consequence, the bands

are spin degenerate even in the presence of intrinsic SOC. Konschuh et al [5] demonstrated using tight binding (TB) model with s, p (p_x, p_y, p_z) and d (d_{xz}, d_{yz}) orbital as the bases can lead to correct an estimation SOC strength with the form given by:

$$V^{SOC}_{\gamma,\mu,\nu} = \zeta_\gamma < \vec{L} \bullet \vec{\sigma} > \tag{2.22}$$

$\vec{L}$ and $\vec{\sigma}$ are the angular momentum and spin operator, respectively. ζ_γ is the SOC parameter that depends on the type of orbital γ(s,p,d). It should be noted that p_z orbital do not hybridize with p_x, p_y, and s orbital due to symmetry argument unless SOI is introduced in the system. These orbitals p_x, p_y, and s hybridize with each other to form σ bands which are responsible for the mechanical properties of graphene [44]. The d orbitals which hybridize with p_z are only d_{xz}, d_{yz} since they have the same parity, this only as long the kinetic and crystal field operator do not change the parity. Their model [5] yields an effective intrinsic SOC term for the electron at Dirac bands:

$$V^{\mathrm{SOC}} = \frac{i\lambda_I}{3\sqrt{3}} \sum_{<<j,l>>} \sum_{\tau\sigma_1\sigma_2} \chi_{j,l} c^\dagger_{\tau\sigma_1}(R_j) \sigma^z_{\sigma_1\sigma_2} c_{\tau\sigma_2}(R_l) \tag{2.23}$$

$$V^{\mathrm{SOC}}(k) = \lambda_I \xi \sum_{\tau_1\tau_2} \sum_{\sigma_1\sigma_2} \tau^z_{\tau_1\tau_2} \sigma^z_{\sigma_1\sigma_2} c^\dagger_{\tau_1\sigma_1}(k) c_{\tau_2\sigma_2}(k) \tag{2.24}$$

We see that intrinsic SOC contains the contribution from next-nearest neighbor hopping. On the second term, the sum of j and l The coefficient $\chi_{j,l}$ has value 1 or -1 when the hopping is anticlockwise or clockwise for sublattice A. Meanwhile, the coefficient has an opposite value for sublattice B. The strength of SOC parameter λ_I (in order μeV) depends on the coupling between p_z orbital and σ orbital (hybridization between s and p_x/p_y). It also depends on the hybridization between p_z orbital and d orbital. It is interesting to interpret Eq. 2.24 as the Zeeman coupling between the spin and a local perpendicular magnetic field with opposite direction for different sublattice.

When an external perpendicular electric field is applied on graphene layer, the Rashba spin orbit coupling is generated as a consequence of atomic polarization similar to the Stark effect in atomic system. This external electric field will contribute to the system energy through a term that is proportional to eEz. From the pertubation theory, we need to calculate this operator in the relevant orbital bases. As operator z has negative parity, the only coupling that survives is between p_z orbital and s orbital providing the finite term of $< p_z|z|s >$. The spin up electron from p_z orbital do on-site hopping to s orbital state due to the coupling by the external electric field. Then, this electron hop to the p_x or p_y state of the nearest carbon atom. Now, this spin-up electron can do on-site hopping to p_z orbital due to intrinsic spin orbit coupling on p orbital, flipping the spin up to become spin down. Overall this process leads to a hopping of spin-up p_z orbital electron to its nearest neighbor with opposite spin. This mechanism is proposed by Konschuh et al [5] calculating the Rashba SOC potential which takes the form:

$$V^{RB} = i\lambda_{RB} \sum_{<j,m>} \sum_{\sigma_1\tau_1} \sum_{\sigma_2\tau_2} c^{\dagger}_{\tau_1\sigma_1}(\boldsymbol{R_j}) \left(\boldsymbol{\sigma} \times \boldsymbol{n_m}\right)^{z}_{\sigma_1\sigma_2} c_{\tau_2\sigma_2}(\boldsymbol{R_m}) \tag{2.25}$$

$$V^{RB}(k) = i\lambda_{RB} \sum_{\sigma_1\tau_1} \sum_{\sigma_2\tau_2} c^{\dagger}_{\tau_1\sigma_1}(k) \left(\xi\tau_x\sigma_y - \tau_y\sigma_x\right)_{\substack{\tau_1\tau_2 \\ \sigma_1\sigma_2}} c_{\tau_2\sigma_2}(k) \tag{2.26}$$

$< j, m >$ denotes the nearest neighbor and $\boldsymbol{n_m}$ is the unit vector connecting the two atoms.

In order to have sizeable spin orbit interaction in graphene, TMD layer can be utilized to form a bilayer system [6, 45]. The inversion symmetry is broken when graphene is deposited on a monolayer TMD suggesting that spin degeneracy could be lifted on this sytem. The graphene layer will also experience an effective electric field on z direction as a result of mirror symmetry broken on z axis, hence, the Rashba type of SOC can be obtained. The magnitude of the induced Rashba SOC parameter λ_{BR} varies between 0.13

meV in MoS_2 substrate to 0.56 meV in $MoSe_2$ substrate [45]. The hybridization with d orbital of Mo atom could lead to the enhancement of the intrinsic SOC to the order of 0.2 meV [6] when MoS_2 is used as the substrate. The induced SOC can be increased further if a heavier transition metal atom is used such as WS_2 giving the value of intrinsic SOC to be about 1 meV [45]. Furthermore, band inversion is also observed in graphene on WSe_2 substrate [45].

2.2.3 Topological Phase in Graphene

Combination between spin orbit interaction and time-reversal symmetry can produce interesting electronic features on graphene such as topological insulator or quantum spin hall. In this state, graphene exhibits a gap in the bulk which is not continuously connected to the vacuum insulator without having transition to a gapless state. It can be illustrated by imagining a semiconductor material with the gap which is strained to increase the atom-atom distance. The gap will increase as the electrons become harder to move to other atom due to the energy barrier. The crystal properties will be diminished when the atom-atom distance is large enough to form a vacuum state. Hence, this semiconductor has a trivial gap as it is connected directly to vacuum by continuous deformation of the hamiltonian.

We can generate a gap in graphene by adding a staggered sublattice potential $H_s = V_s \sigma^z_{\alpha\beta} c^\dagger_{\alpha,\sigma}(\bar{k}) c_{\beta,\sigma}(\bar{k})$ to the hamiltonian. The $2V_s$ represents the potential difference between two sublattices. Note that the inversion symmetry is broken under this potential. The degeneracy of Dirac points at both valleys is lifted because sublattice A and B have energy V_s and $-V_s$ serving, respectively. The conduction band at K and K' consist of states with $(A, \uparrow)$ and $(A, \downarrow)$. The valence band at K and K' consist of states $(B, \uparrow)$ and $(B, \downarrow)$. The gap produced with this term can be regarded as trivial gap because we can connect it to

a vacuum gap as the two sublattices simply just decouple in the strong limit similar to what happens in the vacuum.

We also can open the gap by adding spin orbit coupling given in Eq. 2.24. Electron at valley K will effectively experience Zeeman interaction with perpendicular magnetic field on $+z$ direction for sublattice A and $-z$ direction for sublattice B. Electron at valley K' will also see this Zeeman field but the direction of the magnetic field will be opposite from the valley K. The conduction and valence band at K are constructed by $(c_{A,\uparrow}(K); c_{B,\downarrow}(K))$ and $(c_{A,\downarrow}(K); c_{B,\uparrow}(K))$, respectively. However, the conduction and valence band at K' have an opposite structure with K. Hence, the gap at K' is inverted relative to the gap at K. We call this non-trivial gap because it can not be connected to the vacuum gap. When small in-plane electric field E_y is applied, there will be no net charge current in the system. But the spin current $\boldsymbol{J_s} = (\hbar/2e)\,(\boldsymbol{J_\uparrow} - \boldsymbol{J_\downarrow})$ will have a finite value where it will flow transverse to the electric field. This spin current is proportional to the electric field by formula $\boldsymbol{J_s} = \sigma^s_{xy} E_y$ with σ^s_{xy} the spin current conductivity. It is shown that this conductivity is quantized with the value $\sigma^s_{xy} = \frac{e}{2\pi}$ [4].

If we confine the topological insulator to be a strip such as zigzag or armchair graphene nanoribbon where we take the one-dimensional periodicity on x direction, we will have gapless edge states on both edges of the strip. These edge states are a consequence of a topological transition from non-trivial to trivial state (vacuum). They are not chiral since we have the states propagating to opposite directions (right or left direction) at each edge [4]. If the moving right state has a spin up, the time reversal symmetry requires the moving left state to have an opposite spin. Hence, we see there is a chiral spin current on each edge where the opposite edge has opposite direction of the spin current. Notice also backscattering from spin-conserving weak disorder is forbidden at each edge because the reflected state has an opposite spin from the incoming state.

2.3 Graphene Nanoribbon

We can confine graphene to be one-dimensional system or strip which we will call graphene nanoribbon (GNR). This nanoribbon can have many different edge shapes. In this work, we will particularly consider two common edge shapes for instance, armchair and zigzag shape. Armchair-GNR (AGNR) and Zigzag-GNR (ZGNR) crystal structures can be obtained by confining graphene shown in Fig. 2.8(a) along y and x direction. In AGNR, each edge has both sublattices serving as the boundaries. This differs from ZGNR where we see that the left and right edge only have sublattice A and B, respectively. The length of the translation vector along the periodic axis is $a_{AGNR} = \sqrt{3}a_g$ for AGNR and $a_{ZGNR} = a_g$ for ZGNR. The dimensionless ribbon width (N) is characterized by the number of dimer lines for AGNR and zigzag chains for ZGNR.

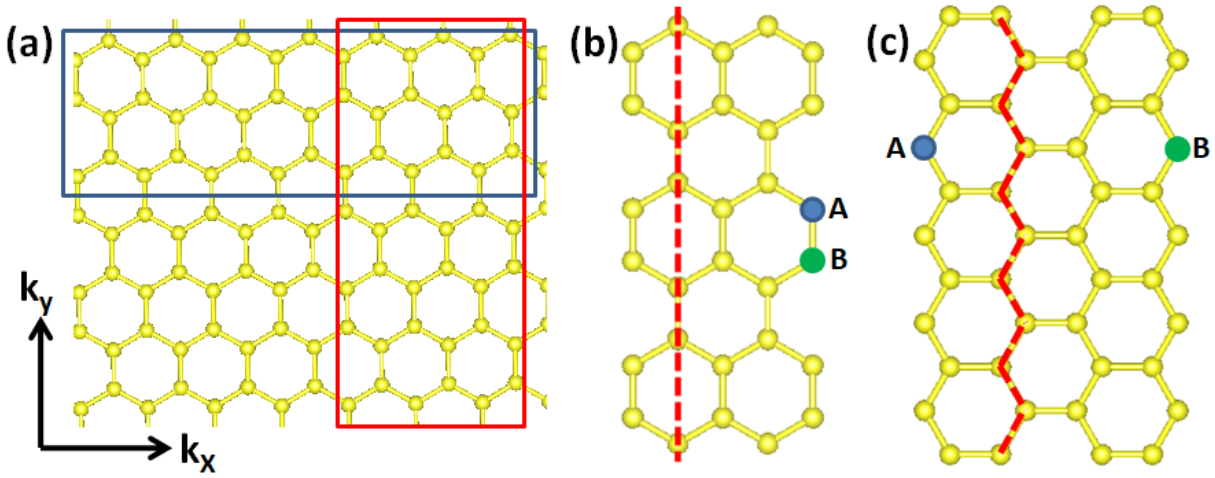

FIG. 2.8: The structure of GNR can be made by cutting graphene on particular direction shown in (a). The structure of AGNR and ZGNR is given in (b) and (c), respectively, with red(dash) and zigzag line defining the dimer line and zigzag chain.

The carbon atom has four valence electrons from s orbital and three p orbital. In graphene, s orbital hybridize with p_x and p_y orbital to form three σ orbitals. Hence, we see that carbon has covalent σ bonding with other three nearest carbon in graphene. This is also true in graphene nanoribbon except for the carbon at the edges. The edge atoms only can have bonding with two nearest carbon which leave one dangling bond unsaturated. The edge also can be passivated with other atoms such as hydrogen or with other molecules [46]. The edge characteristic will determine the low energy bands of GNR.

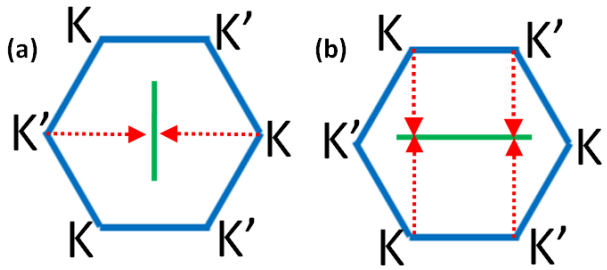

FIG. 2.9: Figure (a) shows the first BZ of graphene (hexagon) and AGNR (green line). Valley K and K' are projected to k = 0 of AGNR. Figure (b) shows the orientation of ZGNR's BZ. We see that valley K and K' are projected to $k = -2\pi/a_G$ and $k = 2\pi/a_G$, respectively.

The relative orientation of ZGNR reciprocal lattice vector respect to BZ of graphene is given in Fig. 2.9. The size of BZ of AGNR and ZGNR will be $2\pi/\mathrm{a_{AGNR}}$ and $2\pi/\mathrm{a_{ZGNR}}$, respectively. If we fold graphene bands along k_y axis, we see that valley K and K' of graphene can be translated to $k = 0$ of AGNR unit cell in the reciprocal space. On the other hand, if we fold the graphene bands along k_x axis, valley K and K' are projected to $k = \pm 2\pi/3a_G$ within the unit reciprocal space of ZGNR. Hence, it is expected the low energy bands will be located around $k = 0$ for AGNR and $k = \pm 2\pi/3a_G$ for ZGNR within their one-dimensional BZ.

2.3.1 Armchair Graphene Nanoribbon

The tight binding model of AGNR has been developed in previous works [47, 48, 49, 50]. The basic TB model where the hopping energy between p_z orbital taken to be constant throughout the ribbon will predict metallic behavior when the ribbon width $N = 3m + 2$ for m some positive integer. The ribbon will become a semiconductor when the widths are equal to $N = 3m$ and $N = 3m + 1$. These predictions are not similar to DFT calculation which suggests AGNR to be a semiconductor with a finite gap regardless of its width. This difference between DFT and TB could be explained by considering non-uniform hopping energy between carbon at the edge and the middle of ribbon. Besides, the third nearest neighbor hopping can contribute to the opening gap for metallic ribbon [48]. We will review some TB model that has been developed previously. At first, we will assume hopping energy to be uniform and constant. Even though this basic model has failed to reproduce DFT calculation, it still can provide us basic insight about AGNR electronic properties.

We discuss the approach developed by Huaixiu et all [50] to construct TB model of AGNR. The ribbon with size N is modeled to be N + 2 because there will be an additional dimer lines at each edge serving as the boundary. For the simplification, we give index for each dimer line range between $n = 0, ..., N + 1$. The wavefunctions for carbon atom at $n = 0$ and $n = N+1$ line will set to be zero indicating the confinement effect and boundary condition. On each dimer line, we have two carbon atoms featuring like sublattice A and B on graphene. Hence, the sublattice is specified by three indexes for instance $|X, A, n >$ represent the bases in the real space from carbon at position $\boldsymbol{R} = X\sqrt{3}a_g\hat{\boldsymbol{i}} + \boldsymbol{\tau_{A,n}}$. X is the integer to indicate the primitive cell of AGNR. They show that the wavefunction can

be chosen to be:

$$|\psi>= C_A\left[\sum_{i=1}^{N}\sum_X e^{ik\sqrt{3}.X.a_g}\sin\left(\tfrac{p\pi}{N+1}i\right)|X,A,n>\right]+C_B\left[\sum_{i=1}^{N}\sum_X e^{ik\sqrt{3}.X.a_g}\sin\left(\tfrac{p\pi}{N+1}i\right)|X,B,n>\right] \tag{2.27}$$

The sinusoidal function will guarantee the wavefunction to vanish when n = 0 and n = N + 1. Index p indicates the band index with the value $p = 1, 2, ..., N$. By restricting to nearest neighbor hopping with constant hopping energy t, the hamiltonian can be formulated by $H = -\sum_{<i,j>} t|i><j|$. The energy eigenvalue can be calculated by diagonalizing the hamiltonian for particular band index p given by:

$$\epsilon_{\pm} = \pm t\sqrt{1+4\cos^2\left(\frac{p\pi}{N+1}\right)+4\cos\left(\frac{p\pi}{N+1}\right)\cos\left(\frac{\sqrt{3}}{2}ka\right)} \tag{2.28}$$

So, we have conduction and valence band for each p. We see from Eq.2.28 that the gap is closed when $N = 3m + 2$ indicating the metallic state of ribbon. If we do expansion around $k = 0$, we obtain the dispersion of the low energy band similar with Dirac band of graphene $\epsilon = \pm v_g k$ with v_g is graphene Fermi velocity. The other value of $N = 3m$ and $N = 3m + 1$ will make AGNR to be a semiconductor with a gap $\triangle \approx \frac{2\pi}{\sqrt{3}(N+1)}t$.

It turns out that DFT calculation produces different low energy properties where AGNR will become a semiconductor for any size. The gap is still proportional to $\frac{1}{w}$ where w is the ribbon width. From the relation between energy gap and the ribbon width, it is found that AGNR can be categorized into three different families depending on the number of dimmer lines N. Son Et al. [51] shows the energy gap following $\triangle_{3m+1} > \triangle_{3m} > \triangle_{3m+2}$ which is different from TB prediction with constant and uniform nearest neighbor hopping energy. The finite size of ribbon plays the role of this behavior. As we confine the graphene to be a strip, the hopping energy will vary between carbon located at the middle and at the edge. The bond length at the edge is decreasing about 3% for $N = 12 - 14$ which

contribute to 12% increase of hopping energy [51].

2.3.2 Zigzag Graphene Nanoribbon

Localized States in ZGNR

ZGNR has interesting electronic features where it exhibits semiconducting and magnetic ordering which is not observed in graphene or AGNR. Its low energy bands are also formed by the wavefunctions that are localized at the edges of ribbon. In this section, we will review the TB model and DFT calculation that has been extensively studied.

We will start to discuss about the earliest TB model to describe the ZGNR bandstructure [47]. We will restrict the pz orbital on each carbon atom to hop only to its nearest neighbor with constant and uniform energy t. The bases of this hamiltonian will have three indexes to identify the sublattices within the primitive cell. These indexes are p with the integer value between $0, ..., L-1$ to represent the primitive unit cell, m with the integer value between $1, ..., N$ to identify the zigzag chain where carbon atom located, and A/B to denote the sublatice types. Hence, the electron creation operator is written as $c^{\dagger}_{m,A/B}(\boldsymbol{R_p})$ with $\boldsymbol{R_p} = p\boldsymbol{T_z} + \boldsymbol{\tau}_{m,A/B}$. The nearest neighbor hamiltonian is simply $H = t\sum_{<i,j>} c^{\dagger}_i c_j$ with i,j denote the sites of carbon and $< i, j >$ denotes the nearest neighbor hopping. According to the Bloch theorem, the hamiltonian of the periodic system can be diagonalized in the momentum space. Hence, we transform from the real space to the k space using:

$$c^{\dagger}_{m,A/B}(R_p) = \frac{1}{\sqrt{L}} \sum_k e^{-ik.R_p} c^{\dagger}_{m,A/B}(k) \tag{2.29}$$

We will select a particular width with N = 4 in order to explicitly show the structure of the hamiltonian. If we represent the k-space hamiltonian in matrix representation with the bases $\left(c^{\dagger}_{1,A}(k), c^{\dagger}_{1,B}(k), c^{\dagger}_{2,A}(k), c^{\dagger}_{2,B}(k), c^{\dagger}_{3,A}(k), c^{\dagger}_{3,B}(k), c^{\dagger}_{4,A}(k), c^{\dagger}_{4,B}(k)\right)$, we obtain:

$$H(N=4)=\left[\begin{array}{cc|cc|cc|cc} 0 & 2t\cos\left(\frac{k.a}{2}\right) & 0 & 0 & 0 & 0 & 0 & 0 \\ 2t\cos\left(\frac{k.a}{2}\right) & 0 & t & 0 & 0 & 0 & 0 & 0 \\ \hline 0 & t & 0 & 2t\cos\left(\frac{k.a}{2}\right) & 0 & 0 & 0 & 0 \\ 0 & 0 & 2t\cos\left(\frac{k.a}{2}\right) & 0 & t & 0 & 0 & 0 \\ \hline 0 & 0 & 0 & t & 0 & 2t\cos\left(\frac{k.a}{2}\right) & 0 & 0 \\ 0 & 0 & 0 & 0 & 2t\cos\left(\frac{k.a}{2}\right) & 0 & t & 0 \\ \hline 0 & 0 & 0 & 0 & 0 & t & 0 & 2t\cos\left(\frac{k.a}{2}\right) \\ 0 & 0 & 0 & 0 & 0 & 0 & 2t\cos\left(\frac{k.a}{2}\right) & 0 \end{array}\right] \tag{2.30}$$

The bandstructure within the BZ is shown in Fig. 2.10(a). From this plot, we see that ZGNR is a metal with the energy band at Fermi level located around $k_F = \pm\pi/a_g$. The bands are spin degenerate since the hamiltonian is spin independent. The flat Fermi surface indicates the DOS is higher at the Fermi level.

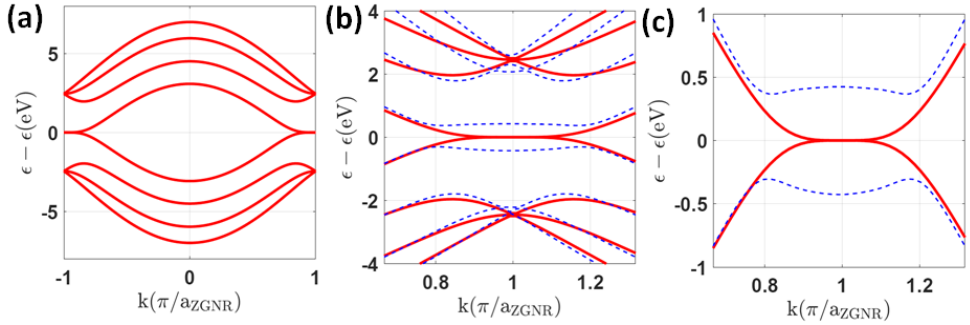

FIG. 2.10: The bandstructure of ZGNR (N = 4) calculated using TB with constant nearest neighbor hopping energy given by red lines. (a) shows the bands within the first BZ of ZGNR. (b) and (c) are the low energy bands. Dash blue lines are the bands from DFT calculation.

If we set k to be $\pm\pi/a_g$, the cos term will vanish causing $c^\dagger_{1,A}(\pm\pi/a_g)$ and $c^\dagger_{4,B}(\pm\pi/a_g)$ decouple from other bases. We obtain two localized states at each edge with zero energy. The wavefunction at this k point will be a linear combination of these localized states. The projected wavefunction on the sublattices for the highest valence and lowest conduction bands are given in Figure 2.11 (a) and (b), respectively. We observe that the wavefunctions

corresponding to the flat band or around $k = \pm\pi/a_g$ are almost localized at the two edges.

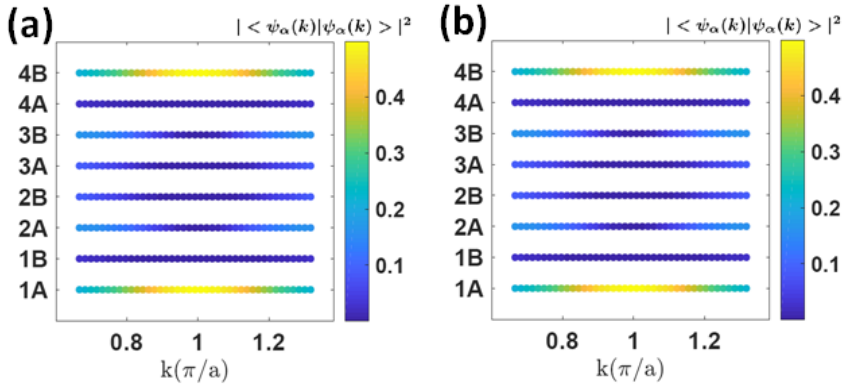

FIG. 2.11: The orbital projection to carbon atoms for the wavefunctions at the flat bands are shown in (a) and (b).

The emergence of the localized wavefunctions (edge state) is not only limited for narrow ribbon. We can generalize this result for wider ribbon by using the solution of Dirac hamiltonian with appropriate boundary conditions [49]. In this approach, ribbon is modeled as graphene confined along y axis with the size L. The wavefunction at valley K and K' can be used as the bases of the low energy band hamiltonian. The corresponding wavefunctions from the two valleys can be written as:

$$\psi_{K/K'}(x,y) = \begin{bmatrix} \phi_A(K/K',y) & \phi_B(K/K',y) \end{bmatrix}^T e^{ik_x x} \tag{2.31}$$

k_x is the momentum parallel to the translation axis of ribbon which is chosen to be in x direction. It should be noted that the momentum k_x is taken relative to the valley K or K'. Hence, the momentum according to ribbon will be $4\pi/3a_g + k_x$ for state associated with K and $-4\pi/3a_g + k_x$ for state associated with K'. Each of wavefunction is an eigenfunction of Dirac equation where we replace k_y with $-i\partial_y$. The hamiltonian for the electron at

valley K can be written as:

$$H_K = v_g \begin{bmatrix} 0 & -k_x + \partial_y \\ -k_x - \partial_y & 0 \end{bmatrix} \tag{2.32}$$

The hamiltonian for the electron at valley K' is given by:

$$H_{K'} = v_g \begin{bmatrix} 0 & k_x + \partial_y \\ k_x - \partial_y & 0 \end{bmatrix} \tag{2.33}$$

In the following, we will only focus on the wavefunction at valley K because similar mathematical steps can also be applied to valley K'. If ψ_K is the eigenfunction of the Hamiltonian in Eq. 2.32 with energy ϵ, we will obtain that $\phi_A(K, y)$ has to satisfy following differential equation:

$$\partial_y^2 \phi_A(K, y) = z^2 \phi_A(K, y) \tag{2.34}$$

We define $z = \sqrt{k_x^2 - \tilde{\epsilon}^2}$ with $\tilde{\epsilon} = \epsilon / v_g$. The wavefunction for sublattice B can be determined by:

$$\phi_B(K, y) = -\frac{1}{\tilde{\epsilon}} \left(k_x + \partial_y\right) \phi_A(K, y) \tag{2.35}$$

To incorporate the confinement into the model, we exert the boundary conditions on sublattice A and B to be zero at $x = 0$ and $x = L$, respectively. Mathematically, this can be written as:

$$\phi_A(K, 0) = \phi_B(K, L) = 0 \tag{2.36}$$

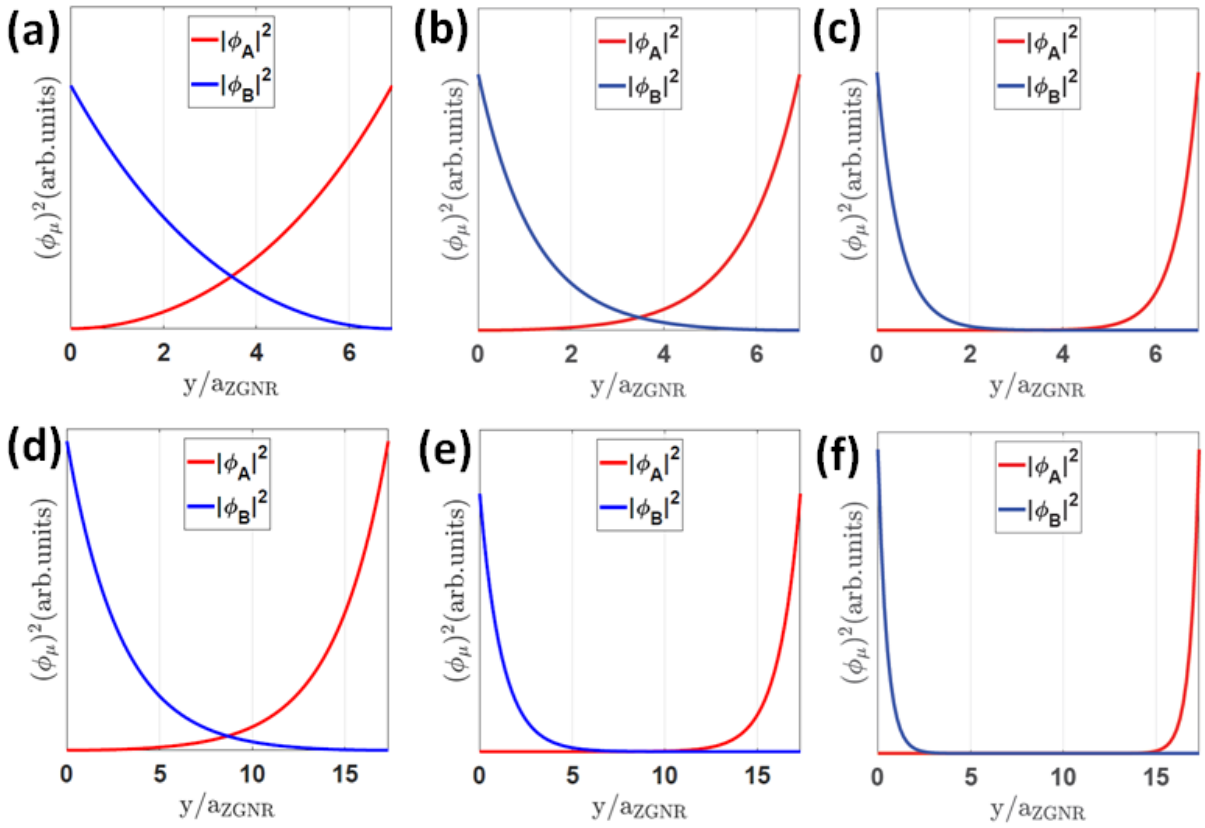

FIG. 2.12: The magnitude of the wavefunctions for sublattice A $\left(|\phi_A(K,y)|^2\right)$ and sublattice B $\left(|\phi_B(K,y)|^2\right)$ are shown as function of y. Top and bottom panels correspond to ribbon width $N = 4$ and $N = 10$. We chose different value of momentum k_x. It will be more convenient if we take the momentum relative to the edge of ZGNR brillouin zone at $k = -\pi/a_g$. Hence, the momentum of wavefunction are 0.35Å^{-1} for (a,d), 0.25Å^{-1} for (b,e), and 0Å^{-1} for (c,f).

Therefore, we see that z in Eq. 2.34 has to satisfy a transcendental equation:

$$e^{2zL} = \frac{k_x - z}{k_x + z} \tag{2.37}$$

We also obtain the wavefunction for sublattice A and B as:

$$\phi_A(K,y) = C\left(e^{zy} - e^{-zy}\right) \tag{2.38}$$

$$\phi_B(K,y) = -C\frac{k_x + z}{\tilde{\epsilon}}\left(e^{zy} - e^{-zy}e^{2zL}\right) \tag{2.39}$$

If z has pure real value, the wavefunction is exponentially decreasing from the edge to the center of ribbon which corresponds to the localized state. If z has pure imaginary value, we will have harmonic oscillation of the wavefunction in y direction. This means that there is a resonance state along y axis. By using these equations and solving transcendental equation in Eq. 2.37, we can plot the wavefunction that contribute to the flat energy bands shown in Fig. 2.12.

Magnetic Ground state of ZGNR

We have seen that the wavefunctions corresponding to the flat bands are localized at the edges of ribbon. The flat bands indicate high density of states (DOS) at Fermi level. Hence, there will be strong electron-electron interaction acted on this localized states which is not included in the previous TB model. If we incorporate the electron-electron interaction via exchange interaction to the hamiltonian, we observe that ZGNR will have magnetic ground state depending on its width. The two magnetic ground states are Ferro-AntiFerroMagnetic (FA) and Ferro-FerroMagnetic (FF) states. They have spin ordering along their edges. In FA ground state, each edge has ferromagnetic spin ordering with the opposite spin orientation between the edges. On the other hand, FF ground state has the same spin orientation between both edges.

DFT calculation shows that the FA ground state is more preferable for narrow ribbon as the energy is lower than FF state. When the ribbon width is increasing the energy difference between these two states becomes smaller. But it should be noted that the non-

magnetic state still has higher energy than in FA or FF state. Hence, the ribbon could have two degenerate magnetic ground states for larger width.

We present the bandstructure of ZGNR (N = 4) in FA and FF ground state which are calculated using DFT in Figure 2.13(a-b), respectively. The spin degeneracy is still retained in the FA state. However, we see that ZGNR become a semiconductor with a finite gap scaled by its width. Its wavefunction around $k = \pm\pi/a_g$ is mostly localized at the edges with different spin for the opposite edges. On the contrary, FF ground state exhibits metallic behavior which is spin polarized. The low energy bands look similar with the non-magnetic case produced within TB model. With the difference, one of the spin bands are lowered in energy, while the opposite spin bands have higher energy.

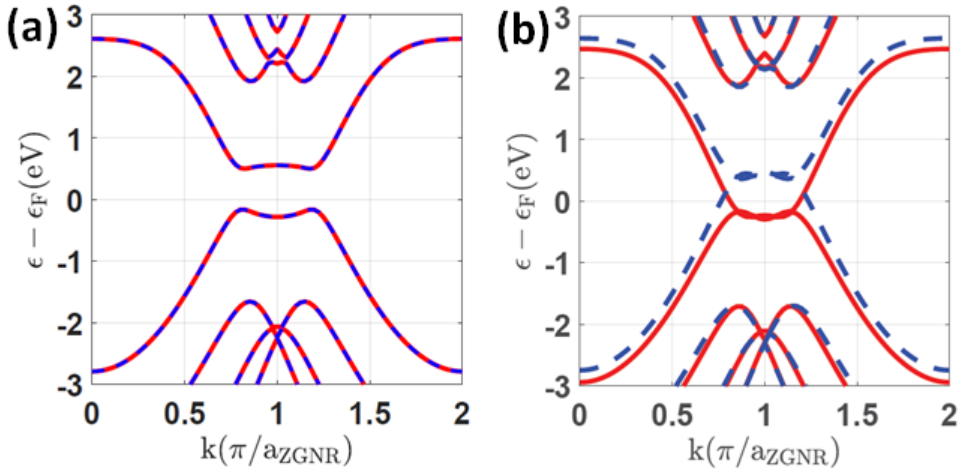

FIG. 2.13: (a) and (b) are the bandstructure of ZGNR (N = 4) in FA and FF ground states calculated using DFT, respectively.

This magnetic behavior can be explained by introducing Hubbard interaction in TB model that we have in previous section. The Hubbard interaction can be expressed as:

$$V_H = \sum_i U n_{i,\uparrow} n_{i,\downarrow} \tag{2.40}$$

This electron-electron interaction depends on the electron density on each lattice site i. In general, there is no analytical solution for this interaction. We will try to use very rough simplification to simplify the model. We also use mean field theory by replacing the interaction by $U < n_{i,\uparrow} > n_{i,\downarrow} + U < n_{i,\downarrow} > n_{i,\uparrow}$. We address that this interaction will significantly modify the energy for the atoms at both edges. Therefore, we can neglect this term for the carbon atoms positioned not at the edges. We set the average electron number in the ground state to be 1 for $< n_{L,\uparrow} >$ and $< n_{R,\downarrow} >$. On other hand, the average number of the electron for $< n_{L,\downarrow} >$ and $< n_{R,\uparrow} >$ are zero. These conditions are chosen by considering the result from the DFT calculation. Using this assumptions, the electron-electron interaction manifest as a staggered sublattice potential difference between left and right edges with the spin dependent term. This is equivalent as in hexagonal boron nitride (hBN) where boron and nitrogen has different on-site potential due to ionic bonding between them. In both cases, this staggered potential is responsible to the energy band gap between valence and conduction bands. Figure 2.14 is the bandstructure within TB

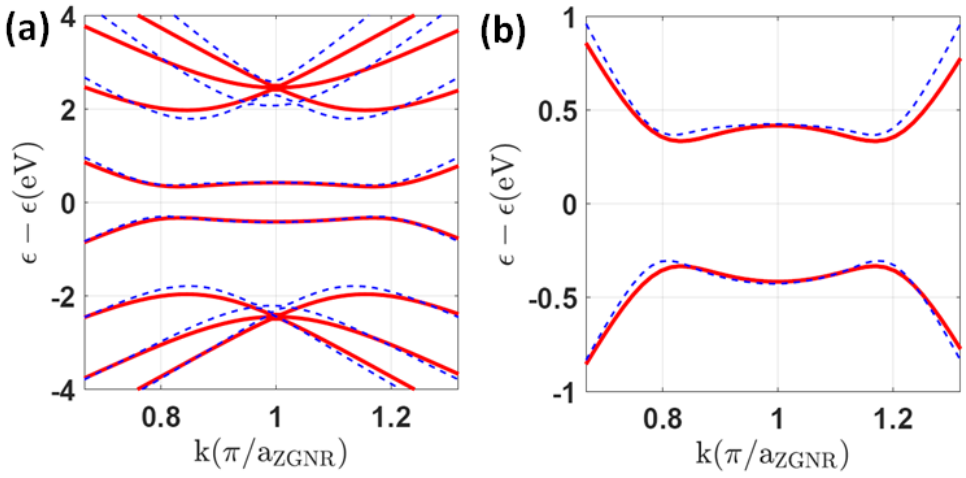

FIG. 2.14: (a-b) show the bandstructure of ZGNR (N = 4) calculated using TB with the simplified of Hubbard interaction shown by red lines. We also plot the bands calculated using DFT given by dash blue lines as comparison.

model by incorporating the Hubbard term with $U = 0.833eV$ given by the red lines. As a comparison, DFT result is given by dashed-blue lines. We see a good agreement between these two models justifying the assumptions that we have.

CHAPTER 3

Graphene-NbSe2

Transition metal dichalcogenides (TMDs) are extremely interesting materials due to their unique electronic properties [52, 53, 54, 55, 56, 45, 57, 58, 38, 59, 60] and the fact that in recent years experimentalists have been able to isolate and probe TMD films only few atoms thick, down to the monolayer limit. Some TMDs monolayers, like $MoSe_2$ and MoS_2, are insulators with gaps of the order of 1.5-2 eV. Other TMDs monolayers, such as $NbSe_2$, NbS_2, $TaSe_2$, TaS_2 are metallic at room temperature and superconducting at low temperature. One feature that all TMDs have in common is a strong spin-orbit coupling (SOC). In monolayer TMDs the strongest effect of the SOC is a spin-splitting of the conduction and valence bands around the K, and K', points of the Brillouin zone (BZ) [61, 62, 20]. For the TMDs that are superconducting at low temperature, such a spin splitting causes the superconducting pairing to be of the Ising type [38] and therefore extremely robust to external in-plane magnetic fields [36, 63, 64, 65]. The ability of metallic TMDs to exhibit superconductivity even in the limit in which they are only one-atom thick, and the robustness of such a superconducting state to external magnetic fields makes them very interesting systems both from a fundamental point of view and for

possible applications.

Recent advances in fabrication techniques have made possible the realization of van der Waals (vdW) heterostructures obtained by stacking crystals that are only a few atoms thick [66, 67] In these structures, the different layers are held together by van der Waals forces. As a consequence the crystals that can be used to create the structures, and their stacking configuration, are not limited to the configurations allowed by chemical bonds. This makes possible the realization of systems with unique properties such as graphene–topological-insulator heterostructures in which graphene has a tunable spin-orbit coupling depending on the stacking configuration [68, 69, 70, 71, 72].

In graphene the conduction and valence bands touch at the corners (K and K' points) of the hexagonal BZ, and around these points the electrons behave as massless Dirac Fermions [73, 39]. This fact makes graphene an ideal semimetal in which the polarity of the carriers can easily be tuned via external gates. In addition, graphene has a very high electron mobility due to its very low concentration of defects and the fact that electron-phonon scattering processes do not contribute significantly to the resistivity for temperatures as high as room temperature [74, 1, 75]. All these features make graphene an ideal system to probe, via tunneling setups, other materials and to realize novel vdW heterostructures with tunable properties. In particular, the fact, that the low energy states of graphene, in momentum space, are located just at the K points of its BZ, in vdW structures implies that by simply varying the twist angle, graphene can be used as a momentum selective probe of the electronic structure, and properties, of the substrate. The work that we present below is an example of such momentum-selective probing capability of graphene. In monolayer $NbSe_2$ the Fermi surface (FS) is formed by a pocket around the Γ point, and pockets around the K, and K' points. Contrary to bulk $NbSe_2$, in monolayer $NbSe_2$ there is no selenium-like FS pocket around the Γ point. As a consequence monolayer $NbSe_2$ is expected to be a single-gap superconductor with the same gap at the Γ pocket as at the

K pockets [76]. However, the Γ and K pockets differ in the magnitude, and k dependence around the pocket, of the spin-splitting induced by the spin-orbit coupling. The splitting is much larger for the K pockets and therefore the superconducting gap for these pockets is much more robust to external in-plane magnetic fields than for the Γ pocket. As we show below a graphene-$NbSe_2$ heterostructure allows to probe separately $NbSe_2$'s states around the Γ point, and **K** point simply by tuning the relative twist angle between graphene and $NbSe_2$ and therefore to study the difference between pockets of the interplay between spin-orbit coupling and superconducting pairing.

In this work we study vdW heterostructures formed by graphene and monolayer $NbSe_2$. Our results show that despite the large mismatch between the lattice constants of graphene and $NbSe_2$ in these structures a large superconducting pairing can be induced into the graphene layer. In addition, we show how such pairing depends, both in nature and structure, on the stacking configuration. Our results are relevant also to other graphene-TMD heterostructures such as the ones that can be obtained by replacing the $NbSe_2$ monolayer by a monolayer of NbS_2, $TaSe_2$, or TaS_2 that have also been shown to be superconducting at low temperature [77, 78, 65, 79] and show how graphene can be used to probe in these systems the momentum-dependent superconducting gap and in particular its multiband structure.

3.1 Method

In graphene the carbon atoms are arranged in a 2D hexagonal structure formed by two triangular sublattices, A and B, with lattice constant $a_g = \sqrt{3}a = 2.46\mathring{A}$, with $a = 1.42\mathring{A}$ the carbon-carbon atomic distance. The 2D structure of $NbSe_2$ is also formed by two triangular sublattices. One of the sublattices is formed by the Nb atoms, the other by two Se atoms symmetrically displaced by a distance $u = 1.679$Å above and below the plane

formed by the Nb atoms. The lattice constant of $NbSe_2$ is $a_s = 3.48$Å. [62]. Figure 3.1 shows the Brillouin zone of graphene and $NbSe_2$. In this figure and in the remainder we take k_x to be in the direction connecting the valley $\mathbf{K}$ with its time-reversed partner $\mathbf{K}'$. Figure 3.1 (a) shows the relative orientation of the graphene's and $NbSe_2$'s BZs for the case when the twist angle θ is zero and Figure 3.1 (b) for a case when $\theta \neq 0$.

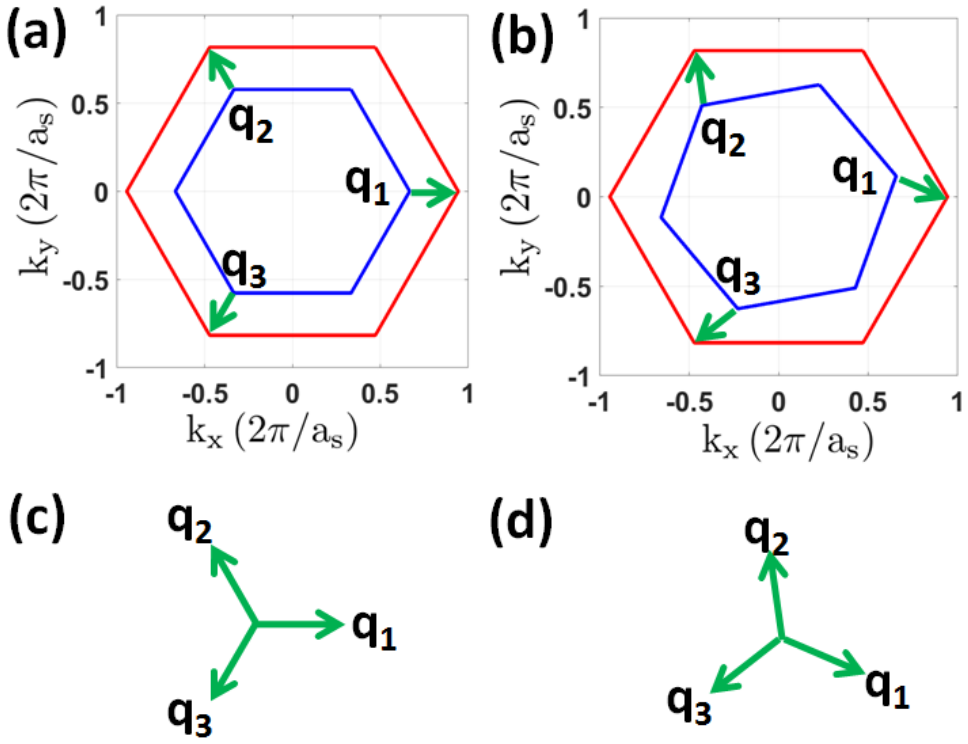

FIG. 3.1: Brillouin zone for graphene and $NbSe_2$, and corresponding q-vectors for the case when $\theta = 0$, (a), (c), and $\theta \neq 0$, (b), (d).

To obtain the electronic structure of the graphene-$NbSe_2$ structure for a generic twist angle and in the presence of superconducting pairing in the $NbSe_2$, we first need to estimate the charge transfer between the graphene layer and $NbSe_2$, and the strength of the tunneling t between graphene and the $NbSe_2$ monolayer. To this effect we first obtain via ab-initio the electronic structure of a commensurate graphene-$NbSe_2$ structure. Let $\mathbf{a}_{1s} = a_s[\cos(\pi/3)\mathbf{x} - \sin(\pi/3)\mathbf{y}]$, $\mathbf{a}_{2s} = a_s[\cos(\pi/3)\mathbf{x} + \sin(\pi/3)\mathbf{y}]$, be the primitive lattice

vectors for $NbSe_2$, and $\mathbf{a}_{1g} = a_g[\cos(\pi/3)\mathbf{x} - \sin(\pi/3)\mathbf{y}]$, $\mathbf{a}_{2g} = a_g[\cos(\pi/3)\mathbf{x} + \sin(\pi/3)\mathbf{y}]$, the primitive vectors for graphene, with $\mathbf{x}$ and $\mathbf{y}$ the unit vectors in the x and y direction, respectively. In a commensurate stacking configuration the primitive vectors satisfy the equation:

$$m_1\mathbf{a}_{1s} + m_2\mathbf{a}_{2s} = n_1\mathbf{a}_{1g} + n_2\mathbf{a}_{2g} \tag{3.1}$$

where (m_1, m_2, n_1, n_2) are four integers constrained by the following second order Diophantine equation:

$$(m_1^2 + m_2^2 - m_1m_2) = \frac{a_g^2}{a_s^2}(n_1^2 + n_2^2 - n_1n_2). \tag{3.2}$$

Given that the lattice constant of graphene and $NbSe_2$ are highly incommensurate with respect to each other, Eq. (3.1) (or, equivalently, Eq. (3.2)) can only be satisfied for a finite size system if we allow some amount of strain for one of the lattices. For this reason we allow a small amount of strain for the graphene lattice considering that the amount of charge transfer between the graphene layer and $NbSe_2$, and the magnitude of the graphene-$NbSe_2$ tunneling strength, are not expected to be affected by a small change of the graphene's lattice constant.

The ab-initio calculation were performed using the Quantum-Espresso package [80, 81]. We use full-relativistic ultrasoft pseudopotentials with the wavefunction kinetic energy cutoff of 50 Ry. We adopted the Perdew-Burke-Ernzerhof (PBE) [24] as the exchange and correlation functional. We set the vacuum thickness equal to 25Å to isolate the heterostructure and avoid the interactions between the periodic layers along the direction, (z), perpendicular to the layers. The interlayer distance between graphene and $NbSe_2$ was obtained by full relaxation in the z-direction. The total energy was calculated by using a $18 \times 18 \times 1$ Monkhorst-Pack scheme grid for the k points.

After having obtained the amount of charge transfer and the strength of the tunneling between the graphene layer and $NbSe_2$ via ab-initio, we use a continuum model [82, 83, 70]

to obtain the low-energy spectrum of the graphene-$NbSe_2$ heterostructure for different values of the twist angle θ. In general, the Hamiltonian $\hat{H}$ describing the graphene-$NbSe_2$ heterostructure can be written as: $\hat{H} = \hat{H}_g + \hat{H}_s + \hat{H}_t$ where $\hat{H}_g$ is the Hamiltonian for graphene, $\hat{H}_s$ is the Hamiltonian for $NbSe_2$ and $\hat{H}_t$ is the term describing tunneling processes between graphene and $NbSe_2$.

In graphene the low energy states are located at the $\mathbf{K}_g$ and $\mathbf{K}'_g$ points of the BZ: $\mathbf{K}_g = (4\pi/(3a_g), 0)$, $\mathbf{K}'_g = (-4\pi/(3a_g), 0)$ (and equivalent points connected by reciprocal lattice wave vectors). Close the $\mathbf{K}_g$ and $\mathbf{K}'_g$ points in graphene the electrons, at low energies, are well described as massless Dirac fermions with Hamiltonians $\hat{H}_{\mathbf{K}_g} = \sum_{\mathbf{k},\tau\tau'\sigma\sigma'} c^\dagger_{\mathbf{K}_g+\mathbf{k},\tau'\sigma'} H_{\mathbf{K}_g} c_{\mathbf{K}_g+\mathbf{k},\tau\sigma}$, $\hat{H}_{\mathbf{K}'_g} = \sum_{\mathbf{k},\tau\tau'\sigma\sigma'} c^\dagger_{\mathbf{K}'_g+\mathbf{k},\tau'\sigma'} H_{\mathbf{K}'_g} c_{\mathbf{K}'_g+\mathbf{k},\tau\sigma}$, where

$$H_{\mathbf{K}_g} = \hbar v_F \mathbf{k}\cdot\boldsymbol{\tau}\sigma_0 - \mu_g\tau_0\sigma_0, \tag{3.3}$$

$$H_{\mathbf{K}'_g} = -\hbar v_F \mathbf{k}\cdot\boldsymbol{\tau}^*\sigma_0 - \mu_g\tau_0\sigma_0, \tag{3.4}$$

$c^\dagger_{\mathbf{p},\tau\sigma}$ ($c_{\mathbf{p},\tau\sigma}$) is the creation (annihilation) operator for an electron, in the graphene sheet, with spin σ and two-dimensional momentum $\hbar\mathbf{p} = \hbar(p_x, p_y)$, $\mathbf{k}$ is a wave vector measured from $\mathbf{K}$ ($\mathbf{K}'$), $v_F = 10^6$ m/s is graphene's Fermi velocity, μ_g graphene's chemical potential, and τ_i, σ_i ($i = 0, 1, 2, 3$)) are the 2×2 Pauli matrices in sublattice and spin space, respectively. As a consequence, when considering the states of graphene close to the $\mathbf{K}_g$ ($\mathbf{K}'_g$) point we have $H_g = H_{\mathbf{K}_g}$ ($H_g = H_{\mathbf{K}'_g}$).

In $NbSe_2$ the low energy states are located close to the Γ, $\mathbf{K}$, and $\mathbf{K}'$ points of the BZ: $\mathbf{K}_s = (4\pi/(3a_s), 0)$, $\mathbf{K}'_s = (-4\pi/(3a_s), 0)$ (and equivalent points connected by reciprocal lattice wave vectors). Close the Γ point the effective low-energy Hamiltonian for $NbSe_2$ takes the form $H_{\Gamma_s} = \sum_{\mathbf{k}\sigma\sigma'} d^\dagger_{\mathbf{k},\sigma} H_{\Gamma_s} d_{\mathbf{k},\sigma'}$, where $d^\dagger_{\mathbf{k},\sigma}$ ($d_{\mathbf{k},\sigma}$) is the creation (annihilation) operator for an electron in $NbSe_2$ with momentum $\mathbf{k}$ and spin σ, and H_{Γ_s} is the effective

low energy Hamiltonian matrix for the conduction band of $NbSe_2$. By fitting the ab-initio results we obtain:

$$H_{\Gamma_s} = \epsilon_{0\Gamma}(\mathbf{k})\sigma_0 + \lambda_\Gamma(\mathbf{k})\sigma_z \tag{3.5}$$

where

$$\begin{aligned}\epsilon_{0\Gamma}(\mathbf{k}) &= \eta_{0\Gamma} + \eta_{2\Gamma}k_+k_- \\ \lambda_\Gamma(\mathbf{k}) &= l_{3\Gamma}\left[\left(k_+^3 + k_-^3\right)\cos(3\theta) + i\left(k_+^3 - k_-^3\right)\sin(3\theta)\right],\end{aligned} \tag{3.6}$$

$k_\pm = k_x \pm ik_y$, and $\eta_{0\Gamma}$, $\eta_{2\Gamma}$, $l_{3\Gamma}$ are constants:

$$\begin{aligned}\eta_{0\Gamma} &= \quad 0.5641\,\text{eV}, \\ \eta_{2\Gamma} &= -7.0640\,\text{eV}\,[a_s/(2\pi)]^2, \\ l_{3\Gamma} &= \quad 0.5085\,\text{eV}\,[a_s/(2\pi)]^3.\end{aligned} \tag{3.7}$$

Close to the corners of the BZ of $NbSe_2$, the $\mathbf{K}_s$ and $\mathbf{K}'_s$ points, for $NbSe_2$ we have $H_{\mathbf{K}_s} = \sum_{\mathbf{k}\sigma\sigma'} d^\dagger_{\mathbf{k},\sigma} H_{\mathbf{K}_s} d_{\mathbf{k},\sigma'}$, $H_{\mathbf{K}'_s} = \sum_{\mathbf{k}\sigma\sigma'} d^\dagger_{\mathbf{k},\sigma} H_{\mathbf{K}'_s} d_{\mathbf{k},\sigma'}$, where $\mathbf{k}$ is now a wave vector measured from the $\mathbf{K}_s$, $\mathbf{K}'_s$ point, respectively, and

$$H_{\mathbf{K}_s} = \epsilon_0(\mathbf{k})\sigma_0 + \epsilon_3(\mathbf{k})\sigma_0 + \lambda(\mathbf{k})\sigma_z \tag{3.8}$$

$$H_{\mathbf{K}'_s} = \epsilon_0(\mathbf{k})\sigma_0 - \epsilon_3(\mathbf{k})\sigma_0 - \lambda(\mathbf{k})\sigma_z \tag{3.9}$$

$$\tag{3.10}$$

where,

$$\begin{aligned}
\epsilon_0(\mathbf{k}) &= \eta_0 + \eta_2 k_+ k_-, \\
\epsilon_3(\mathbf{k}) &= \eta_3 \left[\left(k_+^3 + k_-^3\right) \cos(3\theta) + i \left(k_+^3 - k_-^3\right) \sin(3\theta) \right], \\
\lambda(\mathbf{k}) &= l_0 + l_2 k_+ k_-,
\end{aligned} \tag{3.11}$$

and η_0, η_2, η_3, l_0, l_2, are constants that we extracted from the ab-initio results for an isolated monolayer of $NbSe_2$:

$$\begin{aligned}
\eta_0 &= \quad 0.4526\,\text{eV}, \\
\eta_2 &= -9.0940\,\text{eV}\,[a_s/(2\pi)]^2, \\
\eta_3 &= \quad 3.07 \quad \text{eV}\,[a_s/(2\pi)]^3, \\
l_0 &= \quad 0.0707\,\text{eV}, \\
l_2 &= -0.33 \quad \text{eV}\,[a_s/(2\pi)]^2.
\end{aligned} \tag{3.12}$$

Let $\mathbf{p}_g$, $\mathbf{p}_s$, be the wave vector of an electron in graphene, $NbSe_2$, respectively. In the remainder we consider only momentum and spin conserving tunneling processes. Conservation of crystal momentum requires

$$\mathbf{p}_s + \mathbf{G}_s = \mathbf{p}_g + \mathbf{G}_g, \tag{3.13}$$

where $\mathbf{G}_g$ and $\mathbf{G}_s$ are reciprocal lattice vectors for graphene and $NbSe_2$ respectively. For the purpose of developing a continuum low energy model for a graphene-$NbSe_2$ heterostructure it is more convenient to consider the twist angle θ as relative twist between BZ's, as shown in Fig. 3.1. For $\theta = 0$ the $\mathbf{K}$ point of graphene's and $NbSe_2$'s BZs are on the same axis. Depending on the value of θ we can have two situations: the low energy states of graphene,

in momentum space, are close to $NbSe_2$'s Fermi pockets around the $\mathbf{K}$ and $\mathbf{K}'$ points, or, considering $NbSe_2$'s extended BZ, to $NbSe_2$'s Fermi pocket around the Γ point. In the first case the conservation of the crystal momentum, Eq. (3.13), takes the form:

$$\mathbf{k}_s = \mathbf{k}_g + (\mathbf{K}_g - \mathbf{K}_s) + (\mathbf{G}_g - \mathbf{G}_s) \tag{3.14}$$

where $\mathbf{k}_s$ $\mathbf{k}_g$ are momentum wave vectors measured from $\mathbf{K}_g$ and $\mathbf{K}_s$, respectively. By replacing $\mathbf{K}_g$, $\mathbf{K}_s$, with $\mathbf{K}'_g$, and $\mathbf{K}'_s$ in Eq. (3.14) we obtain the momentum conservation equation valid for momenta taken around the $\mathbf{K}'$ points. In the second case Eq. (3.13) takes the form:

$$\mathbf{k}_s = \mathbf{k}_g + \mathbf{K}_g + (\mathbf{G}_g - \mathbf{G}_s) \tag{3.15}$$

and similarly for momenta around $\mathbf{K}'_g$.

The conservation of the crystal momentum implies that the tunneling term takes the form:

$$\hat{H}_t = \sum_{\mathbf{G}_g \mathbf{G}_s \tau\sigma} \hat{T}_{\tau\sigma\sigma'}(\mathbf{p}_g + \mathbf{G}_g) e^{-i\mathbf{G}_g \cdot \mathbf{d}_\tau} c^\dagger_{\mathbf{p}_g \tau\sigma} d_{\mathbf{p}_g + (\mathbf{G}_g - \mathbf{G}_s)\sigma'} + h.c. \tag{3.16}$$

where $\mathbf{d}_\tau$ is the position of the carbon atom on sublattice τ within the primitive cell of the graphene sheet. For sublattice A $\mathbf{d}_\tau = (0, 0)$, for sublattice B $\mathbf{d}_\tau = (a_0, 0)$, with a_0 the carbon-carbon distance.

Considering that, as shown in table 3.1, the separation $d = 3.57\mathring{A}$ between the graphene sheet and $NbSe_2$ is much larger than the interatomic distance in each material, in momentum space, the tunneling amplitude $t(\mathbf{p})$ decays very rapidly as a function of $\mathbf{p}$ [83] and so in Eq.(3.16) we can just keep the terms for which $(\mathbf{p}_g + \mathbf{G}_g)$ is smallest, i.e., restrict the sum to $\mathbf{G}_g = 0$ and the two $\mathbf{G}_g$ that map $\mathbf{K}$ ($\mathbf{K}'$) to the two other equivalent points in the BZ and set $t = t(\mathbf{K})$. The sum over $\mathbf{G}_s$ is restricted by the fact that we only need to keep terms for which the graphene's and $NbSe_2$'s states have energy separated by

an amount of the order of t.

Let $\mathbf{q} = \mathbf{k}_s - \mathbf{k}_g$. The above considerations imply that for the case when the $\mathbf{K}_g$ and $\mathbf{K}_s$ are close we only need to keep the terms for which $|\mathbf{q}| = |\mathbf{K}_g - \mathbf{K}_s|$, given that these are the terms for which $(\mathbf{p}_g + \mathbf{G}_g)$ that satisfies Eq. (3.14) is smallest. Due to the C_{3v} symmetry of the hexagonal structure there are three equivalent $\mathbf{K}$ points, $\mathbf{K}_1$, $\mathbf{K}_2$, $\mathbf{K}_3$, (and $\mathbf{K}'$ points), i.e. two reciprocal lattice wave vectors $\mathbf{G}$ connecting equivalent corners of the BZ. There are three vectors $\mathbf{q}_{iK} = (\mathbf{K}_g - \mathbf{K}_s) + (\mathbf{G}_{gi} - \mathbf{G}_{si})$ $(i = 1, 2, 3)$ such that $|\mathbf{q}_i| = |\mathbf{K}_g - \mathbf{K}_s|$. $\mathbf{q}_{1K}$ is obtained by taking $\mathbf{G}_{g1} = 0$ and $\mathbf{G}_s = \mathbf{G}_{sK1} \equiv 0$, $\mathbf{q}_{2K}$ by taking $\mathbf{G}_g = \mathbf{G}_{g2} \equiv 4\pi/(\sqrt{3}a_g)[\cos(5\pi/6), \sin(5\pi/6)]$, $\mathbf{G}_s = \mathbf{G}_{sK2} \equiv 4\pi/(\sqrt{3}a_s)[\cos(5\pi/6+\theta), \sin(5\pi/6+\theta)]$, and $\mathbf{q}_{3K}$ by taking $\mathbf{G}_g = \mathbf{G}_{g3} \equiv 4\pi/(\sqrt{3}a_g)[\cos(7\pi/6), \sin(7\pi/6)]$, $\mathbf{G}_s = \mathbf{G}_{sK3} \equiv 4\pi/(\sqrt{3}a_s)[\cos(7\pi/6+\theta), \sin(7\pi/6+\theta)]$.

When the graphene's low energy states are close to the Γ pocket of $NbSe_2$'s second BZ the smallest possible value of $|\mathbf{q}|$ is $|\mathbf{K}_g - \mathbf{G}_s|$ with $\mathbf{G}_s = 4\pi/(\sqrt{3}a_s)[\cos(-\pi/6+\theta), \sin(-\pi/6+\theta)]$. As before, considering the C_{3v} symmetry, there are three vectors $\mathbf{q}_{i\Gamma}$ with this magnitude: $\mathbf{q}_{1\Gamma}$ obtained by taking $\mathbf{G}_g = 0$, $\mathbf{G}_s = \mathbf{G}_{s\Gamma 1} \equiv 4\pi/(\sqrt{3}a_s)[\cos(-\pi/6+\theta), \sin(-\pi/6+\theta)]$, $\mathbf{q}_{2\Gamma}$ obtained by taking $\mathbf{G}_g = \mathbf{G}_{g2}$, $\mathbf{G}_s = \mathbf{G}_{s\Gamma 2} \equiv 4\pi/(\sqrt{3}a_s)[\cos(\pi/2+\theta), \sin(\pi/2+\theta)]$, and $\mathbf{q}_{3\Gamma}$ obtained by taking $\mathbf{G}_g = \mathbf{G}_{g3}$, $\mathbf{G}_s = \mathbf{G}_{s\Gamma 3} \equiv 4\pi/(\sqrt{3}a_s)[\cos(7\pi/6+\theta), \sin(7\pi/6+\theta)]$,

By retaining only the tunneling terms for which $t(\mathbf{p}_g+\mathbf{G}_g)$ is largest, when considering the graphene states close to the $\mathbf{K}_g$ point so that $H_g = H_{\mathbf{K}_g}$, we can rewrite $\hat{H}_t$ as

$$\hat{H}_t = \sum_{i=1}^{3} c^{\dagger}_{\mathbf{k}_g\tau\sigma} T^{\dagger}_{\mathbf{K}_g,i,\tau\sigma\sigma'} d_{\mathbf{k}_g+\mathbf{q}_i,\sigma'} + h.c. \tag{3.17}$$

with:

$$T^{\dagger}_{\mathbf{K}_g,1} = \begin{bmatrix} t & 0 & t & 0 \\ 0 & t & 0 & t \end{bmatrix} \tag{3.18}$$

$$T^{\dagger}_{\mathbf{K}_g,2} = \begin{bmatrix} t & 0 & te^{-i\mathbf{G}_{g2}\cdot\mathbf{d}_B} & 0 \\ 0 & t & 0 & te^{-i\mathbf{G}_{g2}\cdot\mathbf{d}_B} \end{bmatrix} \tag{3.19}$$

$$T^{\dagger}_{\mathbf{K}_g,3} = \begin{bmatrix} t & 0 & te^{-i\mathbf{G}_{g3}\cdot\mathbf{d}_B} & 0 \\ 0 & t & 0 & te^{-i\mathbf{G}_{g3}\cdot\mathbf{d}_B} \end{bmatrix}. \tag{3.20}$$

In the remainder, supported by DFT results, we take t to be the same both when the graphene's low energy states tunnel into states around the $\mathbf{K}$ ($\mathbf{K}'$) point and the Γ point of $NbSe_2$. Let $\gamma \equiv t/\hbar v_F|\mathbf{q}_i|$. When $\gamma < 1$ we can develop a perturbative approach in which γ is the small parameter [84, 83]: terms of order γ^n correspond n-tuple tunneling processes. For our situation, as we show in the following section, $\gamma \ll 1$ and so we can retain just the lowest order terms in γ.

It is convenient to define the following spinors:

$$\begin{aligned} C^{\dagger}_{\mathbf{k}} &= (c^{\dagger}_{\mathbf{k}A\uparrow}, c^{\dagger}_{\mathbf{k}A\downarrow}, c^{\dagger}_{\mathbf{k}B\uparrow}, c^{\dagger}_{\mathbf{k}B\downarrow}); \\ D^{\dagger}_{\Gamma\mathbf{k}} &= (d^{\dagger}_{\mathbf{k}\uparrow}, d^{\dagger}_{\mathbf{k}\downarrow}); \\ D^{\dagger}_{K,\mathbf{k}} &= (d^{\dagger}_{\mathbf{K}_s+\mathbf{k}\uparrow}, d^{\dagger}_{\mathbf{K}_s+\mathbf{k}\downarrow}); \\ \Psi^{\dagger}_{K_g\Gamma_s\mathbf{k}} &= (C^{\dagger}_{\mathbf{k}}, D^{\dagger}_{\Gamma,\mathbf{k}+\mathbf{q}_{1\Gamma}}, D^{\dagger}_{\Gamma,\mathbf{k}+\mathbf{q}_{2\Gamma}}, D^{\dagger}_{\Gamma,\mathbf{k}+\mathbf{q}_{3\Gamma}}); \\ \Psi^{\dagger}_{K_gK_s,\mathbf{k}} &= (C^{\dagger}_{\mathbf{k}}, D^{\dagger}_{K,\mathbf{k}+\mathbf{q}_{1K}}, D^{\dagger}_{K,\mathbf{k}+\mathbf{q}_{2K}}, D^{\dagger}_{K,\mathbf{k}+\mathbf{q}_{3K}}). \end{aligned}$$

For the case when the graphene's FS overlaps with the $NbSe_2$'s pocket close to the K point, we can then express the Hamiltonian for the graphene-$NbSe_2$ system as $\hat{H}_{K_gK_s} = \sum_{\mathbf{k}} \Psi^{\dagger}_{\mathbf{k},K_gK_s} H_{K_gK_s}(\mathbf{k}) \Psi_{\mathbf{k},K_gK_s}$ with

$$H_{K_gK_s}(\mathbf{k}) = \begin{bmatrix} H_{\mathbf{K}_g}(\mathbf{k}) & T_{\mathbf{K}_g,1} & T_{\mathbf{K}_g,2} & T_{\mathbf{K}_g,3} \\ T^{\dagger}_{\mathbf{K}_g,1} & H_{\mathbf{K}_s+\mathbf{G}_{sK1}}(\mathbf{k}+\mathbf{q}_{1K}) & 0 & 0 \\ T^{\dagger}_{\mathbf{K}_g,2} & 0 & H_{\mathbf{K}_s+\mathbf{G}_{sK2}}(\mathbf{k}+\mathbf{q}_{2K}) & 0 \\ T^{\dagger}_{\mathbf{K}_g,3} & 0 & 0 & H^{S}_{\mathbf{K}_s+\mathbf{G}_{sK3}}(\mathbf{k}+\mathbf{q}_{3K}) \end{bmatrix} \tag{3.21}$$

For the case when we consider graphene states close to the $\mathbf{K}'_g$ point, so that $H_g = H_{\mathbf{K}'_g}$, the expression of the Hamiltonian matrix $H_{K'_gK'_s}(\mathbf{k})$ for the graphene-$NbSe_2$ system, within the approximations described above, can be obtained from Eq. (3.21) by doing the following substituions: $\mathbf{K}_s \to \mathbf{K}'_s$, $\mathbf{G}_{gi} \to -\mathbf{G}_{gi}$, $\mathbf{G}_{si} \to -\mathbf{G}_{si}$, $\mathbf{q}_{iK} \to -\mathbf{q}_{iK}$ and noticing that $T_{\mathbf{K}'_g,i} = T^{*}_{\mathbf{K}_g,i}$. Similarly, when the low energy states of graphene are close to the Γ point of $NbSe_2$ the Hamiltonian $H_{K_g\Gamma}(\mathbf{k})$ ($H_{K'_g\Gamma}(\mathbf{k})$) is obtained from the expression (3.21) for $H_{K_gK_s}(\mathbf{k})$ via the substitutions $\mathbf{K}_s + \mathbf{G}_{sKi} \to \mathbf{G}_{s\Gamma i}$ ($\mathbf{K}'_s - \mathbf{G}_{sKi} \to -\mathbf{G}_{s\Gamma i}$), and $\mathbf{q}_{iK} \to \mathbf{q}_{i\Gamma}$ ($\mathbf{q}'_{iK} \to -\mathbf{q}_{i\Gamma}$).

Including the superconducting pairing, the effective low-energy Hamiltonian for $NbSe_2$ for states close to the Γ point takes the form

$$\hat{H}^{(\mathrm{SC})}_{\Gamma_s} = \sum_{\mathbf{k}} \Psi^{\dagger}_{\mathbf{k}s} H^{(\mathrm{SC})}_{\Gamma_s} \Psi_{\mathbf{k}s}, \tag{3.22}$$

where $\Psi^{\dagger}_{\mathbf{k}s}$ is the Nambu spinor $\Psi^{\dagger}_{\mathbf{k}s} = (D^{\dagger}_{\mathbf{k}}, D_{-\mathbf{k}})$,

$$H^{(\mathrm{SC})}_{\Gamma_s} = \begin{bmatrix} H_{\Gamma_s}(\mathbf{k}) & i\Delta_{\Gamma}\sigma_2 \\ -i\Delta_{\Gamma}\sigma^{*}_2 & -H^{T}_{\Gamma_s}(-\mathbf{k}) \end{bmatrix}, \tag{3.23}$$

$H_{\Gamma_s}(\mathbf{k})$ is given by Eq. (3.5), and Δ_Γ is the size of the superconducting gap of $NbSe_2$ close to the Γ point.

For states close to $\mathbf{K}_s$, including the superconducting pairing, the Hamiltonian for $NbSe_2$ becomes

$$\hat{H}_{sK}^{(\mathrm{SC})} = \sum_{\mathbf{k}_n} \Psi_{\mathbf{k}_s}^\dagger H_{sK}^{(\mathrm{SC})} \Psi_{\mathbf{k}_s}, \tag{3.24}$$

where now $\mathbf{k}$ ($-\mathbf{k}$) is understood to be measured from $\mathbf{K}_s$ ($\mathbf{K}'_s$), and

$$H_{sK}^{(\mathrm{SC})} = \begin{bmatrix} H_{s\mathbf{K}_s}(\mathbf{k}) & i\Delta_K\sigma_2 \\ -i\Delta_K\sigma_2^* & -H_{s\mathbf{K}'_s}^T(-\mathbf{k}) \end{bmatrix}, \tag{3.25}$$

$H_{s\mathbf{K}_s}(\mathbf{k})$, $H_{s\mathbf{K}'_s}(\mathbf{k})$ are given by Eq. (3.8).

For monolayer $NbSe_2$ the superconducting gap is expected to have the same value, Δ, on the Γ and K pocket. In the remainder we conservatively assume $\Delta = 0.5$ meV [76].

The Hamiltonian for the graphene-$NbSe_2$ system including the superconducting pairing in $NbSe_2$. For the case when $\mathbf{K}_g$ is close to $\mathbf{K}_s$ the Hamiltonian becomes $\hat{H}_{K_gK_s}^{(\mathrm{SC})} = \sum_{\mathbf{k}} \Psi_{K_gK_s,SC,\mathbf{k}}^\dagger H_{K_gK_s}^{(\mathrm{SC})}(\mathbf{k}) \Psi_{K_gK_s,SC,\mathbf{k}}$, with $\Psi_{K_gK_s,SC,\mathbf{k}}^\dagger = (\Psi_{K_gK_s,\mathbf{k}}^\dagger, \Psi_{K'_gK'_s,-\mathbf{k}}^T)$,

$$H_{K_gK_s}^{(\mathrm{SC})}(\mathbf{k}) = \begin{bmatrix} H_{K_gK_s}(\mathbf{k}) & \Delta_K\Lambda \\ \Delta_K\Lambda^\dagger & -H_{K'_gK'_s}^T(-\mathbf{k}) \end{bmatrix}, \tag{3.26}$$

and

$$\Lambda = \begin{bmatrix} 0_{4\times4} & 0_{4\times2} & 0_{4\times2} & 0_{4\times2} \\ 0_{2\times4} & i\sigma_2 & 0_{2\times2} & 0_{2\times2} \\ 0_{2\times4} & 0_{2\times2} & i\sigma_2 & 0_{2\times2} \\ 0_{2\times4} & 0_{2\times2} & 0_{2\times2} & i\sigma_2 \end{bmatrix} \tag{3.27}$$

where $0_{m\times n}$ is the zero matrix with m rows and n columns.

Similarly, for the case when the low energy states of graphene are close to the Γ point of the extended BZ of $NbSe_2$ the Hamiltonian for the whole system becomes $\hat{H}^{(\mathrm{SC})}_{K_g\Gamma_s} = \sum_{\mathbf{k}} \Psi^{\dagger}_{K_g\Gamma_s,SC,\mathbf{k}} H^{(\mathrm{SC})}_{K_g\Gamma_s}(\mathbf{k}) \Psi_{K_g\Gamma_s,SC,\mathbf{k}}$, with $\Psi^{\dagger}_{K_g\Gamma_s,SC,\mathbf{k}} = (\Psi^{\dagger}_{K_g\Gamma_s,\mathbf{k}}, \Psi^{T}_{K'_g\Gamma_s,-\mathbf{k}})$,

$$H^{(\mathrm{SC})}_{K_g\Gamma}(\mathbf{k}) = \begin{bmatrix} H_{K_g\Gamma}(\mathbf{k}) & \Delta_{\Gamma}\Lambda \\ \Delta_{\Gamma}\Lambda^{\dagger} & -H^{T}_{K'_g\Gamma}(-\mathbf{k}) \end{bmatrix}. \tag{3.28}$$

3.2 Results

The large lattice mismatch between graphene and $NbSe_2$ would suggest that even in the absence of any twist angle the electronic states of the two systems would not hybridize. However, this does not take into account the large size of $NbSe_2$'s Fermi pockets. As shown in Fig. 3.2 there is a large set of values of θ for which the Dirac point of graphene intersects the $NbSe_2$'s FS either around the K points, or around the Γ point in the repeated zone scheme. For these points the electronic states of graphene and $NbSe_2$ are expected to hybridize.

From the results shown in Fig. 3.2 we see that for small values of θ, we can expect that the graphene's low energy states close to the Dirac point will hybridize with the $NbSe_2$'s states close to the K point. For values of θ close to 30° we see that graphene's states will hybridize with $NbSe_2$'s states close to the Γ point. For this reason, to estimate the charge transfer and the strength of the graphene-$NbSe_2$ tunneling in the two situations, we performed ab-initio calculations for a commensurate heterostructure with $\theta = -5.2°$, and one with $\theta = 33.0°$. The parameters identifying these commensurate structures are given in table 3.1 and the corresponding primitive cells are shown in Fig. 3.3.

The ab-initio calculations return the band structure shown in Fig. 3.4, 3.5. In these

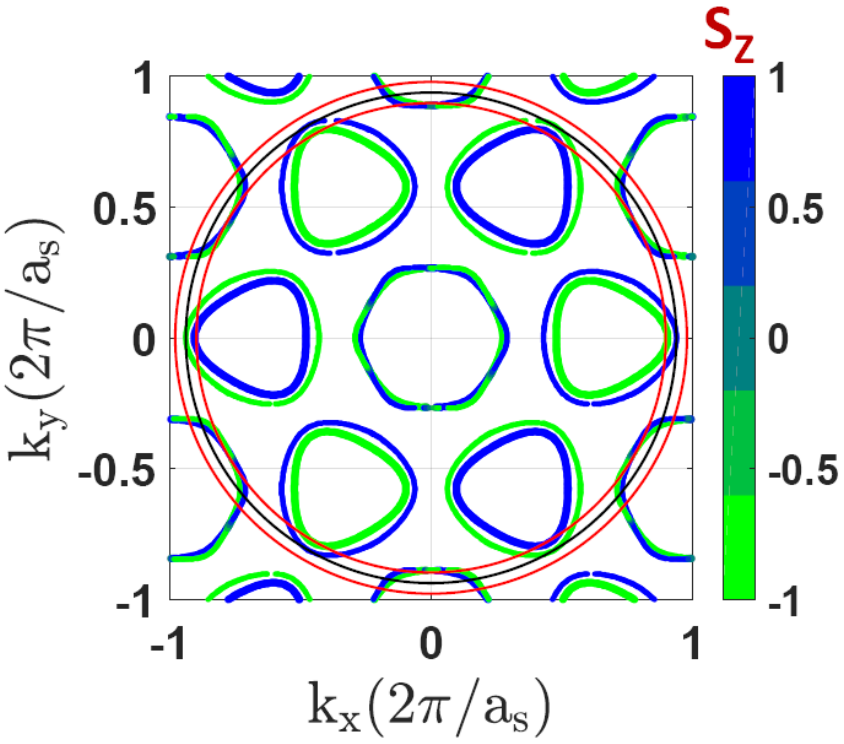

FIG. 3.2: Overlap of the Fermi surfaces of monolayer $NbSe_2$ and graphene. The blue (green) FSs are the $NbSe_2$ FSs for spin up (down) respectively, the black circle shows the position of the graphene Dirac point for all the possible twist angles, and the red circles show the region within which the graphene FS is confined as the twist angle is varied.

TMD	(m_1, m_2, n_1, n_2)	a_s(Å)	a_g(Å)	$\%\delta a_g$	θ	$\lvert A\rvert$(Å)	d(Å)	$\mu_G(eV)$
$NbSe_2$	$(-2, 1, -4, -3)$	3.48 [62]	2.55	3.7%	-5.2^0	9.2	3.57	-0.40
$NbSe_2$	$(-1, 2, 1, 4)$	3.48 [62]	2.55	3.7%	33.0^0	9.2	3.57	-0.40

TABLE 3.1: Parameters for graphene-$NbSe_2$ commensurate structures.

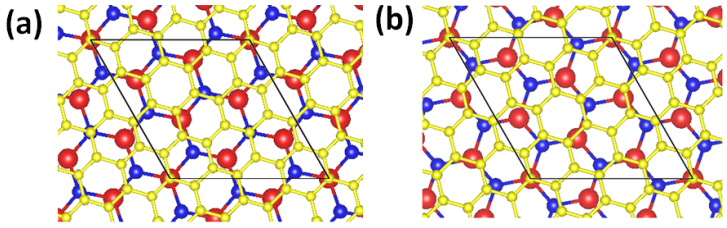

FIG. 3.3: Commensurate graphene-$NbSe_2$ structure corresponding to the parameters listed in Table 3.1. (a) is the configuration for $\theta = -5.2^0$. (b) is the configuration for $\theta = 33.0^0$. The red (blue) spheres show Nb (Se) atoms, the graphene lattice is shown in yellow.

figures the dashed blue lines show the bands of isolated graphene. The left panels show the results obtained without including spin-orbit effects and the right panels the results obtained taking into account the presence of spin orbit coupling. Panels (c) and (d) show an enlargement at low energies of the results shown in panels (a) and (b).

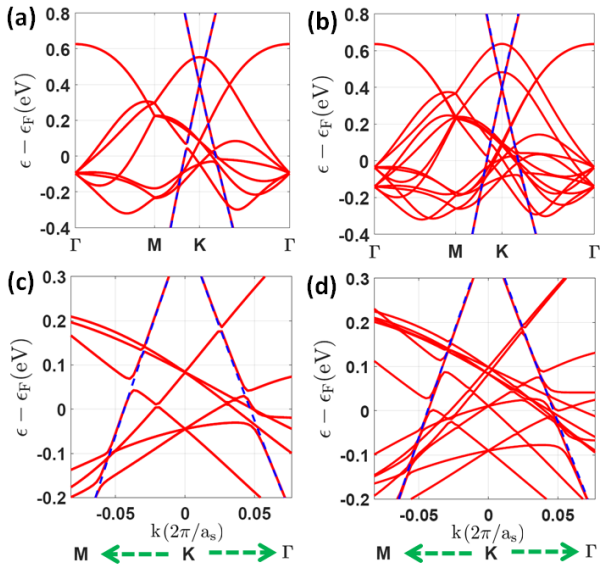

FIG. 3.4: Bands for the commensurate graphene-$NbSe_2$ structure shown in Fig. 3.3 (a) for which $\theta = -5.2°$ so that graphene's FS overlaps with $NbSe_2$'s FS pocket around the **K** point. (a) No SOC, (b) with SOC. (c): low energy detail of (a). (d): low energy detail of (b).

The results of Fig. 3.4, 3.5 clearly show that there is a significant charge transfer between graphene and monolayer $NbSe_2$ resulting in hole doping of the graphene sheet corresponding to a Fermi energy of about -0.4 eV. They also show that the amount of charge transfer does not depend on the value of the twist angle θ. Considering the finite extension of the graphene's FS due to the charge-transfer shown in Fig. 3.4 3.5 between $NbSe_2$ and graphene, we obtain that there is a significant range of values of θ for which the graphene's FS intersects the $NbSe_2$ FS and for which we can then expect non-negligible hybridization of the graphene's and $NbSe_2$ states. This is shown in Fig. 3.2 in which the red circles delimit the boundaries of the graphene's FS as θ is varied. Table 3.2 shows the

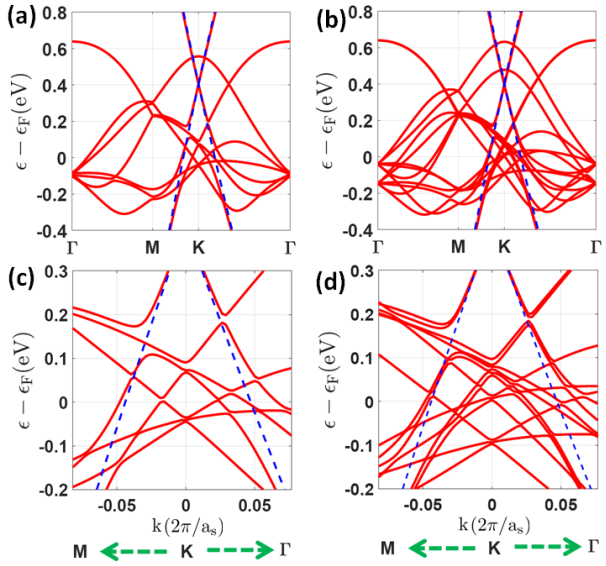

FIG. 3.5: Bands for the commensurate graphene-$NbSe_2$ structure shown in Fig. 3.3 (b) for which $\theta = 33^\circ$ so that graphene's FS overlaps with $NbSe_2$'s FS pocket around the Γ point. (a) No SOC, (b) with SOC. (c): low energy detail of (a). (d): low energy detail of (b).

range of values of θ extracted from Fig. 3.2 for which the graphene's FS is expected to intersect either one of the $NbSe_2$'s FS pockets around the K (K') point, or around the Γ point. In this table $\theta_m(K)$ ($\theta_m(\Gamma)$) is the angle in the middle of the range $2\delta\theta(K)$ ($2\delta\theta(\Gamma)$) of angles for which the graphene's FS intersects the $NbSe_2$'s FS.

TMD (1L)	$\theta_{\rm m}$(K)	$\delta\theta$(K)	$\theta_{\rm m}(\Gamma)$	$\delta\theta(\Gamma)$
$NbSe_2$	$0^0 + n * 60^0$	7.2^0	$21.9^0 + n * 60^0$	3.9^0
			$37.5^0 + n * 60^0$	3.9^0

TABLE 3.2: Values of the twist angle θ for which the graphene's FS overlap with $NbSe_2$'s FS pocket around the K point or Γ point. For $\theta_{\rm m}(\mathrm{K}) - \delta\theta(\mathrm{K}) \leq \theta \leq \theta_{\rm m}(\mathrm{K}) + \delta\theta(\mathrm{K})$, $\theta_{\rm m}(\Gamma) - \delta\theta(\Gamma) \leq \theta \leq \theta_{\rm m}(\Gamma) + \delta\theta(\Gamma)$, graphene's FS overlaps $NbSe_2$'s K pocket, Γ pocket, respectively. n is an integer between 0 and 5.

The ab-initio results allow us also to estimate the strength of the tunneling between graphene and $NbSe_2$. In Figs. 3.4 (c), (d), 3.5 (c), (d) we can see the avoided crossings close to the Fermi energy between the graphene's and $NbSe_2$'s bands. The amplitude of such crossings provides an estimate of the tunneling strength t between the graphene

sheet and the monolayer of $NbSe_2$. We find that both for the case when the graphene's FS intersects the $NbSe_2$'s pocket around the **K** point and when it intersects the $NbSe_2$'s FS pocket around the Γ point, $t \approx 20$ meV and so in the remainder we set $t = 20$ meV.

We first consider the case when graphene's FS intersects the FS pocket of $NbSe_2$ close to the K point, i.e. $-7.2^\circ < \theta < 7.2^\circ$, and $\Delta = 0$. Figure 3.6 shows the results for the FS of the hybridized system in the limit when no superconducting pairing is present in $NbSe_2$: the left (right) column shows the FS around the **K** (**K′**) of graphene. Figure 3.6 (a), (b) show the relative position in momentum space of graphene's FS and $NbSe_2$'s FS for the case when $\theta = 0$ and $t = 0$, taking into account the "folding" of the $NbSe_2$'s FS pockets due to the fact that the three **K** (**K′**) corners of the BZ are equivalent. The graphene FS is shown in red and the spin splitted $NbSe_2$'s FS in blue and green. We use this color-convention throughout this work. A zoom closer to the graphene's K point, Figs 3.6 (c), (d), clearly shows the overlap of the graphene's FS with the $NbSe_2$' FS pockets. When $t \neq 0$ the graphene's and $NbSe_2$'s states hybridize giving rise to the reconstructed FSs shown in Fig. 3.6 (e), (f). Figures 3.6 (e), (f) show that the graphene's FS, due to the hybridization with $NbSe_2$, becomes spin split.

Figure 3.7 shows the results for the case when $\theta = 2^\circ$, left column, and $\theta = 6^\circ$, right columns. For these values of the twist angle the low energy states of graphene are still close to the low energy states of $NbSe_2$ located around $NbSe_2$'s K points. For $\theta = 2^\circ$ the graphene's and $NbSe_2$'s low energy states are still close enough (in momentum and energy) that, for $t = 20$ meV, the hybridization is strong enough to significantly modify the FS of the combined system, as shown in Fig 3.7 (c), obtained setting $\Delta = 0$. For $\theta = 6^\circ$ the graphene's and $NbSe_2$'s FSs are tangent at isolated points as shown in Fig. 3.7 (b). As a consequence, when $t \neq 0$ the states at the FS of graphene and $NbSe_2$ only hybridize around these "tangent-points", as shown in Fig. 3.7 (d) obtained for $t = 20$ meV and $\Delta = 0$.

We now consider the case when a superconducting gap is present in $NbSe_2$. We find

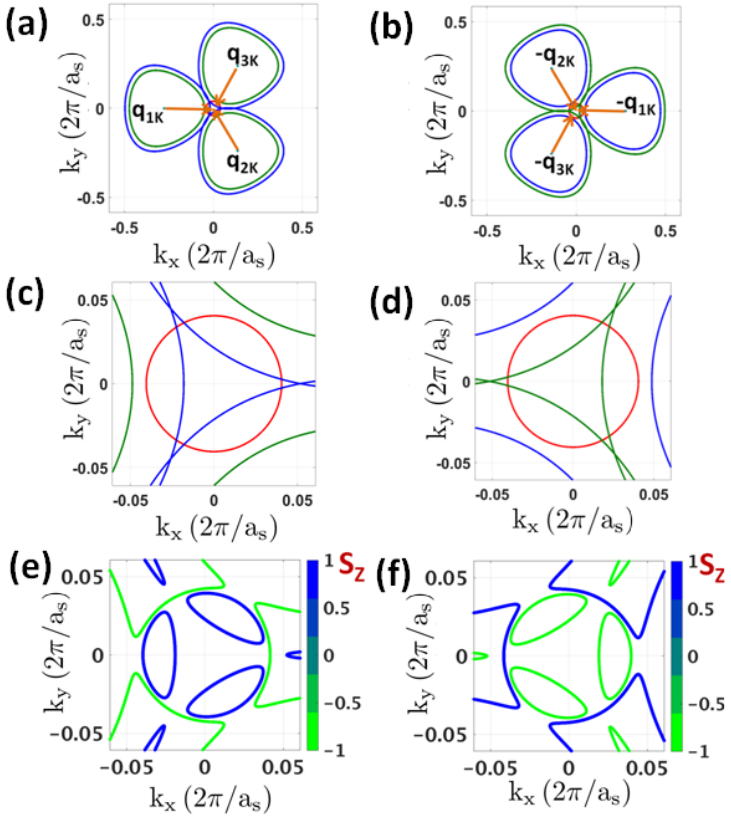

FIG. 3.6: (a) Graphene's FS at the K point (in red) and $NbSe_2$'s FS (in red and green) for $\theta = 0$, for which graphene's low energy states are close to $NbSe_2$'s K point. Because of SOC the $NbSe_2$ FS for spin-up, shown in blue is different from the $NbSe_2$'s FS for spin down, shown in green. The arrows show the vectors $\mathbf{q}_{iK}$. (b) Same as (a) but for graphene's valley around the K'point. (c), (d) zoom of (a), and (b), respectively. (e) FS of graphene-$NbSe_2$ heterostructure around graphene's K valley for the case when a finite tunneling $t = 20$ meV between graphene and $NbSe_2$ is present. (f) Same as (e) for graphene's K' valley.

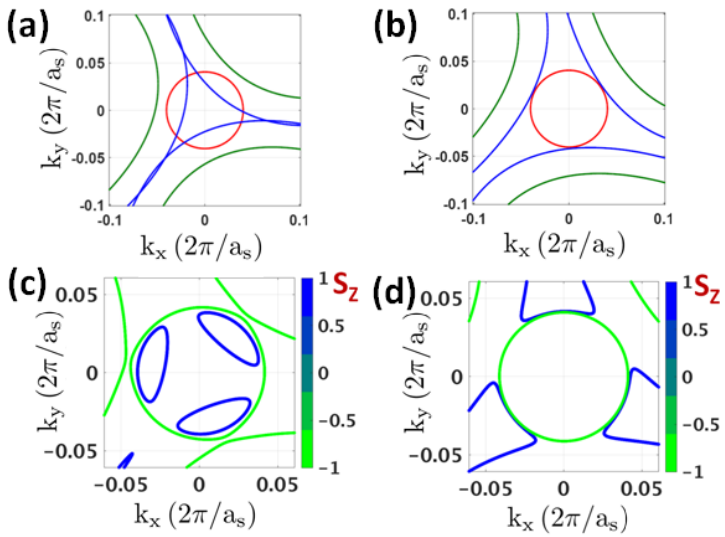

FIG. 3.7: Graphene's and $NbSe_2$'s FSs for $\theta = 2°$, (a), and $\theta = 6°$ in the limit $t = 0$. (c) FS of graphene-$NbSe_2$ heterostructure for the case when $t = 20$ meV, and $\theta = 2°$. (d) Same as (c) for $\theta = 6°$

that for $\theta = 0$ the FS is completely gapped but the gap is not uniform. Figure 3.8 (a) shows the lowest positive electron energy, E_c, as a function of $\mathbf{k}$. The smallest value of $E_c(\mathbf{k})$ corresponds to the induced superconducting gap Δ_{ind}. For $\theta = 0$ we find $\Delta_{\text{ind}} = 0.05$ meV. By calculating the smallest value of $E_c(\mathbf{k})$ for each angle $\phi_k = \arctan(k_y/k_x)$ we obtain the angular dependence of Δ_{ind}. This is shown in Fig. 3.8 (b) for the case when the twist angle is zero. We see that Δ_{ind} is strongly anisotropic, with a C_{3v} symmetry, a reflection of the structure of the reconstructed FS, Fig. 3.6 (e), 3.7 (c).

As the twist angle θ increases Δ_{ind} decreases becoming vanishing small for $\theta \gtrsim 9°$. Figure 3.8 (c) shows $E_c(\mathbf{k})$ when $\theta = 9°$. From this figure we see that the location where $E_c(\mathbf{k})$ is minumum appears to correspond to the original graphene's FS for which $|\mathbf{k}| = k_{F,g}$. A closer inspection however reveals small oscillations as a function of ϕ_k, as shown in Fig. 3.8 (d) where $E_c(\mathbf{k})$ is plotted as function of ϕ_k and $|\mathbf{k}|$ for a small range of $|\mathbf{k}|$ centered at $k_{F,g}$.

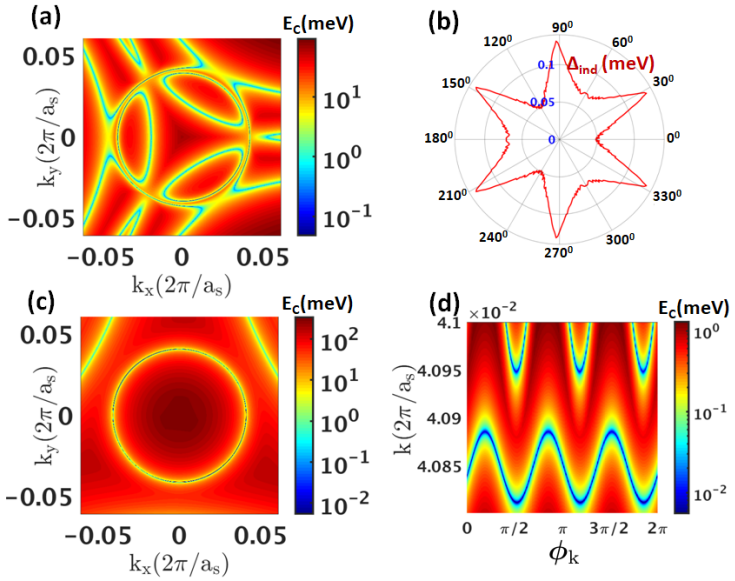

FIG. 3.8: (a) $E_c(\mathbf{k})$ for $\theta = 0$. (b) $\Delta_{\text{ind}}(\phi_k)$ for $\theta = 0$. (c) $E_c(\mathbf{k})$ for $\theta = 9°$. (d) $E_c(\phi_k, |\mathbf{k}|)$ for $\theta = 9°$ and $|\mathbf{k}|$ close to the original graphene's Fermi wave vector $k_{F,g}$.

We now consider the case when the graphene's FS touches, in the extended BZ, the $NbSe_2$'s FS pocket around the Γ point. Figure 3.9 shows the results when $\theta = 20°$, situation for which the overlap between the graphene's FS and the $NbSe_2$'s pocket at the Γ point is largest. The left row show the results for the $\mathbf{K}$ point, the right the ones for the $\mathbf{K}'$ point. Figure 3.9 (a), (b), show, on a fairly large scale, the configuration of the graphene's and $NbSe_2$' FSs, in the absence of any interlayer tunneling, and the corresponding $\mathbf{q}_i$ vectors. Figure 3.9 (c), (d) show a zoom, at small momenta, of Fig. 3.9 (a) and (b), respectively, from which we can see that the graphene's FS and the $NbSe_2$'s spin-split FS intersect at several points. At these intersections the graphene's and $NbSe_2$'s states strongly hybridize causing the FS of the system to take the form shown in Fig. 3.9 (e), (f), for the case when $t = 20$ meV, and $\Delta_\Gamma = 0$.

As θ moves away from 20° the overlap of the graphene's and $NbSe_2$'s FSs is reduced. For $\theta = 18°$ the overlap is still significant, the graphene's and $NbSe_2$'s FS still intersect,

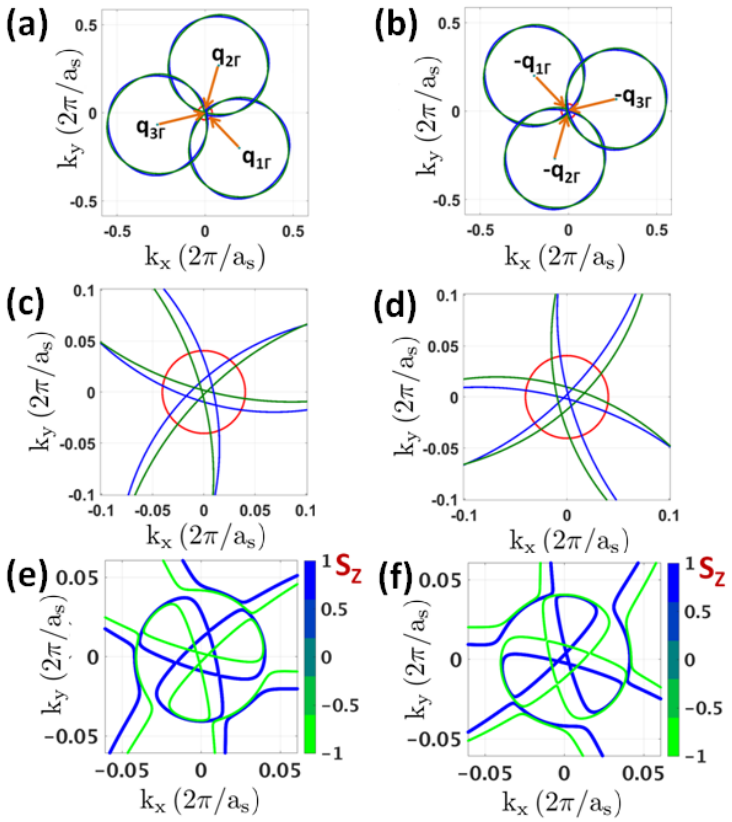

FIG. 3.9: Fermi surfaces for $\theta = 20°$, situation for graphene's FS overlaps with $NbSe_2$'s pocket Γ. Left and right panels show the results for the Dirac bands at valley K and K', respectively. (a), (b) FSs for $t = 0$. (c), (d) zoom of (a) and (b), respectively. (e), (f) FSs for $t = 20$ meV.

Fig. 3.10 (a), resulting in a significantly modified FS for the graphene-$NbSe_2$ system, Fig. 3.10 (c). For $\theta = 16°$ the graphene's and $NbSe_2$'s FSs merely touch, Fig. 3.10 (b). As a consequence the FS of the hybridized system, for $t = 20$ and Δ_Γ =0, is quite similar to the FS of the two isolated systems.

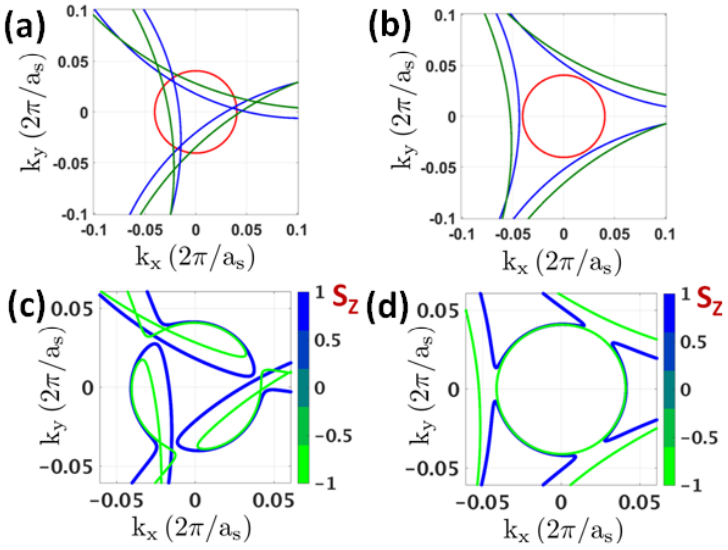

FIG. 3.10: (a) FSs for $\theta = 18°$ and $t = 0$. (b) FSs for $\theta = 16°$ and $t = 0$. (c) FSs for $\theta = 18°$ and $t = 20$ meV. (d) FSs for $\theta = 16°$ and $t = 20$ meV.

The superconducting gap on the $NbSe_2$'s Gamma pocket induces a gap in the graphene layer when θ is around 22°. Figure 3.11 (a)-(c) show the profile of $E_c(\mathbf{k})$ for $\theta = (20°, 22°, 16°)$, respectively. As θ moves away from 22° Δ_{ind} decrease. Figure 3.11 (d) show $E_c(\mathbf{k})$ as function of ϕ_k and $|\mathbf{k}|$ for a small range of $|\mathbf{k}|$ centered at $k_{F,g}$ for the case when $\theta = 16°$ and the original FSs of graphene and $NbSe_2$ barely touch. As for the case then $\theta = 9°$ we see that also for $\theta = 16°$ Δ_{ind} is very small and oscillates as function of ϕ_k for $|\mathbf{k}| \approx k_{F,g}$.

Using tunneling experiments [85, 36] it is possible to obtain the density of states, DOS, of van der Waals systems like graphene-$NbSe_2$. From the DOS it is then straightforward to extract the value of the induced superconducting gap. Figure 3.12 (a) shows the total DOS

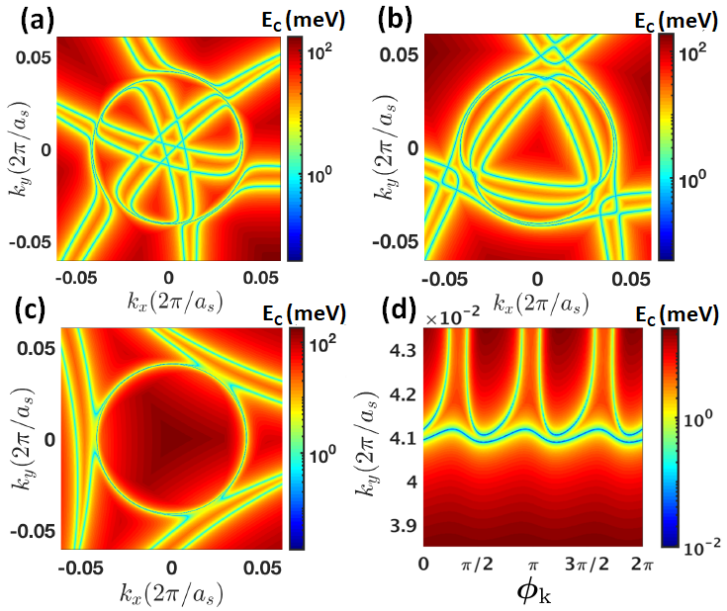

FIG. 3.11: $E_c(\mathbf{k})$ for: $\theta = 20°$, (a), $\theta = 22°$, (b), and $\theta = 16°$, (c). For $\theta = 16°$ the induced superconducting gap is very small. Panel (d) shows the value of $E_c(\phi_k, |\mathbf{k}|)$ for $\theta = 16°$.

as a function of energy on a linear-log scale. We observe the coherence peaks corresponding to the $NbSe_2$'s superconducting gap. Below such coherence peaks the DOS remains finite, because of the graphene's states, until the energy is equal to Δ_{ind}. When the energy is equal to Δ_{ind} the DOS rapidly goes to zero given that at that energy also the graphene's states become gapped. By analyzing the DOS at small energies we can find how it depends on the twist angle, as shown in Fig. 3.12 (b), and (c). Figure 3.12 (b) shows the low energy DOS for several values of θ close to zero, i.e., for the case when $\mathbf{K}_g$ is close to $\mathbf{K}_s$, and Figure 3.12 (b) shows it for several values of θ close to 20°, i.e., for the case when the $\mathbf{K}_g$ is close to Γ point of $NbSe_2$'s extended BZ.

From results like the ones showed in Figs. 3.12 (b), (c), we can extract the size of the induced superconducting gap and in particular its dependence on the twist angle, Fig. 3.13. We see that Δ_{ind} has a fairly sharp peak for $\theta = 23°$ (we used a 0.5° resolution) where it reaches the value of 0.087 meV. This is due to the fact that for $\theta \approx 23°$ there is

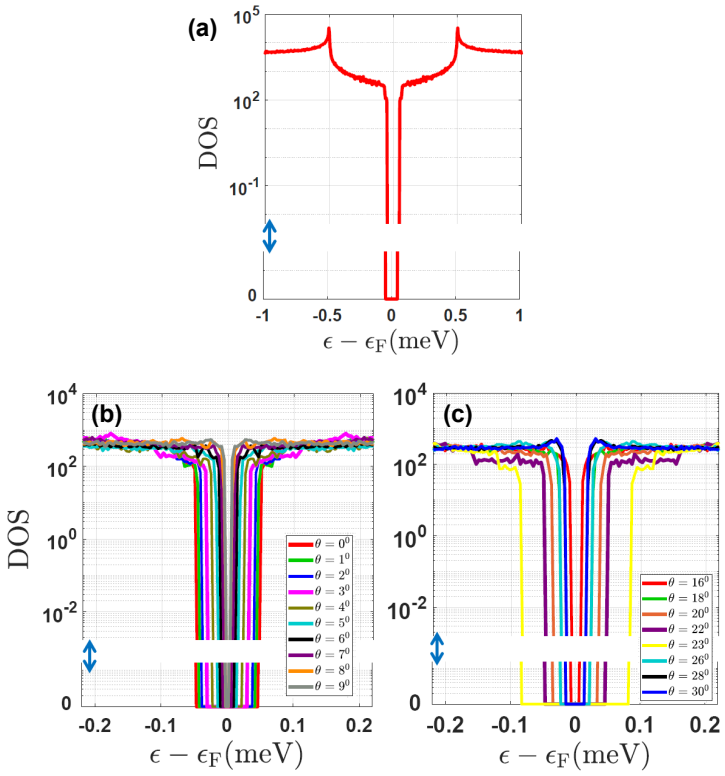

FIG. 3.12: (a) Plot full DOS for graphene-$NbSe_2$ heterostructure for $\theta = 0$.. (b) Low energy zoom of panel (a), for several values of θ for which the graphene's FS is touching $NbSe_2$ K point valley. (c) Same (b) for values of θ for which the graphene's FS overlaps with $NbSe_2$ pocket around the Γ point.

a very strong overlap of the graphene's and $NbSe_2$ Fermi surfaces. Δ_{ind} rapidly decrease as θ deviates from 23° and becomes an order of magnitude smaller when $\theta = 16°$. $\Delta_{\text{ind}}(\theta)$ has a lower and broader peak for $\theta = 0$, for wich Δ_{ind} =0.05 meV, i.e., for the situation in which the graphene's FS has the maximum overlap with the $NbSe_2$ K pockets. As θ increases from zero Δ_{ind} smoothly decreases and becomes negligible for $\theta \approx 9°$. Due to the symmetry of the system the behavior of $\Delta_{\text{ind}}(\theta)$ has a "mirror" symmetry around $\theta = 30°$ and is periodic with period equal to 60°, as exemplified by Fig. 3.13. We notice that the range of values of θ for which Δ_{ind} is not vanishingly small is larger than what we can infer by simply looking at the overlaps of the graphene's and $NbSe_2$'s FSs, Fig. 3.2. The reason is that for finite t graphene's and $NbSe_2$'s states that are within the energy window $|t|$ can still hybridize resulting in a nonzero Δ_{ind}.

Figure 3.13 shows that in a graphene-$NbSe_2$ structure the superconducting gap can be strongly tuned by varying the twist angle and that, counterintuitively, the maximum induced gap is achieved for a value of θ for which the graphene's FS overlaps with the Γ pocket of $NbSe_2$ in the second BZ.

Due to the strong spin-orbit coupling in $NbSe_2$ the in plane critical field is much larger than the field corresponding to the Pauli paramagnetic limit. Due to the fact that SOC is also induced into the graphene layer via proximity effect we find that also for graphene-$NbSe_2$ heterostructures the in plane upper critical field is much larger than the Pauli paramagnetic limit. This is shown in Fig. 3.14 in which we plot the evolution of Δ_{ind} in the presence of a Zeeman term V_z both for values of θ corresponding to the case when the graphene's FS overlaps $NbSe_2$'s K pockets (solid lines and circles), and for values of θ corresponding to the case when the graphene's FS overlaps $NbSe_2$'s Γ pocket (dashed lines and squares). We see that in both cases Δ_{ind} remains finite for V_z as large as 40 times the induced gap of the system at zero magnetic field. However, it is also evident that the suppression of Δ_{ind} due to the magnetic field is weaker, and almost independent

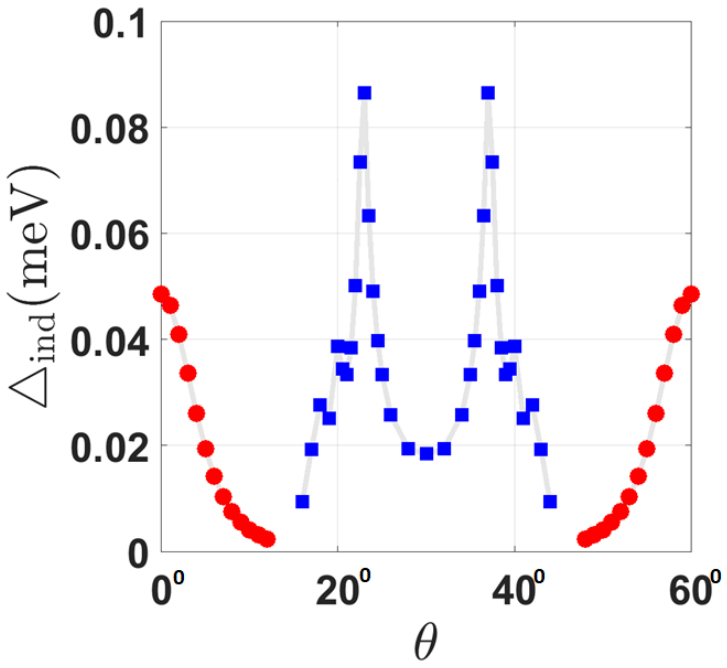

FIG. 3.13: Induced gap Δ_{ind} as a function of twist angle θ.

of θ, for the case when graphene's FS overlaps $NbSe_2$'s K pockets. This is a consequence of the fact that in $NbSe_2$ the bands' spin splitting due to SOC is much stronger for the K pockets than for the Γ pocket.

From Fig. 3.14 we notice that for $\theta = 22°$ the dependence of Δ_{ind} on the Zeeman term deviates from the dependence that we find for the other values of θ: Δ_{ind} suddenly decreases when $V_z \approx 15\Delta_{\mathrm{ind}}(V_z = 0)$, and it exhibits oscillations for larger values of V_z. The reason is that for this value of θ there are several points in momentum space for which the induced gap is close to the minimum value and, as shown in Figs. 3.15 (a)-(c), as V_Z increases the point, $\mathbf{k}^*$, in momentum space where the induced gap is minimum moves. This is in contrast to what happens for other value of θ, for which the gap is minimum always around the same points in k space, Figs. 3.15 (d), regardless of the value of V_z. This implies, for $\theta = 22°$, depending on the value of V_z the minimum gap will be located

at points with significantly different amount of SOC-induced spin splitting of the original FSs, and therefore different robustness against an in-plane magnetic field.

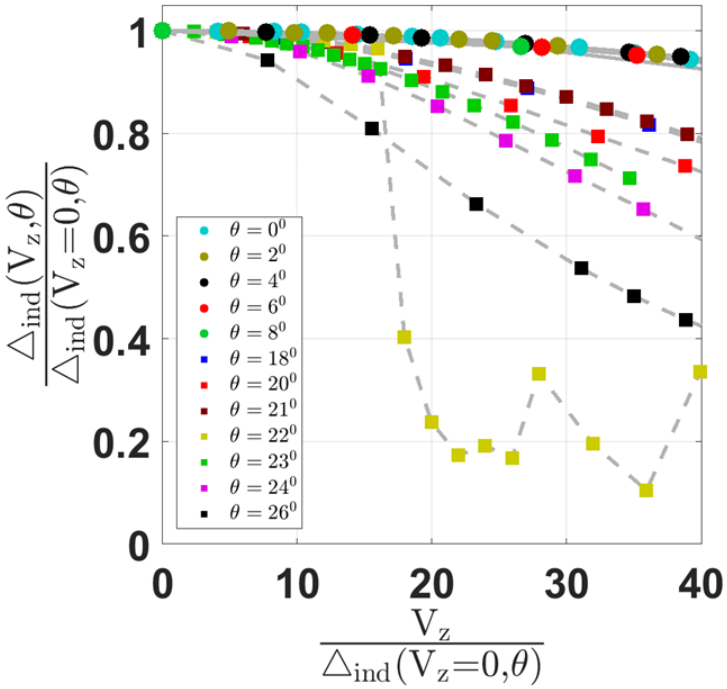

FIG. 3.14: Figure (a): Induced gap Δ_{ind} as a function of Zeeman field, V_z. The solid lines (circles) show the results for values of θ for which graphene's FS overlaps with $NbSe_2$'s K pockets. The dashed lines (squares) show the results for values of θ for which graphene's FS overlaps with $NbSe_2$'s Γ pocket.

3.3 Conclusion

In conclusion, we have shown that, despite the large lattice mismatch between graphene's and monolayer $NbSe_2$'s lattice constants, in graphene-$NbSe_2$ heterostructures, graphene exhibits a significant proximity-induced superconducting gap for a large range of stacking configurations. This is due to the fact that $NbSe_2$ has large Fermi Surface (FS) pockets that overlap with the FS of graphene for most twist angles. Using ab-initio calculations we have obtained the amount of charge transfer between graphene and $NbSe_2$ and estimated

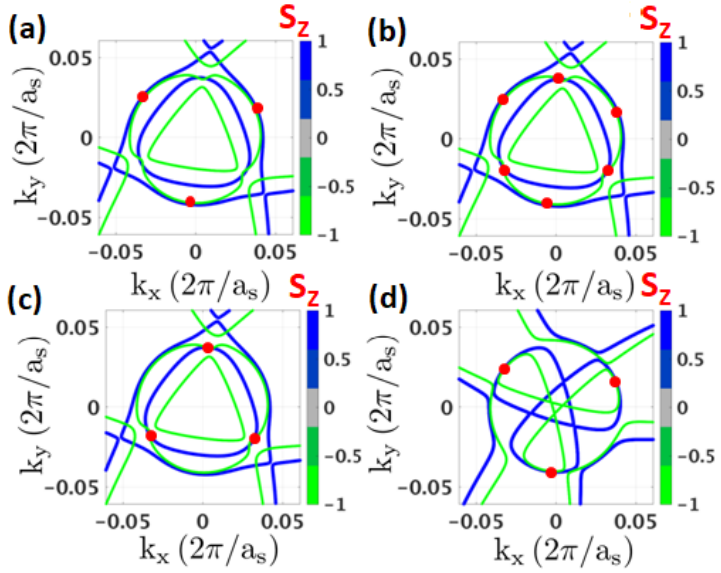

FIG. 3.15: Location $\mathbf{k}^*$ in momentum space where $\Delta_{\rm ind}$ is minimum: (a) $\theta = 22°$, $V_z = 0$; (b) $\theta = 22°$, $V_z = 14\Delta_{\rm ind}(V_z = 0)$; (c) $\theta = 22°$, $V_z = 16\Delta_{\rm ind}(V_z = 0)$; (d) $\theta = 20°$, $V_z = 0$;

the strength of the interlayer tunneling. We have then obtained a continuum model to describe the low energy electronic structure valid in the limit of small interlayer tunneling, a condition that the ab-initio results show is satisfied. The continuum model takes into account both the presence of SOC and superconducting pairing in $NbSe_2$, and the fact that, depending on the twist angle, graphene's FS overlaps either with $NbSe_2$'s FS around the **K** point or the Γ point. Using this model and the value of the parameters from ab-initio calculations, we find that, assuming conservatively the gap in $NbSe_2$ monolayer to be equal to 0.5 meV, and the graphene-$NbSe_2$ tunneling to be 20 meV, the maximum induced superconducting gap in graphene is ~ 0.09 meV, obtained for a situation when the graphene FS has maximum overlap with the $NbSe_2$'s FS around the Γ point. We have shown that the superconducting gap induced into the graphene layer is very robust to external in plane magnetic fields: the superconducting gap remains finite for values of the Zeeman term more than 40 times larger then the value of the induced gap in the absence

of magnetic fields. In addition, we have shown that such robustness strongly depends on the twist angle in the sense that if θ is such that graphene's FS overlaps with the $NbSe_2$ pockets around the K points then the induced gap is much more robust to an external in-plane magnetic field than if θ is such that the graphene's FS overlaps with the $NbSe_2$ pocket around the Γ pocket. This is a consequence of the fact that the spin-splitting of the $NbSe_2$ bands due to SOC is much stronger at the K point than at the Γ point.

The strong dependence on the external magnetic fields of the superconducting gap induced into the graphene layer is a reflection of the fact that graphene can be used, by simply varying the twist angle, as a momentum-selective probe of the electronic structure, and properties of the substrate. We can therefore envision that tunneling experiments on graphene-based heterostructures could provide very useful, momentum selective, information on the gap structure of systems with more complex gap profiles.

Considering the similarities between the Fermi surface structure of monolayer $NbSe_2$ and other transition metal dichalcogenides our results are relevant also to other graphene-TMDs heterostructures. This also applies to the case in which, instead of a monolayer, a few atomic layers TMD is used. Our results suggests that in general, for a large range of stacking configurations, the graphene and TMD states, despite the large lattice mismatch, are expected to hybridize and, when the TMD is superconducting, induce a significant superconducting gap into the graphene layer. It would be interesting to study how such proximity effect can affect the ground state of twisted-bilayer graphene systems [86, 87, 88, 89, 90].

CHAPTER 4

GNR-hBN

Graphene nanoribbons (GNRs)[47, 91, 92, 93, 51, 94, 95, 96] are almost ideal 1D electronic systems: they are only one atom thick and their width can be just a few atoms. Recent advances in bottom-up synthesis using molecular precursors allow to control with atomic precision the width and the edges' morphology of GNRs. [97, 98, 99, 100]. These developments make GNRs very promising as basal elements for the realization of quasi-1D systems and 1D topological states [101, 102]. The particular advantage of GNRs toward this goal are: (i) almost ideal 1D character, (ii) scalable synthesis and layout to create networks of quasi 1D channels, (iii) tunability of their electronic properties via edge and width engineering. Interest in 1D electronic systems has recently increased substantially given that to date the most successful and promising approaches to realize non-abelian electronic states, such as Majoranas, rely on the availability of 1D devices [103] of high quality (ideally disorder free) [104, 105, 106, 107, 108, 109, 110, 111, 112]. The ultimate 1D nature of GNRs and therefore large energy separation between their 1D subbands makes them in many respects ideal for the realization of 1D superconductor heterostructures compared to semiconductor-superconductor nanowires where in typical experimental

conditions several bands are occupied [113, 114, 115].

To be able to use GNRs to realize states like Majoranas [116] the GNRs have to be of very high quality, i.e to have a very low level of disorder. In recent years high quality hexagonal boron nitride, hBN, has emerged as the ideal dielectric to realize graphene-based heterostructures [66, 117, 118, 119, 120]. This is due to the fact that hBN has a large band gap, a very low density of impurities and crystal defects, and it can be exfoliated to be only a few atoms thick. Because of the extreme low impurity density of hBN, graphene devices in which hBN is the dielectric substrate have electron's mobilities orders of magnitude larger than graphene devices on other substrate, such as, for example, silicon dioxide [121, 122, 123, 124, 125, 126]. One additional important consequence of having a substrate with low disorder, is that in systems like graphene and bilayer graphene, it also reduces the carrier density inhomogeneities that, especially close to the Dirac point or in the presence of a small band gap, can be very large and significantly modify the electronic properties of the graphene-based device [127, 128, 129, 130, 131, 132, 74, 133, 134, 135, 136, 137, 138, 139, 75, 72]. Imaging experiments have directly shown that the use of hBN as a substrate instead of silicon oxide greatly reduces the amplitude of the disorder-induced carrier density inhomogeneities [118, 120, 86].

For all the reasons stated above it is natural to use hBN as a substrate for graphene nanoribbons. However, it has been shown both theoretically [140, 141, 142, 143, 144] and experimentally [120, 145, 146, 147, 148] that hBN can qualitatively affect the band structure of graphene. This is due to the fact that in graphene-hBN devices, because hBN has a lattice constant that is only 1.8% larger than graphene's, there can be region tens of nanometer wide in which the graphene layer is in register with the hBN lattice [149] and therefore have its sublattice symmetry broken given that in hBN the A and B sublattices create different electrostatic potentials. Given that GNRs are typically only a few atoms wide we should expect that hBN can qualitatively modify their band structure. In order

to be able to use hBN to increase the quality of GNRs to realize almost ideal 1D electronic systems, it is therefore necessary to understand how hBN can affect the spectrum of GNRs.

In this work we study how hBN modifies the band structure of GNRs. We study different types of GNRs and consider different (commensurate) stackings between the GNRs and hBN. We find that hBN can cause qualitative changes to the band structure of GNRs and that these changes can be tuned by selecting the stacking configuration. The effects are most dramatic for zig-zag graphene nanoribbons (GNRs): for such ribbons hBN in general induces a spin splitting of the conduction band (CB) and valence band (VB). We also find that the sign of such spin-splitting can be changed simply by changing, via a rigid shift, the stacking between the ZGNR and hBN.

4.1 Method

Graphene is a one-atom thick layer of carbon atoms arranged in an hexagonal structure [121, 150, 151, 126]. In graphene the carbon-carbon distance, a, is 1.46 Å. The hexagonal structure is best described as a triangular lattice with lattice constant $a_G = \sqrt{3}a$ and a basis with two sites, A and B. The atoms at sites A form the A-sublattice and the atoms at the B sites form the B-sublattice. In graphene the A and B sites are both occupied by carbon atoms and so we have sublattice symmetry. Graphene nanoribbons can be obtained by etching graphene along particular directions [152]. More recently, GNRs have been produced via bottom-up synthesis [97, 98, 99], a fabrication technique that allows to control with atomic precision the width of the ribbon and the shape of their edge and therefore their electronic properties. Depending on their edges we can identify two types of GNRs: armchair GNRs (AGNRs), Fig. 4.1 (a), in which the edges look like a sequence of armchairs, and zigzag GNRs (ZGNRs), Fig. 4.1 (b), in which the edges have a zigzag pattern. It is customary to refer to the width of an AGNR via the number N across the

transverse direction of carbon-carbon dimers aligned along the longitudinal direction. For ZGNRs the width is denoted by the number N of zigzag chains. For the remainder it is important to notice that the unit cell of AGNRs and ZGNRs is different, as shown in Fig. 4.1. Let a_{AGNR} be the nanoribbon lattice constant. For AGNRs $a_{\mathrm{AGNR}} = \sqrt{3}a_G$, for ZGNRs $a_{\mathrm{ZGNR}} = a_G$.

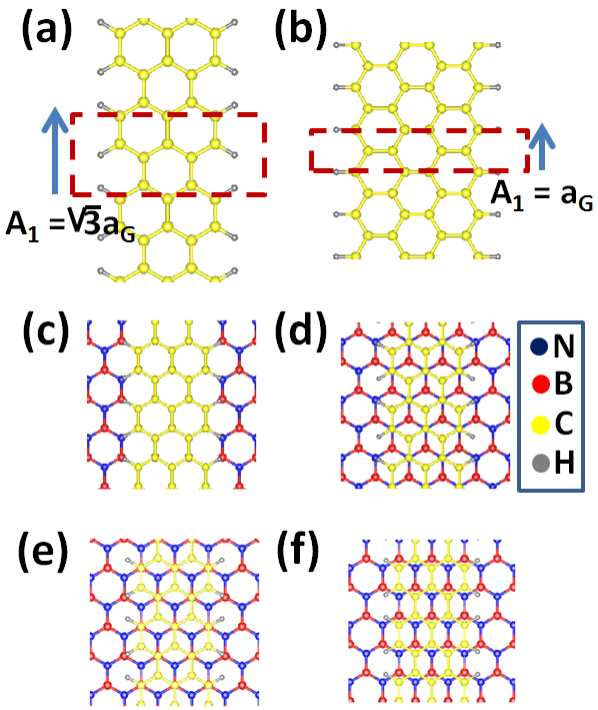

FIG. 4.1: Atoms layout for AGNR (a), and ZGNR (b). The dashed lines identify the primitive cells. (c), (d), (e), (f) possible stacking configurations between a GNR and hBN: AA, $\mathrm{AB_N}$, $\mathrm{AB_B}$, and $\mathrm{A_{br}}$, respectively.

The heterostructures that we study are formed by a graphene nanoribbon (armchair or zigzag) placed on hBN. Figure 4.1 (c-f) show some examples GNR-hBN structures. In hBN the sublattice A (B) is occupied by boron (nitrogen) atoms, or vice versa. The fact that the A and B sites are not equivalent in hBN in Fig. 4.1, and all the figures in the remainder of this work, is denoted by the fact that they are shown in different colors. In all the results presented in the remainder, to avoid the effects due to dangling bonds, we

assume the edges of the GNRs to be terminated by hydrogen atoms, shown in light grey in Fig. 4.1. It is helpful to name the particular stackings shown in Fig. 4.1. Figure 4.1 (c) shows the case in which the ribbon and the hBN are in the AA stacking configuration, i.e. the case in which the GNR's sublattice A (B) is directly above the sublattice A (B) of hBN. In the AB_N (AB_B) stacking the sublattice A (B) of the GNR is in register with the sublattice occupied by the nitrogen (boron) atoms of the substrate, Fig. 4.1 (d) (Fig. 4.1 (e)). In the bridge-stacking configuration, A_{br}, the carbon-carbon links of the GNR cross the boron-nitrogen links of the substrate, Fig. 4.1 (f).

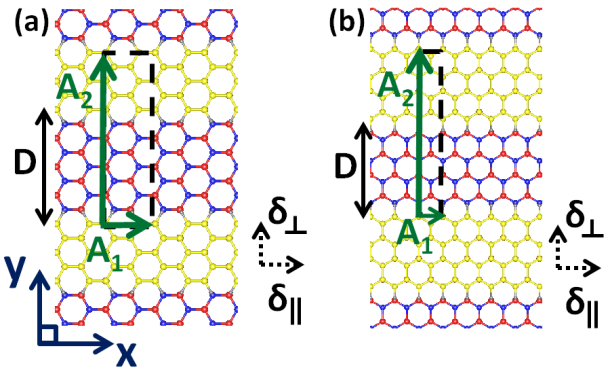

FIG. 4.2: Sketch of the supercell used for the DFT calculation. D is the distance between ribbons, and $\delta_\perp$ ($\delta_\parallel$) denote transverse (longitudinal) shifts of the GNR with respect to the hBN substrate away from AA stacking.

The tight-binding model is a computationally very efficient method that has been used to obtain the band structure of GNRs [47, 48, 153, 154] and related systems. However, to get accurate results, even qualitatively, using the tight-binding model requires a fine tuning of its parameters that can only be achieved by comparing the tight-binding model's results to the ones obtained using density functional theory (DFT) approaches [51, 155, 156, 92, 157, 94]. For the case of isolated AGNR this is exemplified by the fact that the simple nearest neighbor tight binding model with constant hopping parameter for the case in which $N = 3n - 1$ return a gapless band-structure whereas DFT shows the

presence of finite band-gap [51, 94]. The main reason for such discrepancy is that, due to the finite width of the ribbon, the hopping parameter entering the tight-binding model should not be taken to be constant across the ribbon's width [51] and hopping processes beyond next-neighbor should also be included [48]. For ZGNRs the simple tight-binding model predicts a gapless band structure, due to the presence of edge modes, a fact that is not affected by the variation of the hopping parameter across the ribbon. However, also for ZGNRs the result of the simple tight-binding model are qualitatively incorrect if one does not include the effect of the exchange part of the Coulomb interaction. The exchange interaction causes ZGNRs to have an insulating ground state with ferromagnetic order along the edges and antiferromagnetic order between the two edges, an effect that is correctly captured by ab-initio calculations [158, 51, 159]. As evidence of the significant advances in the synthesis of high quality GNRs, very recently the ZGNRs' magnetic edges states have been observed experimentally [100]

For the reasons stated above, in this work we obtain the electronic structure of all the systems via ab-initio density functional theory calculations using the Quantum Espresso package [160]. We use ultrasoft potentials and a plane-waves basis with periodic boundary conditions.

We denote as x the axis along the longitudinal direction of the GNR, as z the axis perpendicular to the heterostructure plane and as y the axis in the GNR plane perpendicular to both x and z, as shown in Fig. 4.2. $\delta_{\parallel}$ ($\delta_{\perp}$) denotes a shift along the x (y) direction between the GNR and the substrate. In order to simulate a heterostructure with an isolated GNR we need to use a supercell large enough to minimize artificial interference effects arising from the periodic boundary conditions. We find that for supercell sizes $D > 9a_G$ finite size effects are negligible and do not affect the electronic structure of the GNR. In the direction perpendicular to the plane of the GNR-hBN heterostructure we insert a "vacuum layer" 10 Å thick.

The electron exhange and correlation are calculated by implementing the generalized gradient approximation (GGA) functional of Perdew-Burke-Ernzerhof (PBE) [24]. For AGNR hybrid systems the Brillouin zone (BZ) integration is performed by generating a uniform 12x12x1 mesh of k points using the Monkhorst-Pack procedure. For ZGNR hybrid systems we use the same procedure using 16x16x1 mesh. The cut off energy wavefunction and charge densities are set to be 50 Ry and 400 Ry, respectively, ensuring the convergence of the total energy. To be able to compare the effect of different stacking configurations we keep the interlayer distance d fixed. We conservatively set $d = 3.5$Å considering that the modifications of the GNR electronic structure due to the presence of the substrate are stronger for smaller values of d. Changes in d do not change qualitatively the results that we present in remainder.

We limit ourselves to the case when the stacking between the nanoribbon and hBN is commensurate. We assume that the 1.8% lattice mismatch between the graphene nanoribbon and hBN can be neglected given the small size of the system and the fact that in graphene-hBN heterostructures it has been shown that graphene and hBN lattices can be in commensurate stacking configurations over regions tens of nanometers wide. wide [149].

4.2 Results

In this section we present our results. To better understand the results for the GNR-hBN heterostructures it is helpful to briefly review the electronic structure of isolated GNRs and hBN. Figure 4.3 shows the low-energy band structure of isolated GNRs obtained using DFT, see Sec. 4.1. Figures 4.3 (a)-(c) show the band structure for AGNRs with width $N = 3n - 1$, $N = 3n$, $N = 3n + 1$, respectively for the case when $n = 2$. As discussed in Sec. 4.1 for all three cases we have a gapped band structure. Figure 4.3 (d) shows the band structure for a ZGNR of width $N = 4$. Notice that for a ZGNR the low energy states are

located at the edge of the 1D BZ ($k = \pi/a_{\mathrm{ZGNR}}$), and the gap due to the antiferromagnetic ordering, decreases with the width of the ribbon. Here, and in the remainder, $\Delta^{(0)}$ denotes the direct band gap and $\Delta^{(1)}$ the energy splitting for $k = \pi/a_{\mathrm{ZGNR}}$. Figure 4.4 shows the low energy band structure of hBN.

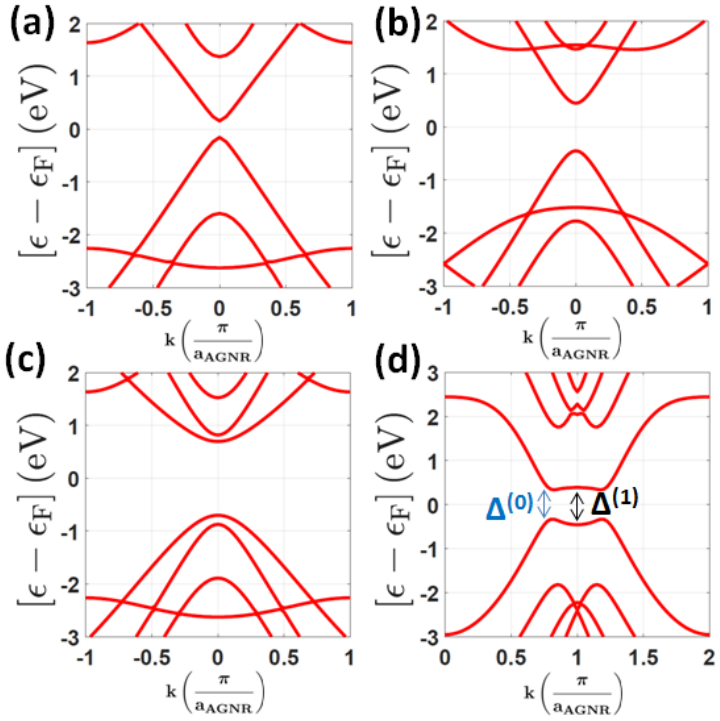

FIG. 4.3: (a) Band structure for an AGNR with N=3n-1=5, (n=2). (b) Band structure for an AGNR with N=3n=6. (c) Band structure for an AGNR with N=3n+1=7. (d) Band structure for a a ZGNR with N=4.

4.2.1 AGNR-hBN heterostructures

In this section we present the results for heterostructures formed by AGNR and hBN. Figure 4.5 (a) shows the low-energy band-structure of a AGNR-hBN heterostructure in the AA stacking configuration: here and in the remainder the dashed lines show the spectrum of the isolated GNR and the solid lines the spectrum of the heterostructure. We see that

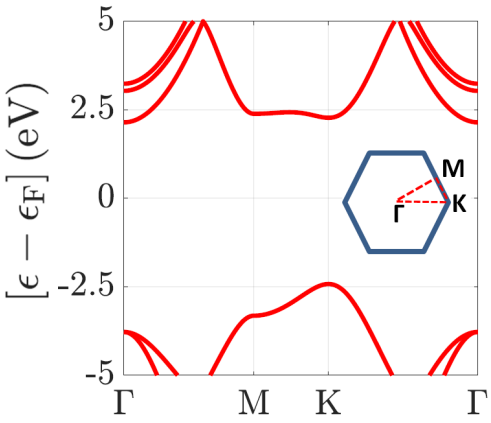

FIG. 4.4: Low energy band structure of hBN. The inset shows the Brillouin Zone.

for this configuration the presence of the hBN does not modify significantly the spectrum of the GNR. Figure 4.5 (b) shows the shift in energy of the ribbon valence and conductance band due to the presence of the hBN: we see that for this configuration the variation in energy is of the order of 15 meV close to the $k = 0$ point and slowly increases (in absolute value) as we move away from $k = 0$.

To study how differences in stacking affect the spectrum we studied the effect of a shift away from the AA configuration in the longitudinal and transverse direction. The relative change of the ribbon's band gap $\Delta_r \equiv (\Delta_h - \Delta_0)/\Delta_0$ where Δ_h is the band gap of the GNR-hBN heterostructure, can be used to show in a compact way the effect. The results are shown in Fig 4.6 for the three classes of AGNRs: $N = 3n - 1$, $N = 3n$, $N = 3n + 1$ where, as in the remainder of this work, we have taken $n = 2$. We see that a shift in the perpendicular direction has only a minor effect: the relative change is at most of the order of 2%. We also observe that the highest increase of the band gap due to $\delta_\perp$ is obtained when the shift results in the A_{br}configuration for $N = 3n-1$ and $N = 3n+1$ AGNRs and very close to it for $N = 3n$ AGNRs.

The shift in the longitudinal direction has a stronger effect than $\delta_\perp$. By varying $\delta_\parallel$ we

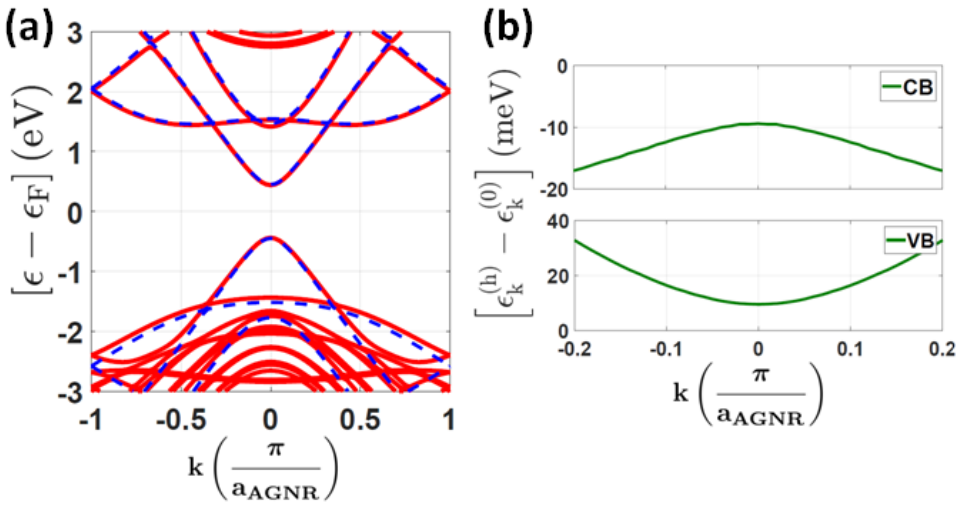

FIG. 4.5: (a) Bands of a AGNR-hBN heterostructure for a ribbon with $N = 6$ placed on hBN in the AA stacking configuration. The dashed lines show the spectrum of the isolated GNR and the solid lines the spectrum of the heterostructure. (c), (d) energy shift as a function of k of the CB, and VB, respectively.

can obtain the AB_N and AB_B configurations. Figure 4.6 shows that for all the three types of ribbons $\Delta_r(\delta_\parallel)$ has an extremum when the AB_B configuration is realized. For most cases a shift in the longitudinal direction can induce a change of the band gap of the order of 6% or less, however, for the case when $N = 3n-1$, i.e. for the class of AGNRs for which Δ_0 is the smallest (zero using a tight binding model with uniform hopping parameters) a shift in the longitudinal direction away from the AA stacking can lead to a configuration for which the band gap is reduced by 20%, i.e. about 60 meV in absolute terms. Figure 4.7 shows the atoms arrangement for this configuration, and the corresponding low-energy band-structure. We see that for this stacking the nitrogen atoms are located midway under the longitudinal C-C bonds.

We expect that graphene nanoribbons will be placed on hBN via methods (such as exfoliation) that in general lead to long-lived metastable stacking configurations that are not the thermodynamic ground state. However, it can be insightful to see which

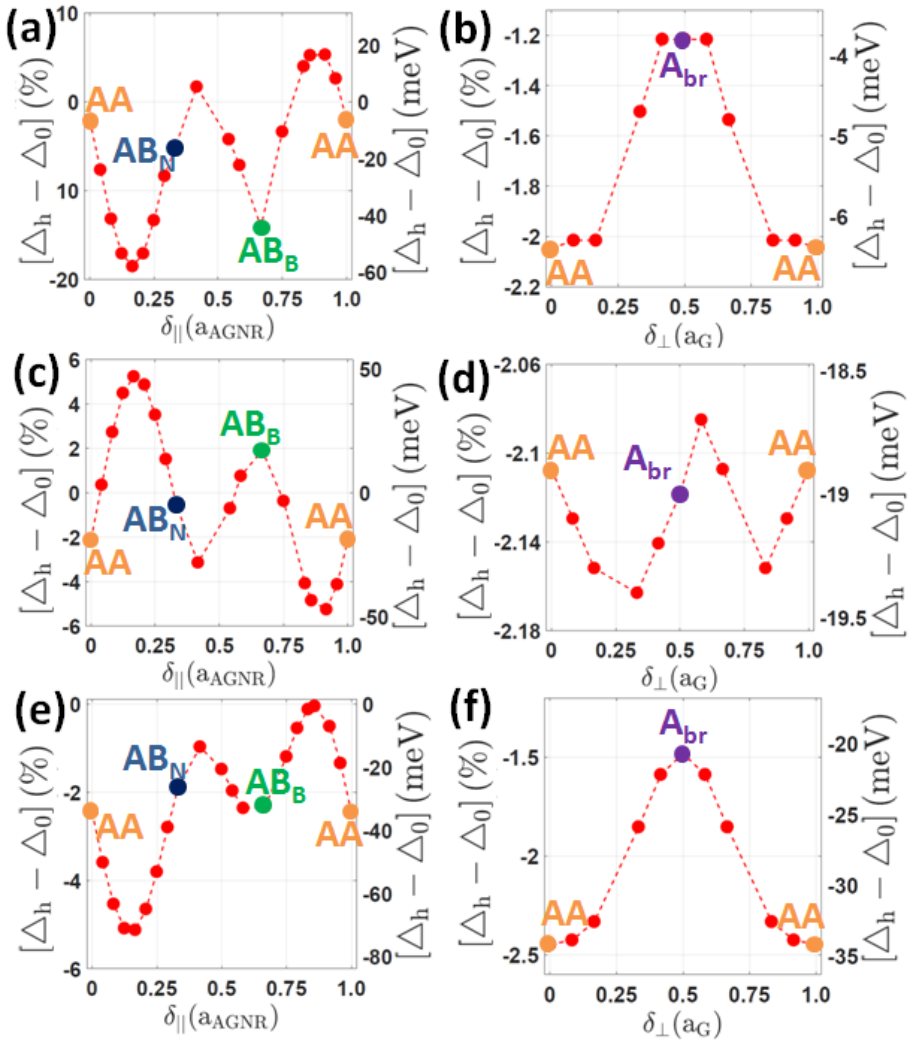

FIG. 4.6: Evolution of the band gap of a AGNR (with $n = 2$) placed on hBN as a function of shift away from AA stacking. The left panels show the results for a shift along $\delta_{||}$, the right panels for shifts along $\delta_{\perp}$. The different rows show the results for different widths of the ribbon: the first row (panels (a) and (b)) show the results for the case when $N = 3n-1 = 5$, the second (panels (c) and (d)) for the case when $N = 3n = 6$, and the last (panels (e) and (f)) for the case when $N = 3n+1 = 7$.

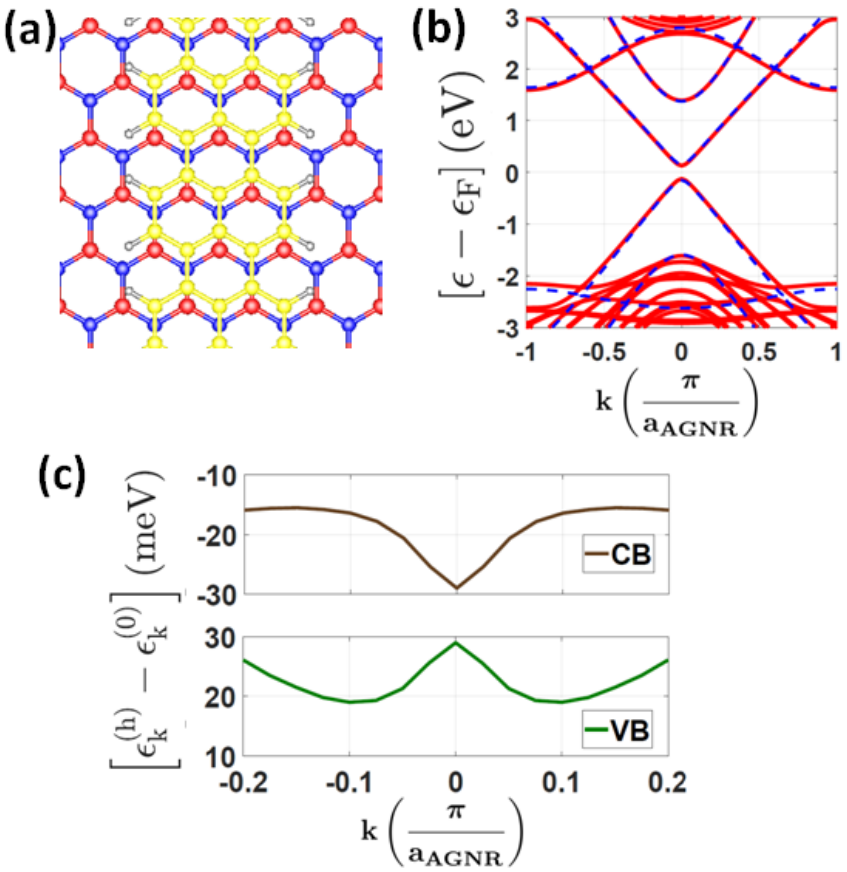

FIG. 4.7: (a) Stacking configuration for a AGNR-hBN system corresponding to the maximum gap change shown in Fig. 4.6 (a) ($N = 5$) corresponding to $\delta_{||} = 0.16\left(\frac{1}{a}\right)$. (b) Bands for the stacking configuration shown in (a) (the dashed lines show the bands for the isolated ribbon). (c) The top panel shows the difference at small k's between the heterostructure's conduction band, CB, and the isolated ribbon's CB for the stacking configuration shown in (a). The bottom panel show the difference between the VBs.

configurations, among the ones considered in Fig. 4.6, are the most stable. For this reason we calculated the change, with respect to the AA-stacking configuration, of the total energy as a function of $\delta_{\parallel}$ and $\delta_{\perp}$. Figure 4.8 show the results for the case of an AGNR with $N = 6$ (we find the same qualitative results for different values of N). This figure shows that the AB_B stacking configuration is the most stable, in agreement with previous studies of graphene on hBN [143].

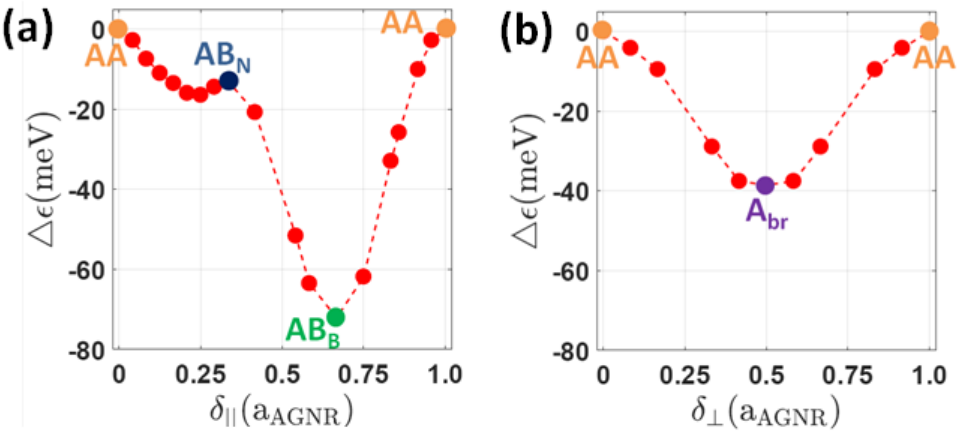

FIG. 4.8: (Color online) Change of the total energy, with respect to the case of AA stacking, as a function of $\delta_{\parallel}$ (a), and $\delta_{\perp}$ (b), for an AGNR with $N = 6$ placed on hBN

4.2.2 ZGNR-hBN heterostructures

We now consider ZGNR-hBN heterostructures. Figure 4.9 shows the low energy spectrum of a ZGNR-hBN heterostructure for the case of AA stacking. Analogously to what we find for AGNR-hBN we see that for this configuration the effect of the hBN on the band gap is small: the conduction and valence bands around $k = \frac{\pi}{a_{\mathrm{ZGNR}}}$ are shifted by 10-20 meV, Fig. 4.9 (c). However, the presence of hBN causes an important qualitative modification of the band structure: it induces a spin splitting of the valence and conduction bands, see Fig. 4.9 (d). This is due to the locking between spin and sublattice degrees

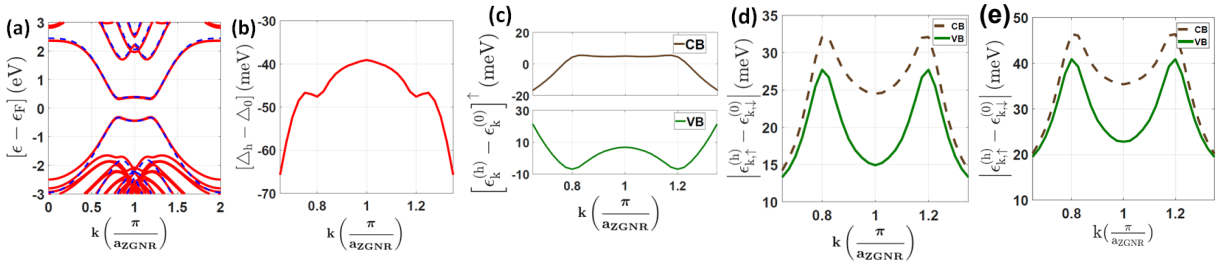

FIG. 4.9: Results for a ZGNR with ($N = 4$) placed on hBN in the AA stacking configuration. (a) Band structure, the dashed lines show the bands for the isolated ZGNR. (b) Difference, for k close to π/a_{ZGNR}, between the band gap of the hBN-ZGNR heterostructure, Δ_h, and the band gap of the isolated ZGNR Δ_0. (c) The top panel shows the difference for k close to π/a_{ZGNR} between the ZGNR-hBN heterostructure's CB and the isolated ribbon's CB for the AA stacking configuration. The bottom panel show the difference between the VBs. (d) Spin splitting as a function of k for the ZGNR-hBN heterostructure's CB and VB. (e) Same as (d) but for $d = 3.4$Å.

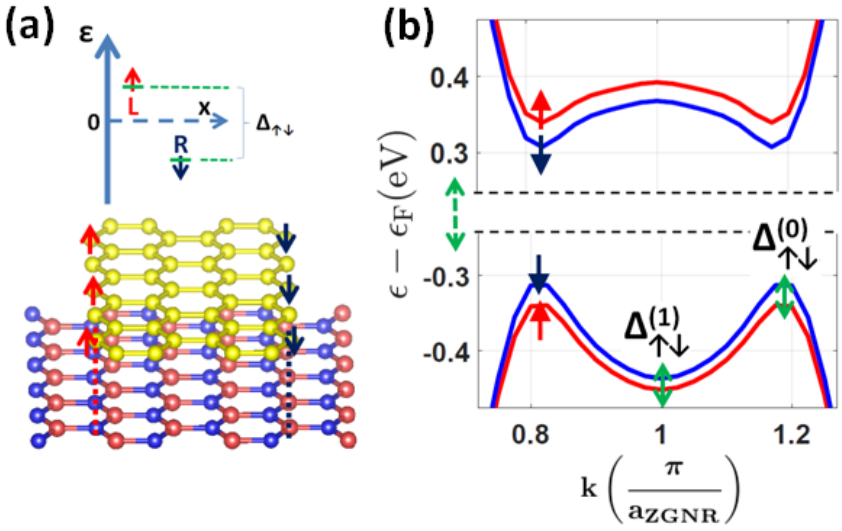

FIG. 4.10: (a) Sketch of a ZGNR placed on hBN in the AA stacking configuration. The arrows at the edges of the ZGNR show the spin polarization of the edge modes. (b) Enlargement of the VB and CB to show the spin splitting due to the presence of hBN.

of freedom for the edge states [161] and the fact that the presence of hBN breaks the GNR sublattice symmetry. For ZGNRs the left (right) edge state has spin polarization up (down) while at the same time the atoms forming the left (right) edge belong to the A (B) sublattice (or viceversa). As Fig. 4.10 shows the presence of hBN breaks the sublattice symmetry and therefore the degeneracy of the states due to this symmetry. In a ZGNR, the breaking of the sublattice symmetry therefore causes a spin splitting of the edge states, for which spin and sublattice degrees of freedom are locked. Such spin splitting is not affected qualitatively by changes in the interlayer distance d, however, changes in d have quantitative effects: as we would expect decrease of d increases the spin splitting as confirmed by the comparison of the results shown in Fig. 4.10 (e) and Fig. 4.10 (f) that were obtained using $d = 3.5$Å and $d = 3.4$Å, respectively.

The effect of the presence of hBN on the band structure of ZGNR is similar to the effect of an electric field applied along the transverse direction of a ZGNR. It was shown that for large enough transverse electric fields a ZGNR can be driven into an ideal half-metallic state [162, 163]. For the case of a ZGNR placed on hBN the difference in electrostatic potential between the ZGNR's atoms on the two different edges is not due to an external electric field but the fact that they are located above different atoms of the layer forming the substrate. The results of Figure 4.9 (d) show that hBN, and any substrate that break the sublattice symmetry of graphene, can be used to spin split the edge modes of a ZGNR. We can conclude that in ZGNR-hBN heterostructures we can break the spin-degeneracy without having to introduce an external magnetic field and explicitly breaking the time reversal symmetry. It is interesting to see if such an effect can be maximized by tuning the stacking configuration and the width of the ZGNR.

Figure 4.11 shows the effects on the ZGNR band structure of a shift along the ribbon's transverse direction away from the AA stacking configuration. We see that the reduction of $\Delta^{(0)}$ and $\Delta^{(1)}$ oscillates with $\delta_{\perp}$, Fig. 4.11 (a), (b). The spin splitting also oscillates

with $\delta_\perp$ Fig. 4.11 (c), (d), in a very similar way both around $\Delta^{(0)}$ and $\Delta^{(1)}$ for valence and conduction band. As for the band-gap the effect of the hBN on the spin splitting is minimal for the AB_B stacking configuration. Also for values of $\delta_\perp$ such that a configuration between AA and AB_N is realized the spin splitting can be tuned very close to zero. We find that by varying $\delta_\perp$ the Zeeman splitting is maximized when a configuration close to the AB_N stacking ($\delta_\perp = 0.8a_G$) or not too far from the AA stacking one ($\delta_\perp = 1.5a_G$). For these configurations the spin splitting is about 40 meV. Fig. 4.11 (e), (f) show the stacking configurations corresponding to $\delta_\perp = 0.8a_G$ and $\delta_\perp = 1.5a_G$, respectively. We see that in both cases the carbon atoms of one of the GNR sublattices are very close to the nitrogen atoms whereas the carbon atoms of the other sublattice are very close to the boron atoms. Due to the details of the electrostatic environment created by the hBN we conclude that these, among the configurations that we have considered, are the ones that maximize the breaking of the ZGNR sublattice symmetry and therefore the spin splitting of the spin polarized edge modes.

Figure 4.12 shows how the band gap and the spin splitting change by shifting the ZGNR away from the AA stacking along the longitudinal direction. As for the case of a perpendicular shift, we see that both the gap and the spin-splitting oscillate with $\delta_\parallel$. Both the gaps, $\Delta^{(0)}$ and $\Delta^{(1)}$, and the spin splitting are symmetric with respect to $(\delta_\parallel - (1/2)a_{\mathrm{ZGNR}})$ This can be understood considering that for $\delta_\parallel = (1/2)a_{\mathrm{ZGNR}}$ we obtain the $\mathrm{A_{br}}$configuration and that shifts along the longitudinal direction around such configuration lead to equivalent stackings. The results of 4.12 (b)-(d) show that for the $\mathrm{A_{br}}$configuration, see Fig. 4.1 (f), both $\Delta^{(1)}$ and the spin splitting are maximized. Our results show that, due to the details of the electrostatic potential created by the atoms forming the heterostructure, the strongest sublattice-breaking effect of hBN is not obtained for the AA stacking configuration, as one would naively expect, but for configurations as the ones shown in Fig. 4.1 (f) and Fig. 4.11 (e), (f) in which the carbon atoms are slightly

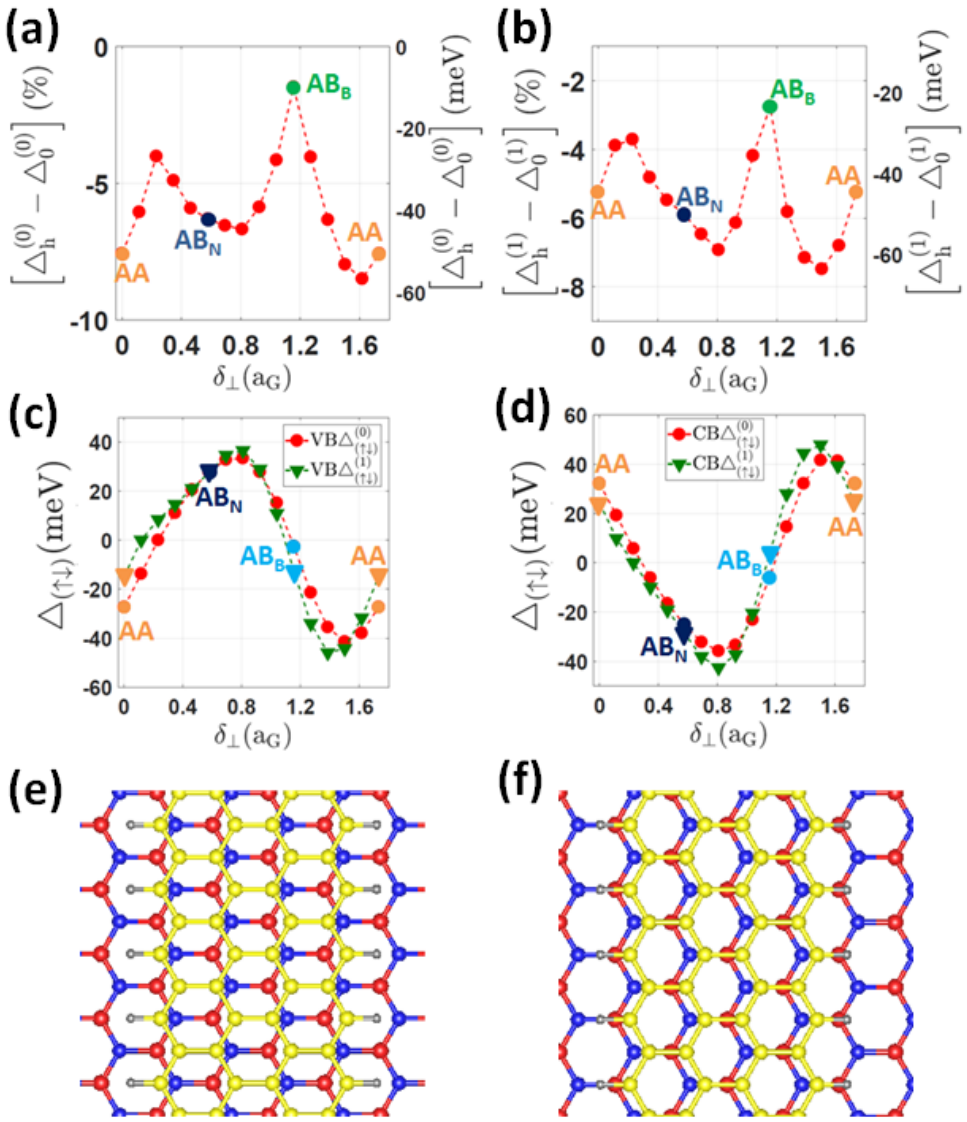

FIG. 4.11: Evolution of the band gaps and spin splittings of a ZGNR with $N = 4$ placed on hBN as a function of $\delta_\perp$. (a), (b), Change of $\Delta^{(0)}$, $\Delta^{(1)}$, respectively, due to the presence of the hBN. (c), (d) Spin splitting $\Delta_{(\uparrow\downarrow)}$, at $k = \pi/a_{\mathrm{ZGNR}}$, and close to $\Delta^{(0)}$, due to the presence of hBN for the VB and CB, respectively. (e), (f) Stacking configuration corresponding to the values of $\delta_\perp$ for which the spin splitting $\Delta_{(\uparrow\downarrow)}$ is maximized, shown in (c), (d): $\delta_\perp = 0.8a_G$ in (e), and $\delta_\perp = 1.5a_G$ in (f).

off from being directly above the nitrogen and carbon atoms.

Figure 4.14 shows the low-energy band structure of ZGNR-hBN for the A_{br}configuration. As to be expected we see, Figure 4.14 (c), that the spin splitting induced by the presence of hBN decreases as we move away from the $k = \pi/a_{\mathrm{ZGNR}}$ point, i.e as we move away from the value of k for which the locking of the spin and sublattice degree of freedoms for the edge states is the strongest.

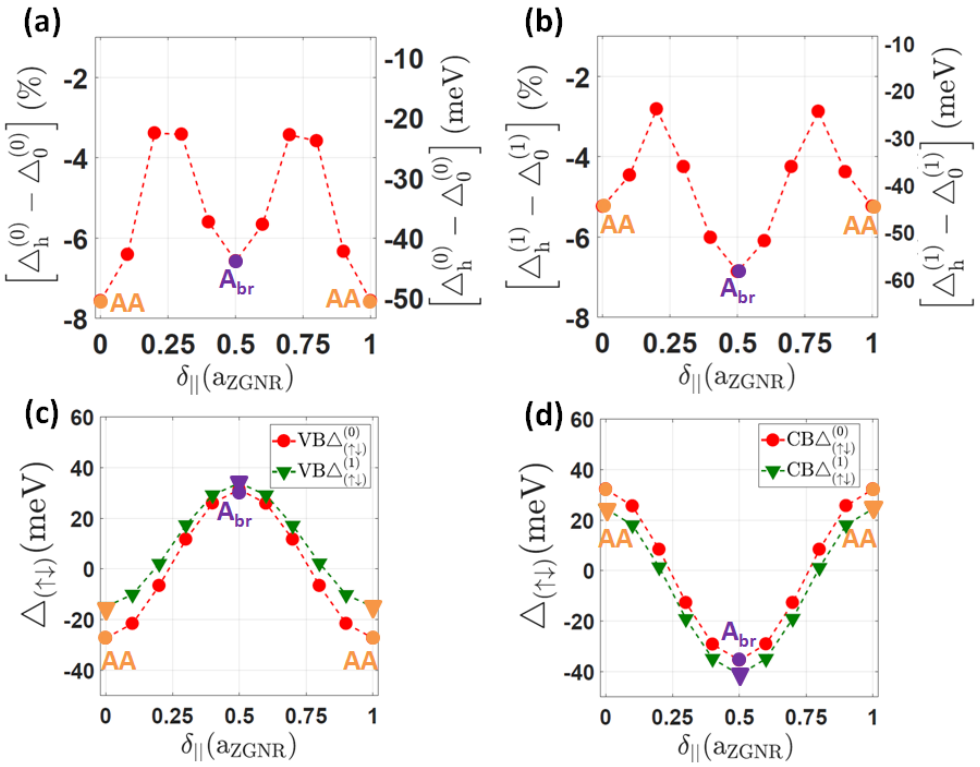

FIG. 4.12: Evolution of the band gaps and spin splittings of a ZGNR with $N = 4$ placed on hBN as a function of a shift $\delta_{||}$ away from AA stacking. (a) Change of $\Delta^{(0)}$ due to the presence of the hBN. (b) Change of $\Delta^{(1)}$ due to the presence of the hBN. (c), (d) Spin splitting $\Delta_{(\uparrow\downarrow)}$, at $k = \pi/a_{\mathrm{ZGNR}}$, and close to $\Delta^{(0)}$, due to the presence of hBN for the CB and VB respectively.

We have shown for the case of AGNRs that the more stable configuration is the AB_B one, Fig. 4.8. We expect this to be the case also for ZGNRs. This is confirmed by the results shown in Fig. 4.13 in which the the change, with respect to the AA-stacking

configuration, of the total energy of a ZGNR-hBN system (with $N = 4$) as a function of $\delta_{\parallel}$ and $\delta_{\perp}$ is shown.

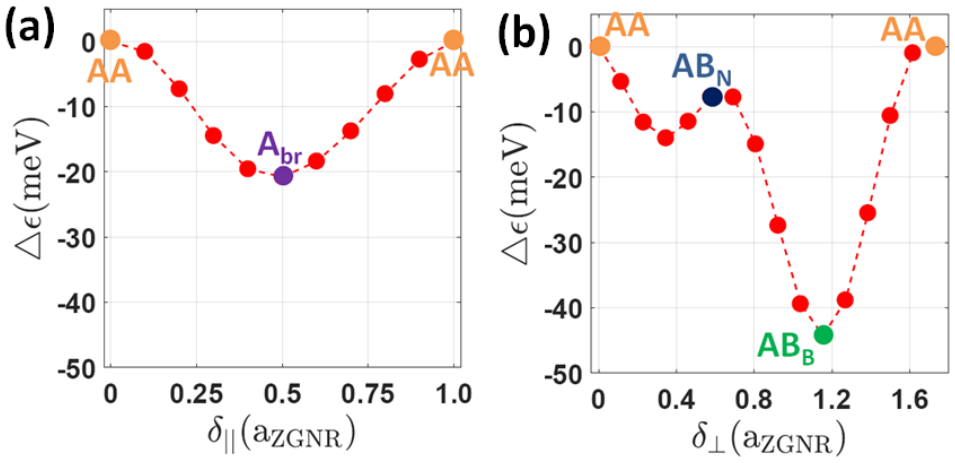

FIG. 4.13: (Color online) Change of the total energy, with respect to the case of AA stacking, as a function of $\delta_{\parallel}$ (a), and $\delta_{\perp}$ (b), for an ZGNR with $N = 4$ placed on hBN

The results of Figs. 4.11, 4.12 show that by shifting the ZGNR away from the AA configuration we have the maximum spin splitting for shift in the transverse direction with $\delta_{\perp} = 1.5a_G$. It is then interesting to see how the main features of the band structure of a ZGNR-hBN system with $\delta_{\perp} = 1.5a_G$ vary as we change the width of the nanoribbon. The results are shown in Fig. 4.15. For an isolated ZGNR we have that as N increases the band gap $\Delta^{(0)}$ induced by the antiferromagnetic ordering of the edge states decreases, whereas $\Delta^{(1)}$ remains approximately constant [51]. This is shown by the squares symbols in Fig. 4.15 (a), and (b), respectively. The circles in the same figures show the results for the ZGNR-hBN heterostructure. We see that the presence of hBN does not affect qualitatively the scaling of of $\Delta^{(0)}$ and $\Delta^{(1)}$ with respect to N.

It is then interesting to see how the spin splitting induced by the presence of hBN scales with N. Fig. 4.15 (c), (d) show the spin splitting around $\Delta^{(0)}$ and $\Delta^{(1)}$, respectively. Contrary to $\Delta^{(0)}$ the spin splitting around it depends very weakly on N. This can be

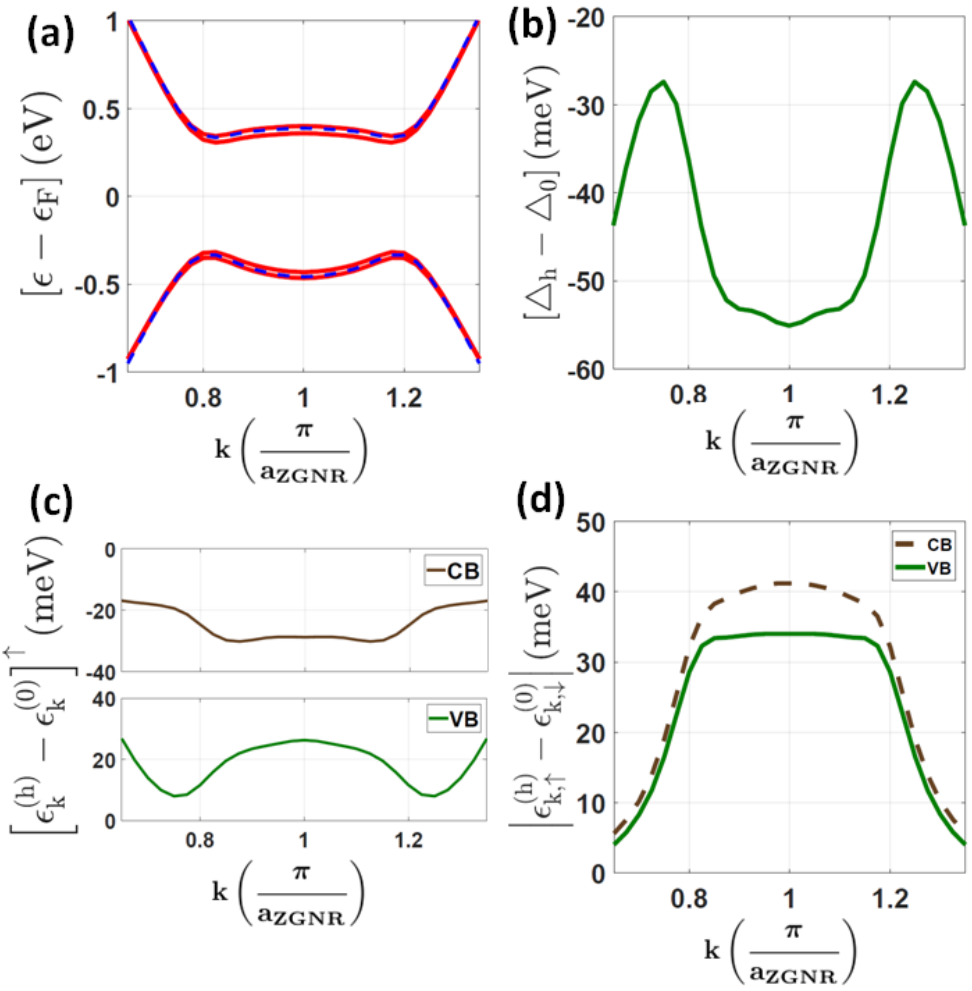

FIG. 4.14: Results for a ZGNR with ($N = 4$) placed on hBN in the A_{br} stacking configuration. (a) Band structure, the dashed lines show the bands for the isolated ZGNR. (b) Difference, for k close to π/a_{ZGNR}, between the band gap of the hBN-ZGNR heterostructure, Δ_h, and the band gap of the isolated ZGNR Δ_0. (c) The top panel shows the difference for k close to π/a_{ZGNR} between the ZGNR-hBN heterostructure's CB and the isolated ribbon's CB for the AA stacking configuration. The bottom panel show the difference between the VBs. (d) Spin splitting as a function of k for the ZGNR-hBN heterostructure's CB and VB.

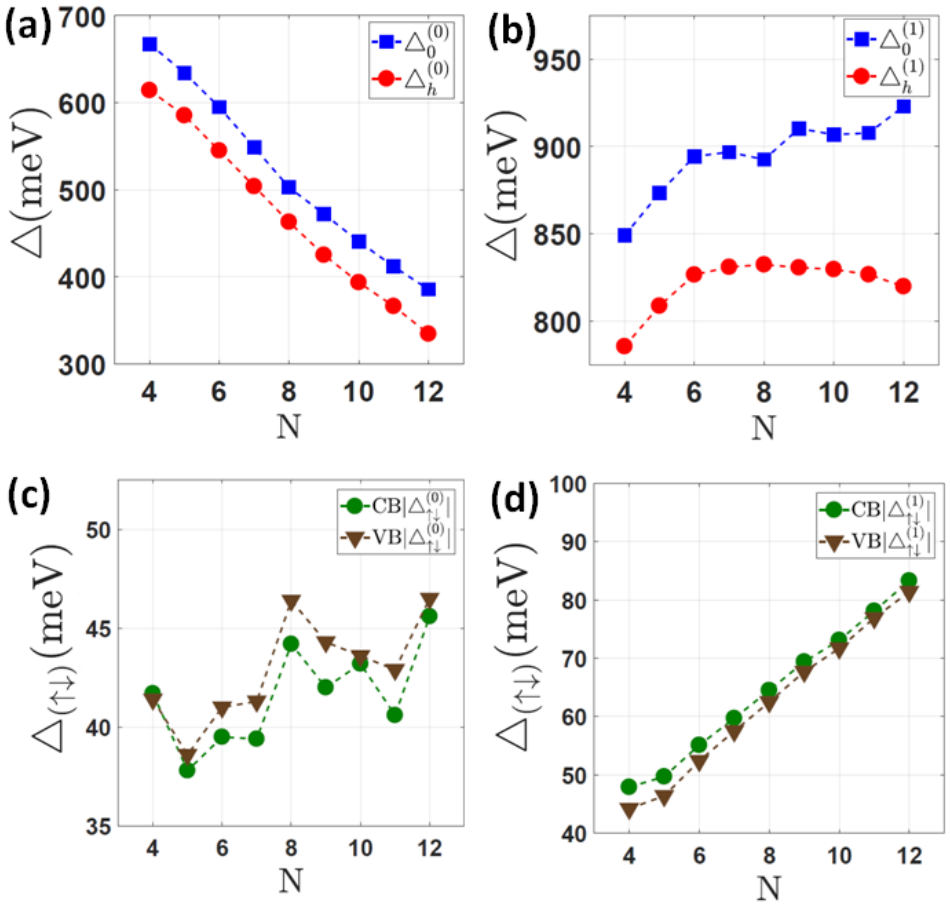

FIG. 4.15: Effect of the ribbon width, N for a ZGNR-hBN heterostructure with stacking configuration shown in Fig. 4.11 (f) corresponding to $\delta_\perp = 1.5a_G$, value of $\delta_\perp$ for which the spin splitting $\Delta_{(\uparrow\downarrow)}$ is maximized. $\Delta^{(0)}$, (a), and $\Delta^{(1)}$, (b), as a function of N for the ZGNR-hBN heterostructure and the isolated ribbon. $\Delta_{(\uparrow\downarrow)}$ for CB and VB around the X point, (c), and the $k = \pi/a_{\text{ZGNR}}$, (d).

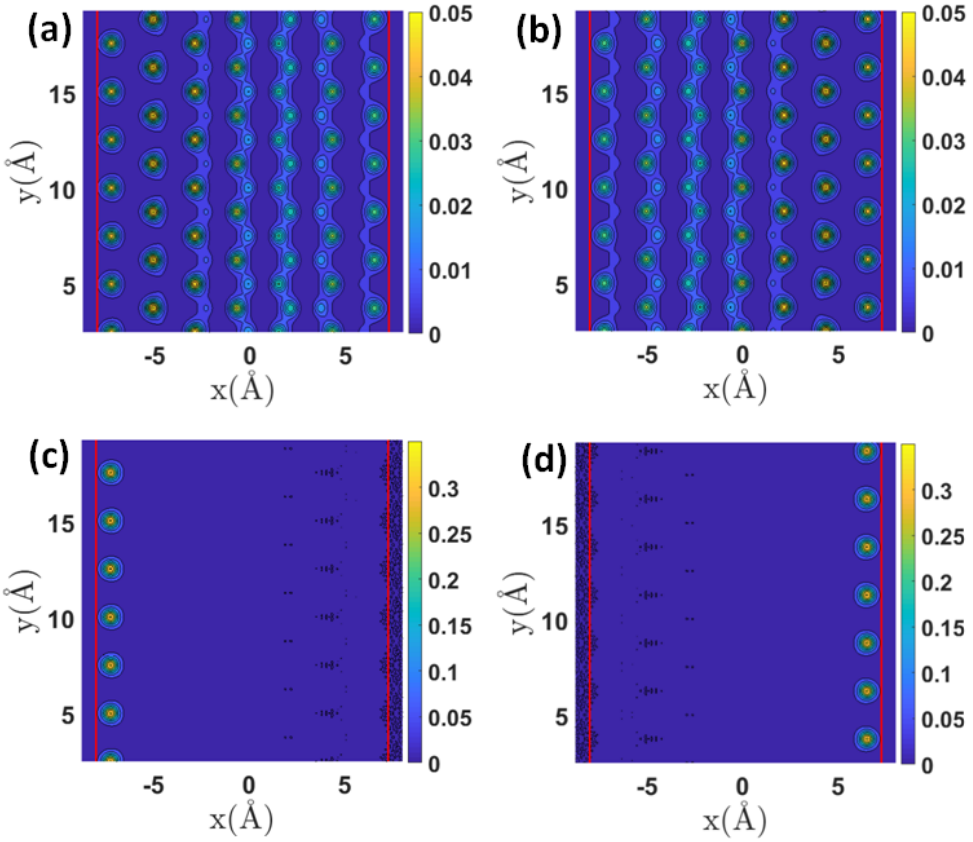

FIG. 4.16: Electron charge density for a pristine ZGNR with $N = 7$. (a), (b) ((c), (d)) show the electron density of spin up and spin down states, respectively close to $\Delta^{(0)}$ ($k = \pi/a_{\mathrm{ZGNR}}$).

qualitatively understood considering that the states close to $\Delta^{(0)}$ are not strongly localized at the edges as shown in Fig. 4.16 (c), (d) and their localization does not change much by varying the width of the ribbon. As a consequence, the fact that the carbon atoms at the opposite edges of the ribbons see a different electrostatic potential being either on top of nitrogen atoms or boron atoms, does not cause a spin splitting that depends strongly on the ZGNR's width, as shown in Fig. 4.15 (c). The opposite is true for the states close to $k = \pi/a_{\mathrm{ZGNR}}$: in this case the states are strongly localized to the edges and this localization increases with the ribbon's width enhancing the spin splitting due to the sublattice breaking effect of hBN on the ribbon, Fig. 4.15 (d). We therefore conclude that the semimetal character of ZGNRs placed on hBN can be increased by considering wider ribbons.

4.3 Conclusion

We have studied how the presence of hBN affects the electronic structure of armchair and zigzag graphene nanoribbons. We have determined how hBN modifies the low energy properties of the graphene ribbons' bands and how these changes depend on the stacking configuration. Pristine armchair graphene nanoribbons always have a finite band gap. We find that for the class of armchair graphene nanoribbons with the smallest band gap, ribbons of width $N = 3n - 1$ (with n a positive integer), the presence of hBN can modify the GNR's gap by as much as 20%. For the armchair graphene nanoribbons for which the band-width is larger when isolated, ribbons of width $N = 3n$ and $N = 3n + 1$, the presence of hBN modifies the size of the gap only up to about 6%.

The effect of hBN is much more significant for zigzag graphene nanoribbons. For these ribbons the band gap is due to the antiferromagnetic ordering of the edge states and the fact that the carbon atoms at the opposite edges of the ribbon belong to different

sublattices implies that the presence of hBN, by breaking the sublattice symmetry, can strongly modify the low-energy features of the ribbon. The presence of hBN can induce a significant spin splitting of the conduction and valence band and drive the ribbon into a half-metallic state. We find that such spin splitting is maximized for the so called *bridge* stacking configuration in which the carbon-carbon links of the GNR cross the boron-nitride links of hBN and for configurations close to the AA stacking configuration, but not for the AA stacking configuration itself. For a zigzag GNR of width $N = 4$ we find that the spin splitting of the conduction and valence bands can be maximized, by varying the stacking configuration, to about 40 meV conservatively assuming a GNR-hBN distance equal to 3.5Å.

Our results show that hBN in general modifies the low energy features of GNRs and that this effect can be tuned to some extent by varying the stacking configuration. For zigzag GNRs, due the spin-sublattice locking of the edges states, the presence of hBN induces a spin splitting of the conduction and valence bands that can be exploited, by properly doping the GNRs, to drive the ribbon into a half-metallic state. The ability to achieve a relatively large spin splitting of the conduction and valence bands without introducing external magnetic fields or proximity to ferromagnetic materials could be very helpful in spintronics applications and in particular to realize quasi 1D ideal spin-filters. In addition, by proximitizing the ribbon to a superconducting system with spin-orbit coupling, such as the surface of Pb, it should be possible to drive a ZGNR-hBN heterostructure into a quasi one-dimensional topological superconducting state.

CHAPTER 5

GNR-TMD

Transition metal dichalcogenides (TMDs) [57, 164, 165, 60, 166, 167, 36, 168] are a class of systems that in recent years has generated a lot of interest. Among the reasons for the high level of research activity on TMDs is the fact that such materials can be exfoliated to be only a few atoms thick [121, 169, 170] down to the limit of one monolayer, and the fact that they have strong spin orbit coupling. Moreover, recently some the TMDs, such as $NbSe_2$ [171, 36, 38, 172, 173], have been shown to be superconducting even when only one monolayer thick, and to have an in-plane upper critical field much larger than the Pauli paramagnetic limit [36, 38, 173] due to the presence of strong spin-orbit coupling. TMDs therefore possess two of the key ingredients –superconductivity and spin-orbit coupling – that can be exploited to engineer topological superconducting phases [174, 9, 175, 8]. These phases, in quasi one-dimensional (1D) systems, exhibit Majorana states bound to the two ends of the systems [7]. In turn, Majorana states can be exploited to realize topologically protected quantum bits, the building blocks of a topological quantum computer [8, 176]. These considerations make quasi 1D TMD-based systems a very interesting class of systems to study. Other possibility to realize quasi 1D TMD-based systems is to "cut" them into

ribbons [177, 178, 179, 180, 181, 182, 183, 184, 185, 186]. However, so far it appears to be challenging to realize high quality TMD ribbons.

In this work we consider a different route: we study the possibility to realize 1D systems with strong spin-orbit coupling (SOC) by combining graphene nanoribbons (GNRs) and 2D TMD systems. We find that in GNR-TMD heterostructures, via the proximity effect, the SOC in the GNR can be greatly enhanced leading to 1D systems ideal for spintronics applications and as basic elements to realize, when paired to a superconductor, Majoranas and topologically protected qubits.

We obtain, via ab-initio calculation, the band structure of armchair GNRs (AGNRs) and zigzag GNRs (ZGNRs) when placed on semiconductor and metallic TMD. To exemplify the physics for the case in which the TMD is a semiconductor we consider TMD: $MoSe_2$. Molybdenum- based TMDs are among the most studied semiconductor TMDs. Mo is the lightest transition metal forming semiconductor TMDs a fact that helps to reduce the resources needed to carry out the calculations that are computationally very expensive due to the large primitive cell required because of the large mismatch between GNRs' and TMD's lattice constants.

For the metallic case, we consider $NbSe_2$ which is particularly interesting given that it becomes superconducting at low temperatures with a so-called Ising-pairing [36, 38] that allows it to remain superconducting for values of in-plane magnetic fields well beyond the Pauli paramagnetic limit. By comparing the ab-initio results to tight-binding model results we estimated that the tunneling strength between AGNRs and $NbSe_2$ is approximately 20 meV, a value that should guarantee that for temperatures lower than the $NbSe_2$ critical temperature T_c a significant superconducting pairing should be induced into the GNRs via the proximity effect.

This chapter is organized as follows: in Sec.5.1 we provide the geometrical characterization of GNR-TMD heterostructures and the details of the method used to obtain the

electronic structure, in Sec.5.2 we first show the results for the case of GNRs on semiconductor TMDs and then for the case of GNR-$NbSe_2$ heterostructures.

5.1 Method

We consider heterostructures formed by AGNRs or ZGNR placed on a monolayer of a TMD [27, 23, 165, 62, 20, 12]. TMD monolayers have an in-plane hexagonal structures as shown in Fig. 5.1 (a). Such a honeycomb lattice is best describe as formed by two triangular sublattices: one sublattice is formed by the transition metal atoms, the darker and larger spheres in Fig. 5.1 (a) and the other by pairs of chalcogenide atoms, the lighter and smaller spheres in Fig. 5.1 (a). As the bottom of Fig. 5.1 (a) shows the pair of chalcogenide atoms are placed on two different planes, one below and one above the plane formed by the transition metal atoms. We denote by u the distance between the chalcogenide plane and the transition metal plane, and by a_s the in-plane lattice constant. The lattice of the TMD substrate is characterized by two primitive vectors $\mathbf{a}_1^s = a_s[\cos(\pi/6)\hat{x} - \sin(\pi/6)\hat{y}]$, and $\mathbf{a}_2^s = a_s[\cos(\pi/6)\hat{x} + \sin(\pi/6)\hat{y}]$, as shown in Fig. 5.1. For $MoSe_2$ we use $a_s = 3.33$Å and $u = 1.674$Å, for $NbSe_2$ we use $a_s = 3.48$Å and $u = 1.679$Å, values that are consistent with experimental values [19] and the ones obtained via ab-initio relaxation calculations [62, 165]

All the electronic structure are obtained via ab-initio density functional theory (DFT) calculations using the Quantum Espresso package [81]. We use the Perdew-Burke-Ernzerhof functional [24] to model the exchange-correlation term, and ultrasoft pseudopotential with a minimum kinetic energy cutoff for the charge density and the potential of 400 Ry. The minimum kinetic energy cutoff for planewave expansion was set to 50 Ry. The integration of the total energy was performed within the first Brillouin zone on the uniform k-points Monkhorst-Pack mesh [187] with sizes $(10 \times 1 \times 1)$ for AGNR-$MoSe_2$, $(16 \times 1 \times 1)$ for AGNR-$NbSe_2$, $(20 \times 1 \times 1)$ for ZGNR-$MoSe_2$, and $(10 \times 2 \times 1)$ for ZGNR-$NbSe_2$ to verify

the convergence of the results.

For each structure, the energy bandstructure was obtained with and without relativistic corrections to identify the effect of spin orbit coupling on the electronic structure of the GNR-TMD system.

To keep the presentation self-contained in Fig. 5.1 we show the band structure for the TMD's monolayers that we consider in the remainder as substrates for GNRs: MoS_2 in Fig. 5.1 (b), $MoSe_2$ in Fig. 5.1 (c) and $NbSe_2$ in Fig. 5.1 (d). $MoSe_2$ has a direct band gap equal to 1.33 eV whereas $NbSe_2$ is metallic. The key feature of TMDs monolayers is the presence of a strong spin-orbit-induced spin splitting around the K-point of the Brillouin Zone (BZ). For a monolayer TMD the strength of the SOC can be quantified by the spin splitting at the K point of conduction or valence band, whichever is largest. For $MoSe_2$ the conduction band has a spin splitting equal to 188.8 meV, for the $NbSe_2$ the conduction band has the largest spin splitting, equal to 156 meV, at the K point. Table 5.1 summarizes the key properties of the TMDs that we consider

System	a_S(Å)	u(Å)	Note	Gap(eV)	$\triangle^v_{\uparrow\downarrow}$(meV)	$\triangle^c_{\uparrow\downarrow}$(meV)
$MoSe_2$	3.33	1.674	PBE	1.33	189	21
$NbSe_2$	3.48	1.679	PBE	-	155	-

TABLE 5.1: Table shows the structural parameter values of the TMD substrates used in this work. Lattice constant of single layer TMD is given by (a_S). The closest distance between transition atom plane and dichalcogenide atom plane is denoted by u. $\triangle^{v/c}_{\uparrow\downarrow}$ are the maximum spin splitting energy at valley K for valence and conduction band.

Graphene nanoribbons are of two types depending on the type of edges: armchair nanoribbons shown in Fig. 5.2 (a), and zigzag ribbons shown in Fig. 5.2 (b). In these figures we also show the corresponding lattice constants $a_{\text{AGNR}} = \sqrt{3}a_G$, $a_{\text{ZGNR}} = a_G$, for an AGNR and a ZGNR, respectively, where $a_G = 2.46$Å is the graphene lattice constant. Fig 5.2 (c) and (d) show the typical electronic structure obtained via ab-initio calculations for an AGNR and a ZGNR respectively. In all our calculations, to avoid the effect of dangling bonds, we terminate the edges of the GNRs with hydrogen atoms, shown as

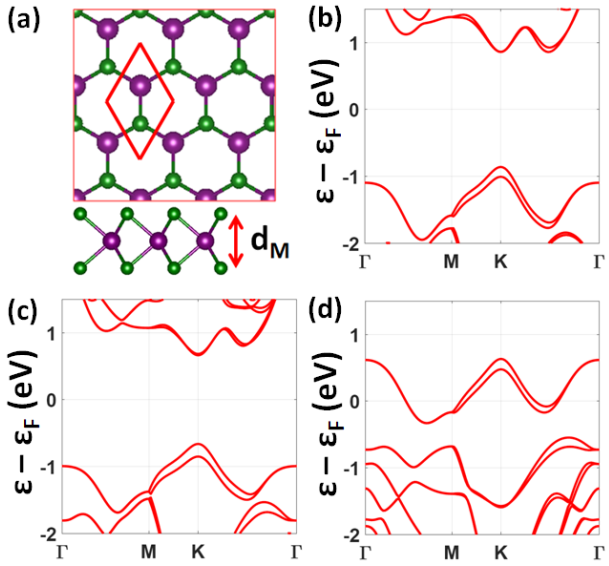

FIG. 5.1: (Color online). (a) Typical structure of a TMD monolayer. Band structure of MoS_2, (b), $MoSe_2$ (c), and $NbSe_2$ (d).

small grey sphere in Fig. 5.2. The band structure of both types of GNRs has a direct gap. In ZGNRs the gap at $k = \pi$ is due to electron-electron interactions that favor a ground state in which the electrons are ferromagnetically polarized along the edges and antiferromagnetically between the edges [158, 51, 188, 46, 94, 98, 189].. AGNRs can be classified in three distinct groups depending on their chirality [47]. Let N be the width, in terms of carbon-carbon dimers aligned along the longitudinal direction, of an AGNR. The three ANGRs' chirality classes correspond to ribbons with width $N = 3n - 1$, $N = 3n$, $N = 3n + 1$ $n \in \mathbb{N}$. DFT results [51, 92, 155] show that, contrary to the prediction of simple tight-binding models with constant hopping between the p_z orbitals, all three types of AGNRs have a direct band gap at $k = 0$, but this gap is much smaller for the class with $N = 3n - 1$. For this in the remainder for AGNR-TMD heterostructures we focus on the case when $N = 3n - 1 = 5$.

The GNR-TMD heterostructure is characterized by a one dimensional primitive cell

that depend on the stacking orientation of the GNR with respect to the TMD. Let θ be the relative angle between the substrate and the ribbon. The condition for a commensurate structure can be expressed as:

$$ma_r e^{i\theta} = a_s[pe^{i\pi/6} + qe^{-i\pi/6}] \tag{5.1}$$

where a_r is the ribbon lattice constant, a_s is the TMD lattice constant and (m, p, q) are positive integers. Equation (5.1) implies that the integers (m, p, q) mus satisfy the following equation:

$$a_r^2 m^2 = a_s^2(p^2 + q^2 + pq). \tag{5.2}$$

We use equations (5.1), (5.2) to identify possible commensurate structures with the constrains that the uniform strain on GNR be less than 5%. The primitive vector $\mathbf{a}_h$ of the GNR-TMD heterostructure is then given by $\mathbf{a}_h = ma_r[\cos\theta x + \sin\theta y]$

Figure 5.3 shows schematically the orientation in momentum space of the GNR's and TMD's Brillouin zones for a generic relative θ. The 2D BZ of the TMD is folded to the 1D BZ of the heterostructure. We can see that for same values of θ, for example $\theta = 0$ the opposite valleys K and K' of the TMD BZ fold on the same point of the heterostructure reduced BZ, its Γ point. For other values of θ, for example $\theta = \pi/2$, equivalent valleys K (and K') fold on the same point of the heterostructure reduced BZ, Fig. 5.3. Considering that the spin splitting at the valley K and K' are equal and opposite, due to time reversal symmetry, we can expect the effect of spin-orbit coupling on the electronic structure of the GNR-TMD system will be much smaller that for configurations in which K and K' fold to the same point of the reduced BZ (such as when $\theta = 0$) than for configurations in which equivalent valley fold to the same point of the reduced BZ (such as when $\theta = \pi/2$). For this reason, in the remainder we consider these two extreme cases: $\theta = 0$, and $\theta = \pi/2$.

The distance d between the GNR and the TMD was set to be equal to the one between graphene and the TMD. Using relaxation calculations with fixed in plan structure we obtained $d = 3.54$Å and $d = 3.49$Å for $MoSe_2$ and $NbSe_2$, respectively, values that are consistent with previous results [6]. The full list structural parameters of the structures that we considered are shown in Table. 5.2.

System	Structure (m_p, m, n)	θ	$a_{TMD}(\AA)$	Strain GNR (%)	$a(\AA)$
AGNR-$MoSe_2$	(4,3,3)	0^0	3.33	1.5	17.3
AGNR-$MoSe_2$	(3,-4,4)	90^0	3.33	4.2	13.3
AGNR-$NbSe_2$	(3,2,2)	0^0	3.48	-5.7	12.1
AGNR-$NbSe_2$	(3,-4,4)	90^0	3.48	8.9	13.9
ZGNR-$MoSe_2$	(7,-3,-3)	0^0	3.33	0.5	17.3
ZGNR-$MoSe_2$	(4,-3,3)	90^0	3.33	1.5	9.99
ZGNR-$NbSe_2$	(5,-2,-2)	0^0	3.48	-2	12.05
ZGNR-$NbSe_2$	(3,-2,2)	90^0	3.48	-5.7	6.96

TABLE 5.2: The structural parameters of the selected heterostructures are given in this table.

To be able to set up a DFT calculation the one-dimensional GNR-TMD heterostructure is simulated as a three-dimensional periodic system as illustrated in Fig.5.2 (a) shown schematically in Fig. 5.2 (b) in which an array of parallel GNRs is placed on the TMD. The distance $D = |\boldsymbol{A_2}| - L_r$ is chosen large enough to minimize interference effects between parallel ribbons where L_r equal to the ribbon width. We chose $D = 11.5$Å for AGNR-TMD and $D = 17.5$Å for ZGNR-TMD system. Each plane is periodically replicated in the direction perpendicular to the plane with a vacuum interspace 15Å thick.

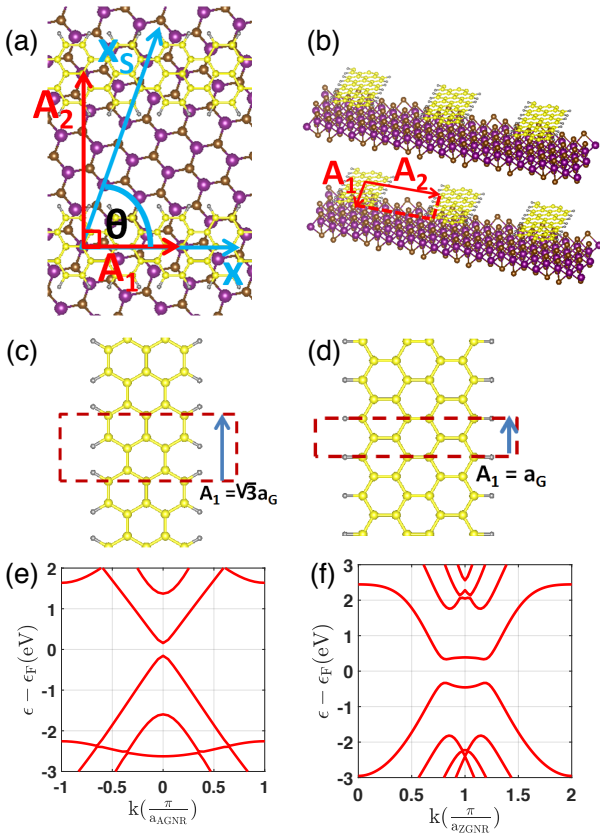

FIG. 5.2: Schematic of the GNR-TMD heterostructure. (a) x is the direction along the longitudinal direction of the ribbon and x_s is the $x-$axis for the substrate. $\boldsymbol{A_1}$ and $\boldsymbol{A_2}$ are the primitive vectors of the supercell translation. (b) Three-dimensional periodic cell used in the DFT calculation. (c) Example of armchair GNR with corresponding primitive lattice vector. (d) Example of zigzag GNR with corresponding primitive lattice vector. (e) Low energy band structure of isolated AGNR shown in (c). (f) Low energy band structure of isolated AGNR shown in (d).

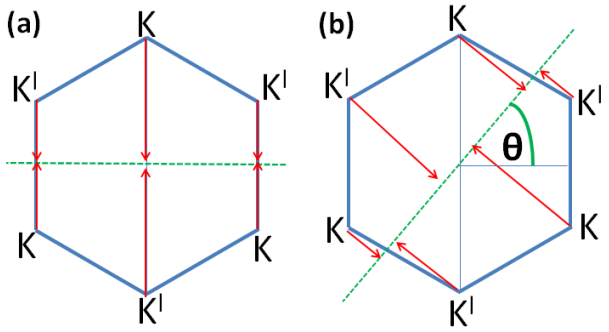

FIG. 5.3: The figures show the orientation of ribbon given by green dash line relative to the first BZ of monolayer TMD given by blue hexagon. The one-dimensional periodicity of the combined sytem will be parallel to the ribbon. TMD valleys will be folded to different position on the 1D periodic axis shown by the red arrows. (a) and (b) correspond to $\theta = 0^0$ and arbitrary rotation angle θ, respectively. We see that valley K and K' overlap at the same k point in particular configuration like (a). In general, the folding will depends on the rotation angle between GNR and TMD.

5.2 Results

5.2.1 Graphene nanoribbons on semiconductor TMD

AGNR on semiconductor TMD

In this section, we present the bandstructure of AGNR on $MoSe_2$ for rotation angle $\theta = 0^0$ and $\theta = 90^0$. The crystal structures are shown in Fig.5.4 where we have two and three primitive cells of AGNR within the supercell for rotation angle $\theta = 0^0$ and $\theta = 90^0$. In order to form one-dimensional periodic system, we uniformly stretched the ribbon with the strain value 1.5% for $\theta = 0^0$ and 4.2% for $\theta = 90^0$. The magnitude of translation vector $\boldsymbol{A_1}$ are 17.3Å and 13.3Å.

The AGNR-$MoSe_2$ bandstructure for $\theta = 0^0$ is shown in Fig.5.5(a). The AGNR parabolic energy band is positioned closer to the conduction band of $MoSe_2$. The maximum energy of AGNR valence band is 0.76 eV above the valence band of $MoSe_2$, meanwhile, the lowest ribbon conduction band is about 0.25 eV below the conduction band of $MoSe_2$. The

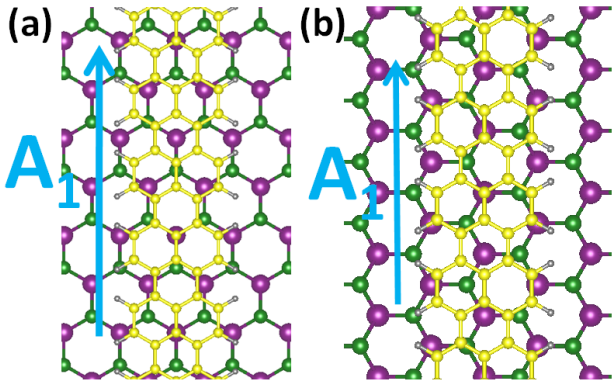

FIG. 5.4: The crystal structure of AGNR on $MoSe_2$ are depicted on (a) and (b) where the rotation angle are set to $\theta = 0^0$ and $\theta = 90^0$, respectively.

band gap is changed by -4.13% relative to the pristine AGNR bandgap energy about 322 meV. We observe similar result for $\theta = 90^0$. The gap is changed about -4.92% relative to the pristine ribbon band gap about 283 meV. The maximum AGNR valence band state is 0.64 eV above the highest valence band state of $MoSe_2$. The AGNR conduction band is 0.42 eV below $MoSe_2$ conduction band. We also observe the electron effective mass change is negligible for both angle showing the electronic mobility of these bands retained in the heterostructure.

Valley K and K' of $MoSe_2$ will be folded to the same k point in the k space shown in Fig.5.3(a) when $\theta = 0$. Due to this overlap, the valence and conduction band of $MoSe_2$ will become spin degenerate with the center at k = 0. On the contrary, when the rotation angle is set to 90^0, the center of each valley will be folded to other similar type of valley preserving the valley structure. Because of this, the spin splitting still exists on the valence and conduction band of $MoSe_2$.

The spin splitting on TMD bands can be important when the energy of AGNR bands is close to the TMD valence or conduction bands as the hybridization is likely to happen when the energy of two states not too different. In this case, the spin splitting in TMD layer

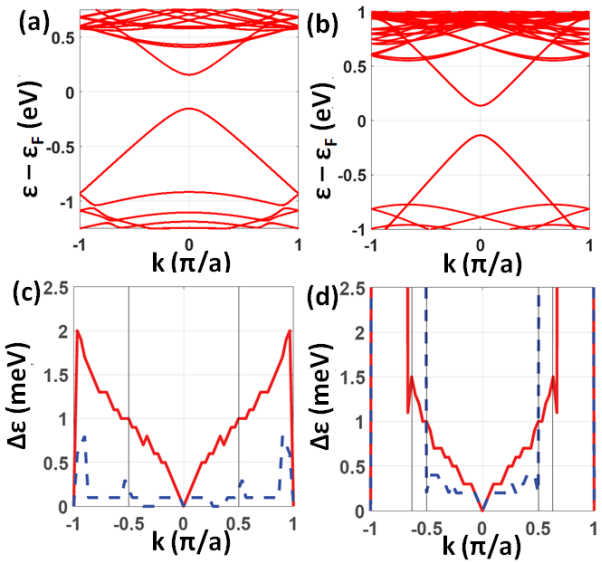

FIG. 5.5: Figure (a) and (b) show the AGNR-$MoSe_2$ bandstructure for $\theta = 0^0$ and $\theta = 90^0$. The spin splitting energy on the ribbon bands are depicted in (c) and (d) corresponding to $\theta = 0^0$ and $\theta = 90^0$. The red(solid) and blue(dash) are the splitting energy for valence and conduction band.

can be transferred to ribbon states due to the spin selective hybridization. The parabolic band of ribbon in AGNR-$MoSe_2$ system has energy much higher than the valence bands of $MoSe_2$, so this effect is greatly suppressed.

We still observe that the spin degeneracy on AGNR low energy bands is removed with the spin splitting energy given in Fig.5.5(c-d) as function of momentum. There is no spin splitting at $k = 0$ due to time reversal symmetry. We also have zero spin splitting at the boundary of Brillouin zone $k = \pm\frac{\pi}{a}$ caused by the translation invariant symmetry and time reversal symmetry. The spin splitting energy on the valence band is increasing from 0 at $k = 0$ to 1 meV at $k = \frac{|0.5|\pi}{a}$ for both angles.

The spin splitting on AGNR bands is caused by the Rashba SOC induced on ribbon. The broken inversion symmetry along z axis will produce the electric field orthogonal to the ribbon plane. Rashba SOC is proportional to $\left[\vec{p} \times \vec{E}\right] \bullet \vec{\sigma}$ with $\vec{p}$, $\vec{E}$, and $\vec{\sigma}$ denoting for electron momentum on the ribbon, electric field on z direction, and the electron spin

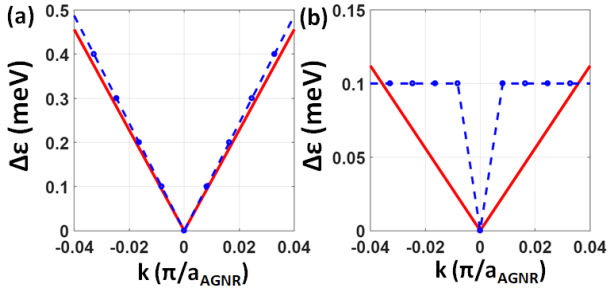

FIG. 5.6: Figure (a) and (b) show the spin splitting energy close to k = 0 for valence and conduction band, respectively, with $\theta = 0^0$. The red (solid) line is the fitting curve to DFT result shown by blue (dash) line.

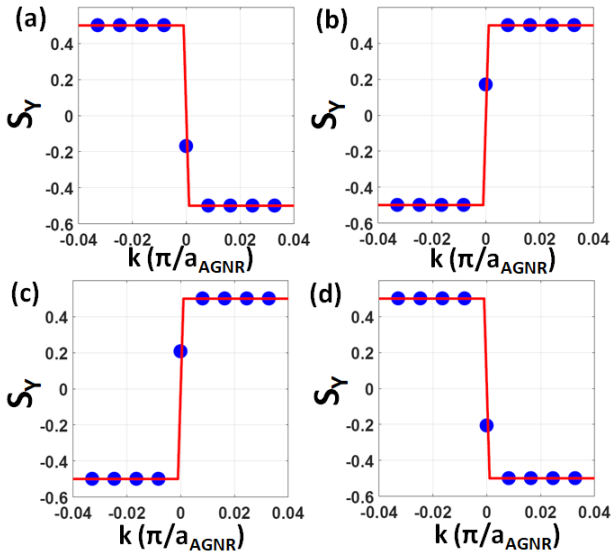

FIG. 5.7: The spin projection from DFT calculation is shown on (a-b) and (c-d) corresponding to two highest valence band and two lowest conduction bands of AGNR-$MoSe_2$ with $\theta = 0^0$.

operator. Hence, we introduced the effective SOC Hamiltonian to describe the electronic structure of AGNR on TMD substrate below:

$$V_{\mathrm{SOC}}^{\mathrm{v/c}} = \alpha_x k\sigma_x + \alpha_y k\sigma_y + \alpha_z k\sigma_z \tag{5.3}$$

σ and k is the Pauli matrix in the spin space and the Bloch momentum of the wave-function. α_i is the coefficient that depend on the system configuration. We distinguished the SOC potential for conduction and valence band because DFT calculation shows that the spin structure and energy splitting are different for these bands. In the lowest order, we approximate the SOC potential as linear function of k restricting the accuracy of this model between $-0.04\frac{\pi}{a_{\mathrm{AGNR}}} \leq k \leq 0.04\frac{\pi}{a_{\mathrm{AGNR}}}$ suggested by the linearity of energy splitting within this range. The energy splitting on a particular band is a linear function of k that can be formulated below:

$$\triangle E = 2\mathrm{g}_{\mathrm{soc}}^{\mathrm{v/c}}|k| \tag{5.4}$$

The slope $\mathrm{g}_{\mathrm{soc}}^{\mathrm{v/c}}$ can also be used to compare the strength of induced SOC on each configurations as it depends on the magnitude of α_i.

$$\mathrm{g}_{\mathrm{soc}} = 2\sqrt{\alpha_x^2 + \alpha_y^2 + \alpha_z^2} \tag{5.5}$$

We performed a curve fitting to the energy splitting of AGNR bands and its spin structure calculated using DFT to determine the coefficients α_x, α_y, and α_z. Therefore, the total effective Hamiltonian are constituted by the kinetic term and effective SOC potential.

$$H = \epsilon_0^{\mathrm{v/c}}\sigma_0 + V_{\mathrm{SOC}}^{\mathrm{v/c}} \tag{5.6}$$

The kinetic energy term $\epsilon_0^{\mathrm{v/c}}$ has an usual parabolic dispersion derived from k.p theory[190]:

$$\epsilon_0^{\mathrm{v/c}}(k) = \pm\left(\frac{E_g}{2} + \frac{\hbar^2 k^2}{2m_{\mathrm{v/c}}}\right) \tag{5.7}$$

where E_g, $m_{\mathrm{v/c}}$, and k are the band gap, effective mass, and momentum of electron. The parameters were calculated by fitting to the DFT result with the values listed in Table 5.3.

Structure $N = 5$		$\theta = 0^0$		$\theta = 90^0$	
		AGNR	AGNR-$MoSe_2$	AGNR	AGNR-$MoSe_2$
Gap(meV)		322	309	283	269
Mass (m_e)	V2	0.007	0.007	0.006	0.006
	V1	0.007	0.007	0.006	0.006
	C1	0.007	0.007	0.006	0.006
	C2	0.007	0.007	0.006	0.006
SOC Valence (meVÅ)	α_x	-	0	-	0
	α_y	-	7.73	-	5.42
	α_z	-	0	-	-1.22
	g^v_{soc}	-	7.73	-	5.56
SOC Conduction (meVÅ)	α_x	-	0	-	0
	α_y	-	-1.90	-	3.39
	α_z	-	0	-	2.31
	g^c_{soc}	-	1.90	-	4.10

TABLE 5.3: The calculated effective mass and SOC parameters for AGNR-$MoSe_2$ are presented.

The finite magnitude of α_y and α_z demonstrates that the electron spin will be aligned to y or z axis as what we also observe from DFT calculation given in Fig.5.7. We also notice that the induced SOC strength g_{soc} is slightly larger in AGNR valence band. In $MoSe_2$, its valence band has much stronger SOC potential compared to its conduction band. The ribbon valence band has energy closer to the valence band of $MoSe_2$. However, the ribbon conduction band has energy closer to the conduction band of $MoSe_2$. This is probably the reason that the induced SOC in AGNR valence band is more than the conduction band.

ZGNR on semiconductor TMD

ZGNR has a FA (Ferro-Antiferromagnetic) ground states with the spin ordering localized at both edges. Each edge has ferromagnetic spin ordering with antiferromagnetic coupling between opposite edges. In this section, we studied the electronic properties of ZGNR-TMD heterostructure for narrow ribbon with the ribbon width $N = 4$. We used a single layer $MoSe_2$ as the two-dimensional semiconductor substrate for the ribbon. The stacking configuration number was selected to be $(m_p = 7, m = -3, n = 3)$ and $(m_p = -4, m = -3, n = 3)$ giving the rotation angle to be $\theta = 0^0$ and $\theta = 90^0$. The ribbon is also uniformly stretched with the strain value about 0.5% for $\theta = 0^0$ and 1.5% for $\theta = 90^0$ to realize the structure commensurability with the smallest supercell size. The heterostructure configurations are depicted in Fig.5.8.

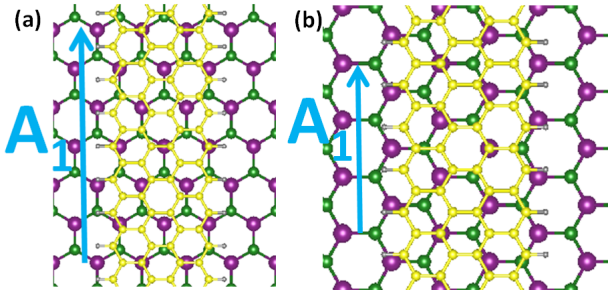

FIG. 5.8: Structure of ZGNR-$MoSe_2$ are depicted in (a) for rotation angle $\theta = 0^0$ and (b) for $\theta = 90^0$.

The magnitude of translation vector $\boldsymbol{A_1}$ for structure with $\theta = 0^0$ and $\theta = 90^0$ are $7a_{\text{ZGNR}}$ and $4a_{\text{ZGNR}}$, respectively. Because the reciprocal lattice vector is inversely proportional to magnitude $\boldsymbol{A_1}$, the edge states of pristine ZGNR with momentum $k = \pm\frac{\pi}{a_{\text{ZGNR}}}$ are folded to the $k = \pm\frac{\pi}{a}$ for $\theta = 0^0$ and $k = 0$ for $\theta = 90^0$ with $a = |\boldsymbol{A_1}|$ is the supercell lattice constant. Figure 5.9(a-b) and (c-d) show the bandstructures without and with SOC interaction, respectively. The semiconducting electronic properties of ZGNR are

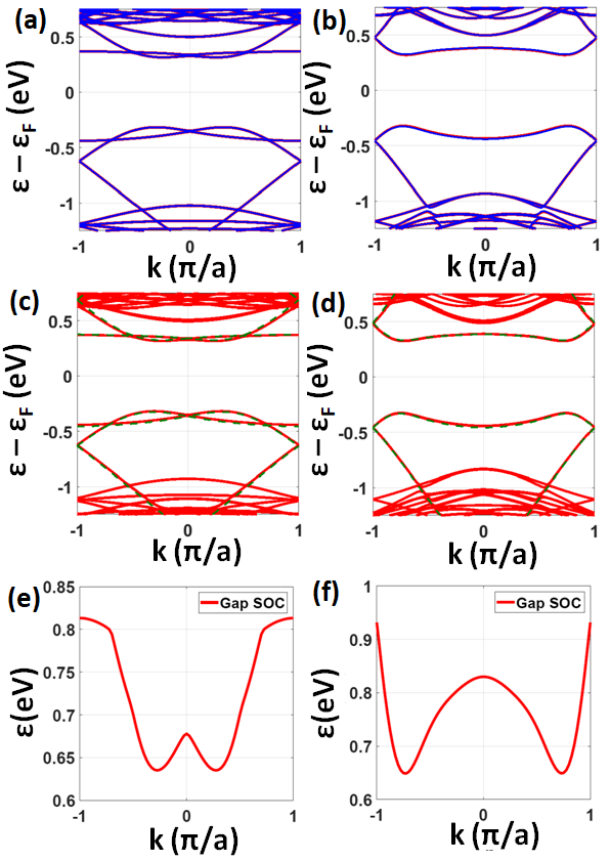

FIG. 5.9: Left and right panel are the calculated electronic properties for ZGNR-$MoSe_2$ with $\theta = 0^0$ and $\theta = 90^0$, respectively. The bandstructure of ZGNR-$MoSe_2$ calculated with non-relativistic pseudopotential (no SOC) are given in (a) and (b). The fully-relativistic pseudopotential including SOC interaction were used to calculate the bandstructure in (c) and (d). The energy difference between the conduction and valence band as function of momentum are given in (e-f).

still retained in the presence of $MoSe_2$ substrate. The low energy of the system is formed by ribbon low energy bands. The position of the highest ribbon valence band is 0.5 eV for $\theta = 0^0$ and 0.6 eV for $\theta = 90^0$ above $MoSe_2$ valence band. Meanwhile, the lowest ribbon conduction band is 0.18 eV and 0.16 eV below the $MoSe_2$ conduction band. The band gap energy for $\theta = 0^0$ is altered by -1.83% relative to the pristine gap 0.660 eV. For $\theta = 90^0$, the band gap is change by -2.11% relative to its pristine band gap energy about 0.648 eV. Note that the ribbon strain are different between these two angles.

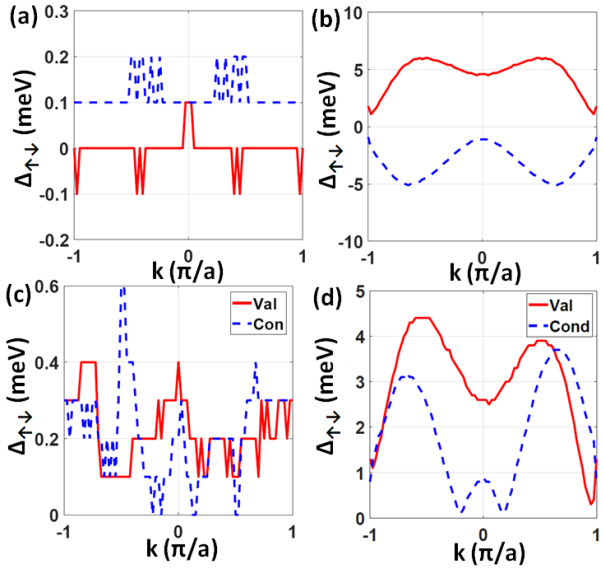

FIG. 5.10: The spin splitting energy of ZGNR-$MoSe_2$ structure calculated without and with SOC interaction are given on the top and bottom panel, respectively. Figure (a,c) is the splitting when $\theta = 0^0$. Figure (b,d) is the splitting when $\theta = 90^0$. Solid and dash lines are corresponding to valence and conduction band.

We observe the spin degeneracy is already removed even when non-relativistic pseudopotential without including SOC interaction is used to calculate the electronic structure of the system. We plot the corresponding spin splitting energy on ZGNR bands as function of momentum in Figure 5.10 with (a) for $\theta = 0^0$ and (b) for $\theta = 90^0$. We see that the energy splitting for structure with $\theta = 0$ is small and negligible. On the other hand, we see a finite spin splitting energy up to 5 meV for the structure with $\theta = 90^0$.

We can explain the mechanism of the spin splitting on ZGNR bands by considering the crystal structure in Fig. 5.8. The sublattice symmetry for the carbon atoms at the edges is broken as their local atomic configurations are different between the opposite edges. When $\theta = 0^0$, there is not much contrast in the local configuration of C atoms that sits on the left or right edges of ribbon. They are positioned alternately closer to Mo or Se atoms at each edge. Compare this with the configuration when $\theta = 90^0$ where there is a significant difference of the local configurations between right and left edge of ribbon. We see that the C atoms at the left edge are mostly closer to Mo atoms. Meanwhile, some of C atoms at the right edge are positioned close to Se atoms. This local configuration difference introduces different staggered potential between two edges, thus, the spin degeneracy could be lifted by this broken sublattice symmetry. As a consequence, we see that the energy splitting for structure with $\theta = 0$ is negligible. On the other hand, we see a finite spin splitting up to 5 meV for the structure with $\theta = 90^0$. There is another indication for this mechanism to be responsible for the spin splitting. The spin splitting energy for the conduction band has opposite sign from the valence band. This means the spin ordering is opposite between valence and conduction bands. We also see this effect on ZGNR-hBN system giving larger spin splitting up to 40 meV [191].

When we introduce SOC interaction in the calculation, the spin splitting energy is slightly changed for $\theta = 90^0$ depicted in Fig. 5.10(d). We observe the splitting energy is not symmetric relative to k = 0. The splitting energy is higher/lower when $k < 0$ compared to $k > 0$ for valence/conduction band. The possible reason is the additional Rashba SOC with the expression proportional to $\alpha_z \sigma_z k$ arisen from induced electric field on y axis. However, we see that the effect of this Rashba SOC in order less than 1 meV is smaller compared to the staggered sublattice potential between two edges in order about 5 meV.

5.2.2 Graphene nanoribbons on metallic TMD

In this section we consider the case when the substrate is a monolayer of $NbSe_2$, that is metallic at room temperature. The Fermi surface of $NbSe_2$ is characterized by two pockets, one around the Γ point of the BZ and one around the K and K' points, as shown in Fig. 5.11. The spin orbit coupling around Γ pocket is smaller that around pocket K or K'.

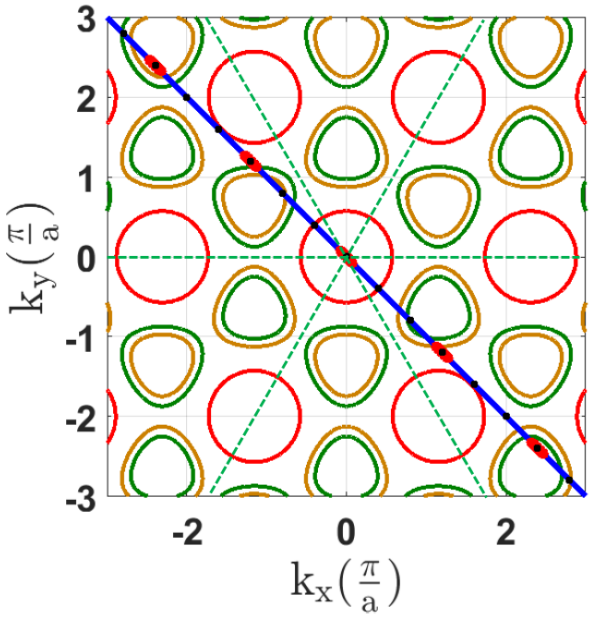

FIG. 5.11: Fermi surface of $NbSe_2$ which consist of several pockets around Γ shown by red circle, K and K' shown by triangular shapes. We neglect the spin splitting at pocket Γ. There is spin splitting at pocket K and K' with spin up and down represented by brown and green colors. The orientation of GNR is parallel to the blue line which is also the direction of 1D periodic axis. There are small red lines along this axis to locate AGNR parabolic bands. The dash green lines mark the orientation of ribbon such that pocket K and K' of $NbSe_2$ overlap at the periodic axis.

Depending on the angle θ the low energy bands of the GNR can overlap with the Fermi surface of $NbSe_2$ and strongly hybridize. This can be seen by considering the repeated zone for GNRs shown in red in Fig. 5.11. In the commensurate configuration, the states outside the first BZ of $NbSe_2$ or GNR can be folded to the origin by commensurate translation

reciprocal lattice vector $\mathcal{G}$. The black dots along the blue lines represent the states that are connected by $\mathcal{G}$. At the chosen angle shown in that figure, we see the AGNR parabolic bands overlap with pocket Γ, K, and K'. We can consider particular angle where the ribbon is aligned parallel to dashed green lines. In this case, the pocket K and K' will overlap at the same point along the blue line. As a result, $NbSe_2$ bands become spin degenerate. We expect the induced SOC on GNR due to hybridization reaches minimum value. From this qualitative arguments, we see a possibility to have stacking dependence effect on induced SOC strength.

AGNR on metallic TMD

In this section, we present the electronic structure of AGNR-$NbSe_2$ heterostructure with the structure depicted in Fig.5.12. We set the three integer values (m, p, q) in Eq.5.1 to be $(3, 2, 2)$ for $\theta = 0^0$ and $(3, -4, 4)$ for $\theta = 90^0$. Both of configurations have three primitive cells of AGNR composing the heterostructure supercells. The ribbon is stretched with strain value -5.7% and 8.9% for $\theta = 0^0$ and $\theta = 90^0$ respectively. From their crystal structure, we see that there is a mirror symmetry along the orthogonal direction (y) of ribbon when $\theta = 0^0$. It should be noted that this mirror symmetry depends also on the shift of GNR position not just on rotation angle. In contrast, the configuration with $\theta = 90^0$ exhibits no mirror in-plane symmetry at all. The mirror symmetry along z direction is broken for both configurations which is obviously caused by stacking ribbon on $NbSe_2$.

Figure 5.13(a-b) shows the bandstructure calculated without SOC interaction for $\theta = 0^0$ and $\theta = 90^0$, respectively. We plot the pristine AGNR bands to identify the ribbon parabolic bands in the heterostructure. AGNR become metallic since the ribbon band is shifted up with the parabolic vertex located about 0.3 eV for $\theta = 0^0$ and 0.16 eV for $\theta = 90^0$ above the Fermi level. We still observe the parabolic nature of AGNR band is retained even there are several hybridization points with $NbSe_2$ bands.

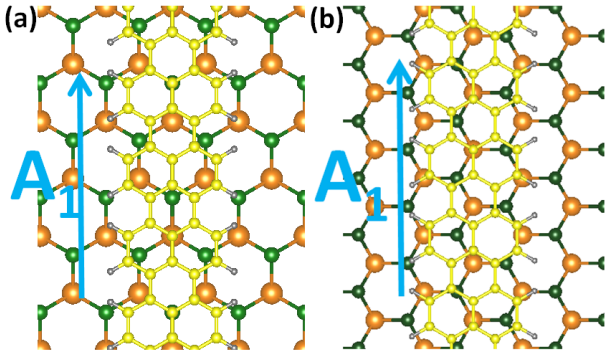

FIG. 5.12: The structure of AGNR (N = 5) on a monolayer $NbSe_2$ is shown in (a) for $\theta = 0^0$ and (b) for $\theta = 90^0$.

Figure 5.13(c-d) shows the bandstructure calculated with SOC interaction. We can identify several $NbSe_2$ bands that are splitted up into several bands. For $\theta = 0^0$, $NbSe_2$ bands are still spin degenerate as the two valeys mixed. For $\theta = 90^0$, the spin degeneracy is removed as the valley K and valley K' are folded at different k point. The bands from pocket Γ have much smaller splitting that is negligible and going to zero for k close to the center.

The metallic properties of $NbSe_2$ will screen the in-plane electric field parallel to the ribbon alignment experienced by AGNR because the electric field is going to be zero in conductor. However, the out of plane and the y axis electric field will not be screening due to the finite thickness of this system and the current only can propagate parallel to ribbon. There is also a charge transfer between ribbon and substrate indicated by the ribbon valence band shifted above the Fermi level. This charge transfer is observed when we use $NbSe_2$ substrate because Nb atom has one electron less than Mo atom. This charge transfer will cause the substrate to be more negative than ribbon. So, we can expect to have induced electric field along z direction. This induced electric field can cause Rashba SOC interaction experienced by the electron in ribbon.

Figure 5.14(a-b) show the states on the band that are formed by finite amount of the

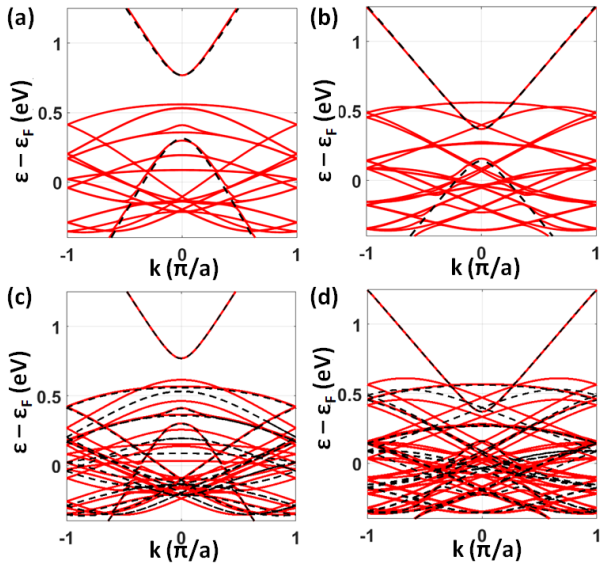

FIG. 5.13: Figure (a-c) and (b-d) are the energy bandstructure of AGNR-$NbSe_2$ with rotation angle $\theta = 0^0$ and $\theta = 90^0$, respectively. The pristine ribbon parabolic bands are given on (a-b) given by the dash lines while the solid lines are the system bands calculated without SOC interaction. The bands with and without SOC interaction are represented with solid and dash lines on figure (c-d), respectively.

carbon atoms. We do a projection to the carbon atoms and filter the states that carry at least 40% of carbon. This data allows us to assess the spin splitting energy experienced by AGNR shown in Figure 5.14(c-d). We see that the splitting energy has peaks when the momentum between $-0.5\frac{\pi}{a} \leq k \leq -0.3\frac{\pi}{a}$ and $0.3\frac{\pi}{a} \leq k \leq 0.5\frac{\pi}{a}$ for both angles. Around these values, AGNR bands are close to the Fermi level where there is higher DOS from $NbSe_2$ system. As a result, strong hybridization between AGNR and $NbSe_2$ bands occurs near the Fermi level. The energy splitting maximum is about 6 meV for $\theta = 0^0$ and 40 meV for $\theta = 90^0$. This huge difference on the splitting energy between these two angle is caused by the folding that we discussed before. At $\theta = 0^0$, $NbSe_2$ bands are spin degenerate. In contrast, $NbSe_2$ bands are spin polarized at $\theta = 90^0$ due to separated valley K and K' after the folding.

Figure 5.14(e-f) display the opening band gap at the avoided crossing point between

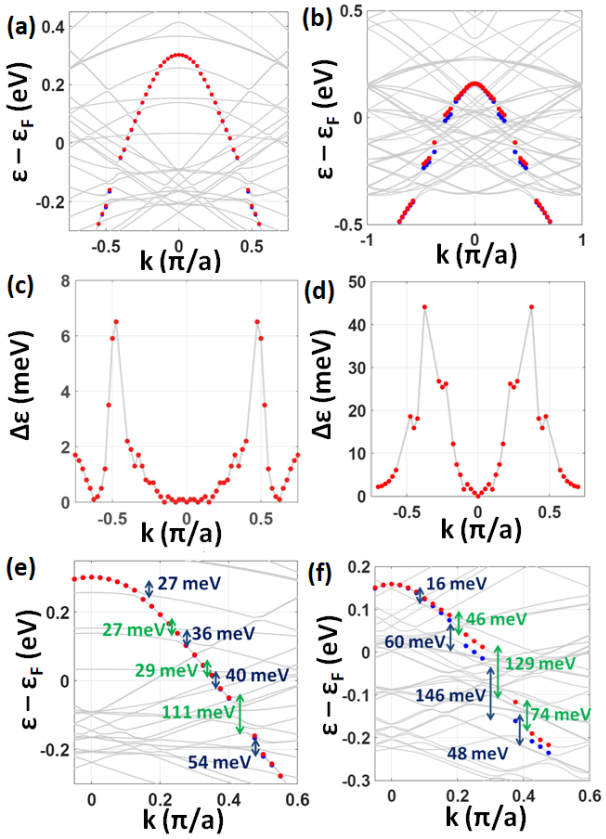

FIG. 5.14: Left and right panel correspond to $\theta = 0^0$ and $\theta = 90^0$, respectively. Figure (a-b) show the ribbon valence bands identified by projection to the Carbon atom states. The red and blue dots represent AGNR states where reds has higher energy than blue dots at each k point. Figure (c-d) are the spin splitting energy of the ribbon valence band calculated by substrating the energy of red and blue dots in (a-b). Figure(e-f) depict the opening band gap at the avoided crossing point on the ribbon valence band.

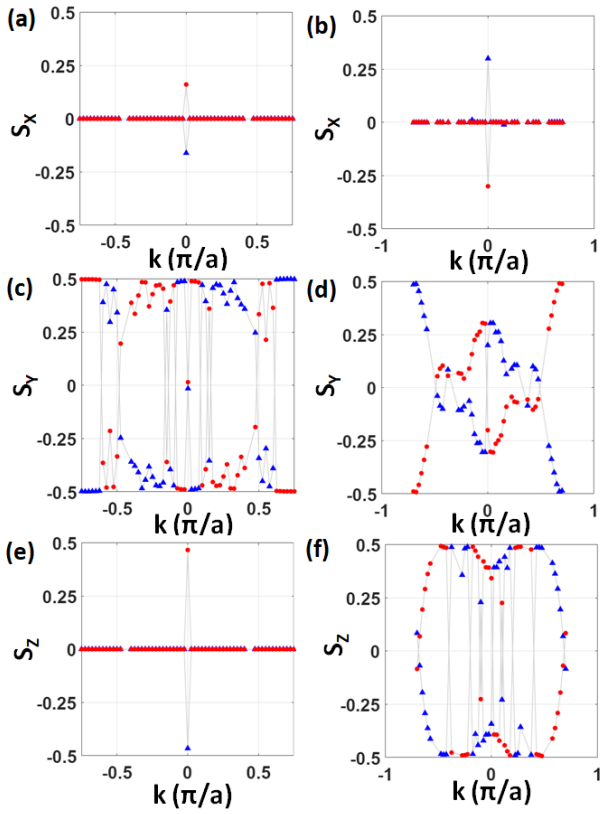

FIG. 5.15: The spin projection in AGNR-$NbSe_2$ system of the ribbon valence states given in Fig.5.14(a-b). Red dot states has energy higher than blue triangle states at each k point. Left and right panel represent the projection plot for $\theta = 0^0$ and $\theta = 90^0$, respectively.

AGNR and $NbSe_2$ bands. When the two bands intersect, the gap could be opened with the magnitude proportional to two times of the hopping energy between these two bands. The magnitude of the hoping depends on the structure of the systems. We can assess the hopping energy between ribbon and substrate by estimating the band gap energy at this points. We see that the band gaps vary between 27 meV to 111 meV for $\theta = 0^0$ suggesting the hopping energy also range from 14 meV to 55 meV. When the rotation angle $\theta = 90^0$, the band gaps vary between 16 meV to 146 meV with the corresponding hopping energy range between 8 meV to 73 meV. It should be noted that the number of substrate bands is increasing close to the Fermi level which means more than two bands intersect with ribbon valence band.

The spin projection was performed and shown in Fig.5.15 for both angles. We see that the spin orientation is orthogonal to the electron momentum k (along x axis) which is a signature of Rashba SOC induced on the system. At k = 0, the spin degeneracy is protected by the time reversal symmetry. The time reversal symmetry also require the state at k has opposite spin with the state at -k and the same energy. This is also something that we observe from the spin projection. This also suggest the possibility to induce p wave superconductor pairing when parallel magnetic field applied on the system.

ZGNR on metallic TMD

We will discuss the electronic structure of ZGNR-$NbSe_2$ calculated using non-relativistic and relativistic pseudopotential for both angles in this section. The crystal structures are shown in Fig.5.16. The three integers in Eq.5.1 are choosen to be $(m = 5, p = -2, q = 2)$ for $\theta = 0^0$ and $(m = 3, p = -2, q = 2)$ for $\theta = 90^0$. The ribbon is stretched by -2% and -5.7% for $\theta = 0^0$ and $\theta = 90^0$, respectively. There is no in-plane mirror symmetry at rotation angle $\theta = 0^0$. We observe the mirror symmetry on the x axis plane at $\theta = 90^0$.

The bandstructure without SOC interaction are depicted in Fig.5.17. The FA ground

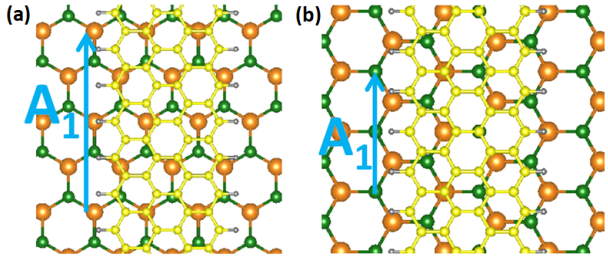

FIG. 5.16: Structure of ZGNR-$NbSe_2$ with $\theta = 0^0$ in (a) and $\theta = 90^0$ in (b).

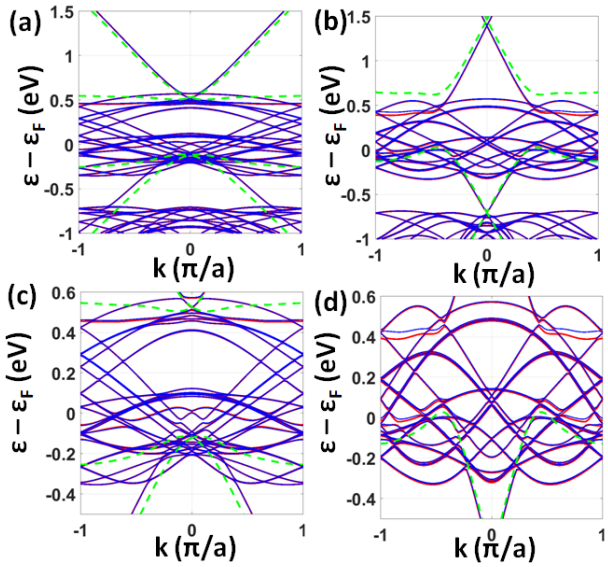

FIG. 5.17: The bandstructure of ZGNR-$NbSe_2$ for $\theta = 0^0$ and $\theta = 90^0$ are depicted in left and panel right, respectively. The bands were calculated without SOC interaction. Solid red and blue lines represent the spin up and spin down bands of the heterostructures. Dash green lines represent the pristine ZGNR bands which are spin degenerate.

state of ZGNR is still retained for both angle in this heterostructure. However, the charge transfer between ribbon and substrate convert the ribbon to be metallic similar with AGNR systems. There is a lot of hybdridization between the ribbon and substrate bands near the Fermi level which makes it difficult to identify ZGNR bands.

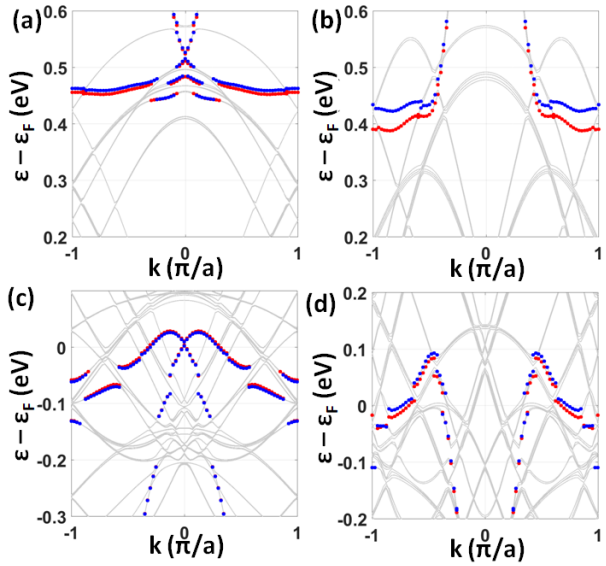

FIG. 5.18: The ribbon bands in ZGNR-$NbSe_2$ system calculated without SOC can be identified from projecting the states to Carbon states. The top and bottom figures show the conduction and valence band of ribbon. Left and right panel are corresponding to $\theta = 0^0$ and $\theta = 90^0$, respectively.

We project the states to atomic orbital of carbon atoms and select the states with at least 30% and 50% of carbon atoms. We plot the conduction and valence bands of ZGNR for system without SOC interaction in Fig.5.18. We observe the opening band gap at the avoided crossing points when ZGNR and $NbSe_2$ bands intersect each other. Our projection also reveals that the edge states are still localized at the edges of ribbon despite placed on metallic substrate.

The spin degeneracy of ZGNR bands is removed due to the staggered sublattice potential as a result of broken sublattice symmetry between the ZGNR edges similar as in ZGNR-$MoSe_2$ structure. We obtain larger spin splitting energy in $NbSe_2$ substrate than in

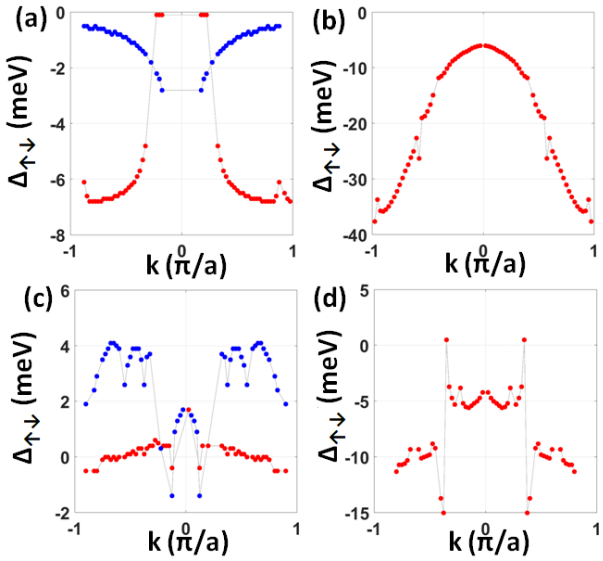

FIG. 5.19: The energy splitting in ZGNR-$NbSe_2$ system without SOC interaction are presented in (a-b) for ribbon conduction band and (c-d) for ribbon valence band. The energy splitting for system without SOC is calculated by calculating the energy difference between spin up and spin down states. The splitting for $\theta = 0^0$ and $\theta = 90^0$ are presented by left and right panel. For $\theta = 0^0$, the blue dots represent the data for the lowest valence band (closest to the Fermi level) and higher conduction band. The red dots represent the data for the higher valence band and lowest conduction band (closest to the Fermi level).

$MoSe_2$ because there is strong hybridization with $NbSe_2$ bands. The energy of ZGNR low energy band is comparable to the $NbSe_2$ low energy band around the fermi level. Figure 5.19 show the spin splitting energy on the ribbon band when there is no SOC interaction. We see that the spin splitting energy of the valence and conduction band for $\theta = 0^0$ vary between 0-10 meV. We also gain much higher splitting energy at $\theta = 90^0$ with the splitting of the valence and conduction band range between 0-15 meV and 0-40 meV, respectively. These large splitting difference between these configurations can be understood qualitatively by comparing their crystal structures in Fig.5.16. At $\theta = 0^0$, the carbon atoms at both edges are alternately positioned near to Nb or Se atoms. On the contrary, the carbon atoms at the left and at the right edge are closer to Nb and Se atoms, respectively, when the rotation angle $\theta = 90^0$. So, in this configuration, the sublattice symmetry between left and right edges are broken with larger electrostatic potential difference.

We turned on the SOC interaction that removes the spin degeneracy on monolayer $NbSe_2$ bands especially for the states around valley K and K'. It is also been pointed out the mixing between valley K and K' due to the folding cause the $NbSe_2$ becomes spin degenerate again at $\theta = 0^0$. Meanwhile, $NbSe_2$ bands are still spin polarized at $\theta = 90^0$. ZGNR-$NbSe_2$ bandstructure with SOC for both rotation angles are presented in Figure 5.20(a-b). The metallic characteristic of $NbSe_2$ is still possessed by the heterostructures.

In order to analyze the ribbon, we project the wavefunctions to atomic orbital of carbon atoms and filter the states that made by at least 60% of carbon. We show the conduction and valence bands of ZGNR in figure (c-d) and (e-f), respectively. From the projection, we also see that the localization of the edge states corresponding to the low energy bands of ZGNR is still preserved. The ZGNR valence energy band is shifted up giving the maximum valence band at 0.03 eV for $\theta = 0^0$ and 0.09 eV for $\theta = 90^0$ above the Fermi level. The ZGNR band gap in this heterostructure is reduced by 36% relative to its pristine band gap about 0.62 eV for $\theta = 0^0$. At $\theta = 90^0$, the ZGNR energy band gap

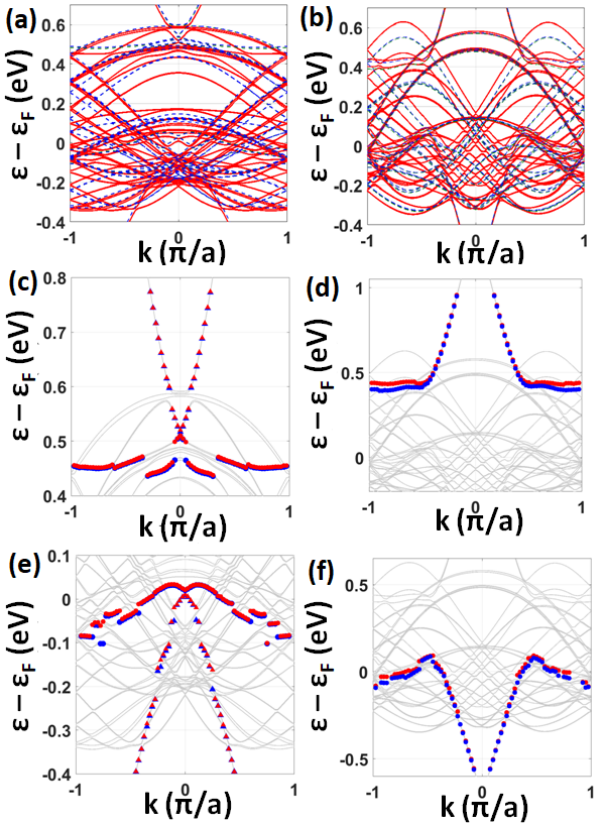

FIG. 5.20: The bandstructure of ZGNR-$NbSe_2$ for $\theta = 0^0$ and $\theta = 90^0$ are depicted in left and panel right, respectively. The bands were calculated with SOC interaction. In (a-b), solid red and dash blue represent the bands of the heterostructures calculated with or without SOC. In (c-d) and (e-f), we have the conduction and valence band of ribbon calculated by projection to the carbon states. Red dots mark the states with energy higher than states marked by blue dots.

is reduced by 50% relative to the pristine band gap about 0.6 eV. This means that the FA ground state still exist even if the exchange interaction responsible for this magnetic state is smaller. It should be noted that the band gap in this system is proportional to on-site Hubbard interaction on each edge. This interaction depends on the electron density which is reduced because of charge transfer from ZGNR to $NbSe_2$.

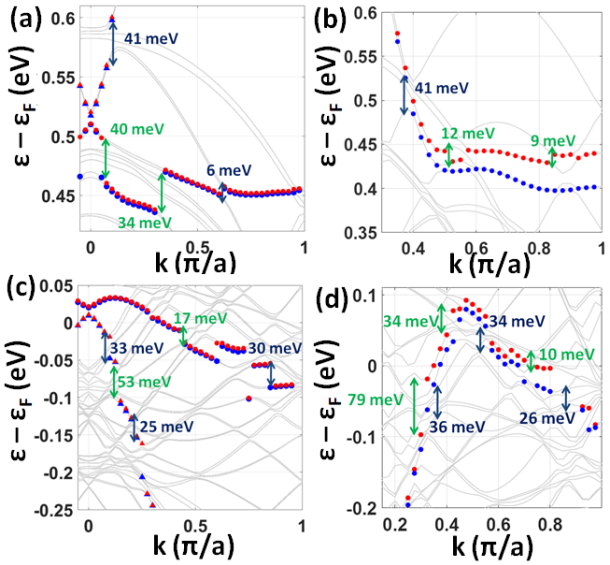

FIG. 5.21: The opening band gap in ZGNR-$NbSe_2$ with SOC interaction for $\theta = 0^0$ and $\theta = 90^0$ are depicted in left and panel right, respectively. The band gap at conduction and valence band are given in (a-b) and (c-d), respectively.

We want to address that the strength of the induced superconductivity pairing in ribbon in the lowest order will be proportional to t^2 where t is the hopping energy between ribbon and the superconductor substrate. From this DFT study, we can assess the magnitude of hopping by identifying the opening band gap at the avoided crossing point as the hopping energy should be proportional to the band gap energy. In figure 5.21, the band gaps for $\theta = 0^0$ vary from 17 meV to 53 meV in the valence band and from 6 meV to 41 meV in conduction band. For $\theta = 90^0$, the band gaps vary between 10 meV to 79 meV in valence band and from 9 meV to 41 meV in conduction band.

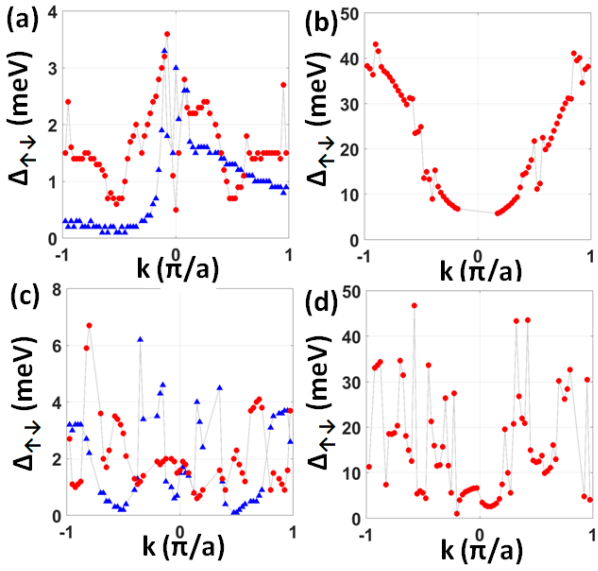

FIG. 5.22: The energy splitting of ZGNR-$NbSe_2$ with SOC interaction for $\theta = 0^0$ and $\theta = 90^0$ are depicted in left and panel right, respectively. The splitting at conduction and valence band are given in (a-b) and (c-d), respectively.

The spin splitting energy is enhanced when SOC interaction presence in the system especially for $\theta = 90^0$. The conduction band still has the splitting energy range from 0 to 40 meV which is similar with the case no SOC. On the contrary, we see that the splitting energy at the valence band is growing with the maximum value about 45 meV which is three times than the maximum value in the case no SOC. The ribbon hybridize with spin polarized band of $NbSe_2$ due to the SOC and the folding that do not mix valley K and K'.

The spin projection on the ribbon bands is given in Fig.5.23 for $\theta = 90^0$. We obtain the spin orientation on the conduction band are polarized to z direction. The electron spin on the valence band is sligthly tilted to y axis. For both bands, the electron has no component on x axis which is parallel to ribbon alignment indicating Rashba type SOC induced on ribbon. As the time reversal symmetry is broken, the spin at k does not need to be opposite with spin at -k. This can forbid the induced pairing on ribbon by proximity

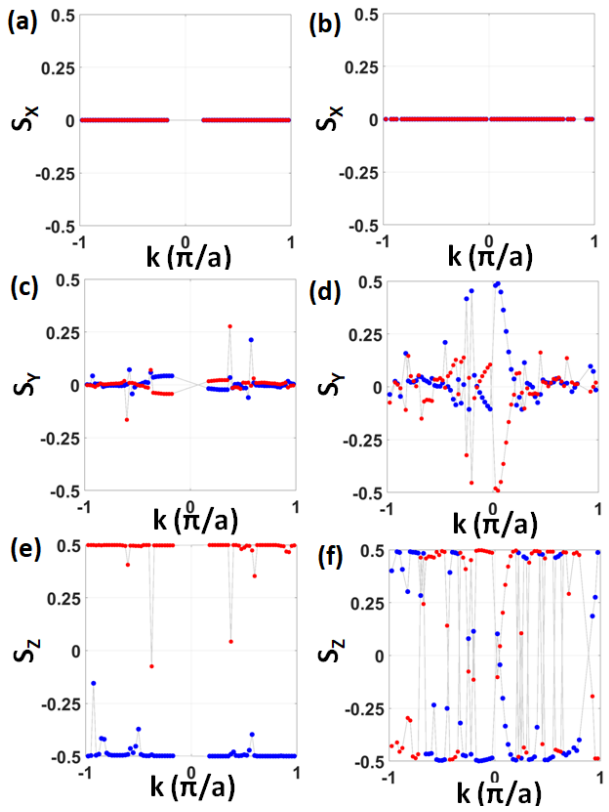

FIG. 5.23: The spin projection on the conduction and valence band given in left and right panel, respectively, for configuration with $\theta = 90^0$. Red dots are corresponding to the state with higher energy than the blue dots on the valence or conduction bands.

from s-wave superconductor.

It is interesting to see the electronic structure of ZGNR-$NbSe_2$ in different magnetic ground state. From previous study (lee 2005), the FA ground state is more favorable than FF ground state in the pristine ZGNR with narrow ribbon width because the constructive interference between magnetic tails from both edges in FA ground state gives larger exchange energy gain. When the ribbon width is increasing, the energy difference between these two ground states is getting smaller as the consequence of finite magnetic tail length. In our simulation, we choose narrow ribbon with N = 4 where each carbon atom have energy 1.7 meV lower in FA ground state than in FF ground state. However, when we placed the ribbon with FF state in $NbSe_2$, we observe its total system energy is lower than the system with FA magnetic state. The binding energy for each carbon atom -13.13 meV in FF state compared with -11.32 meV when it is in FA magnetic state. When the pristine ZGNR (N = 4) is set to be non-magnetic (NM), each carbon atom has energy 6.4 meV higher than when it is in FA state. The NM state still has higher energy than FA and FF state when it is placed on $NbSe_2$ with binding energy -16.1 meV per carbon atom.

Figure 5.24 (a) shows the bandstructure of pristine ribbon in FF state where the low energy are mostly spin polarized band from particular spin. At $k = \pm\frac{\pi}{a}$, the wavefunctions are localized at both edges where they have similar orientation of spin. Figure (b) shows the bandstucture of pristine ribbon in NM state. We see that in this case the bands have spin and sublattice degeneracy from both edges. Figure 5.24 (c-d) shows the bandstructure FF and NM state of ZGNR on $NbSe_2$ with $\theta = 90^0$. We see that the ZGNR is also hole doped as other configurations. The energy difference between spin up and down of ZGNR is reduced which also tells us the smaller magnitude of exchange interaction comparing to the pristine case.

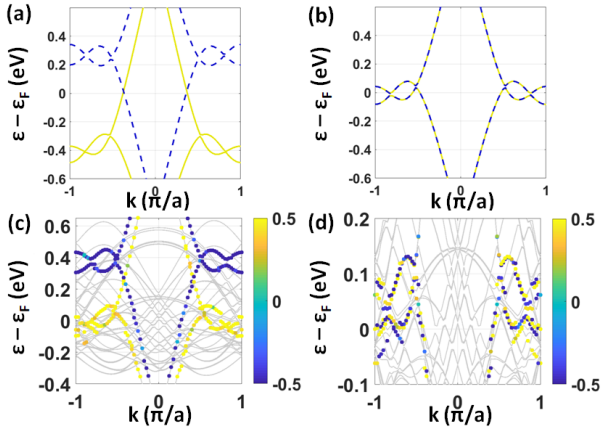

FIG. 5.24: Figure (a) shows the bandstructure of pristine ZGNR (N = 4) in ferromagnetic state (FF). The solid (yellow) and dash (blue) lines identify the spin up and spin down bands, respectively. Figure (b) shows the bandstructure of ZGNR on $NbSe_2$ where we set ZGNR in FF state. We also project the wavefunction to atomic orbital of Carbon to identify the bands from ribbon. The color bar provides the information of spin on z direction. (c) presents the bandstructure of ZGNR (N = 4) in non-magnetic (NM) state. (d) presents the bandstructure of ZGNR (NM) on $NbSe_2$ with $\theta = 90^0$.

5.3 Conclusion

We have studied the electronic structure of Armchair-GNR and Zigzag-GNR in the presence of semiconducting and metallic substrates using first principals calculations. We construct the heterostructures by stacking GNR on monolayer $MoSe_2$ and $NbSe_2$.

Our results show the semiconducting nature of GNR is retained on $MoSe_2$, the substrate. The GNR low energy bands are located within $MoSe_2$ band gap to serve as the low energy of the combined systems. GNR band gap is slightly reduced between 2% to 5% of its pristine band energy gap value. $MoSe_2$ can induce spin orbit coupling in AGNR with features such as Rashba SOC due to the induced electric field cause by the broken inversion symmetry. The strength of the SOC potential is about 7 meVÅ which corresponds to a spin splitting energy of about 1-2 meV, which is similar in magnitude to the spin splitting induced in a graphene layer by proximity effect from monolayer $MoSe_2$ or MoS_2 [6, 45]. We do not observe strong dependence of the induced SOC on the stacking configuration

between AGNR and $MoSe_2$.

In ZGNR-$MoSe_2$ system, the Ferro-Antiferromagnetic (FA) magnetic ground state of ZGNR with the localized edge states is still observed in the system. The spin splitting energy can reach up to 5 meV for rotation angle $\theta = 90^0$. The two edges of the ZGNR have different local atomic configurations that generate a staggered potential energy. The right and left edges are formed by different sublattices. Hence, the staggered potential between the edges will break the symmetry of the two sublattices. Each of the spin states in the valence or conduction bands couple to only one of the sublattices. By breaking this sublattice symmetry, the spin degeneracy will also be removed. As a further consequence, the spin splitting energy is sensitive to how ZGNR is stacked on $MoSe_2$. Our calculations show that the spin splitting energy is smaller than 1 meV for $\theta = 0^0$.

On the contrary, when we used $NbSe_2$ as the substrate, GNR becomes metallic due to charge transfer from the ribbon to $NbSe_2$. The valence band of GNR is shifted up above the fermi level for armchair and zigzag edge shapes. Strong hybridization between GNR and $NbSe_2$ bands leads to the avoided crossing points with the band gap energies varying from 10 meV to 100 meV. This corresponds to a hopping energy from 5 meV to 50 meV. It has been shown that this hopping energy is enough to induce superconducting Ising pairing in graphene stacked on monolayer $NbSe_2$ [192].

For both types of GNR, there is strong dependence of the induced SOC on the stacking configuration between GNR and $NbSe_2$. Besides the induced electric field that generates Rashba type of SOC, there is another mechanism responsible to the spin splitting of GNR bands. The hybridization with $NbSe_2$ bands can give larger effect for certain rotation angles such that AGNR sees the valley K and K' of $NbSe_2$ folded to different k points. In this case, for example when $\theta = 90^0$, $NbSe_2$ exhibits spin polarized bands resulting in asymmetry of the spin dependent hybridization. The spin splitting is enhanced to give a maximum value up to 40 meV, which is almost 5 times the spin splitting in the case for

$\theta = 0^0$.

The spin splitting of ZGNR in $NbSe_2$ is also caused by the broken sublattice symmetry. The relative position of the ZGNR edges with respect to $NbSe_2$ determines the spin splitting energy in ZGNR bands. We can obtain the splitting energy up to 35 meV for $\theta = 90^0$. This value is also much larger than the splitting maximum when we used $MoSe_2$ substrate.

We also demonstrate the degeneracy of ZGNR ground state in the presence of metallic substrate. FA and FF magnetic ground state energies are comparable to each other. The magnetic interaction, which is modeled with a Hubbard interaction, depends on the electron density that is localized on both edges. The hybridization reduces these localization on the edges which further decreases the magnetic interaction.

Our calculation suggest the possibility to implement AGNR or ZGNR stacked on monolayer $NbSe_2$ as the platform to observe Majorana bound state. There are several features of GNR that makes this system better than the current Majorana platform. First, a GNR has a much smaller size, which is only a one layer thickness. Second, there is a large energy difference between subbands that could isolate a pair of Majorana states from the higher subbands. This can prevent the annihilation of Majorana pair to form a trivial state. Third, the geometry of a GNR is less sophisticated than a InAs nanowire, which has a hexagonal cross section for the area perpendicular to the wire. Fourth, the superconducting Ising pairing can be easily induced by proximity effect from monolayer $NbSe_2$.

CHAPTER 6

Summary

We have demonstrated to utilize the van der Waals heterostructures of two-dimensional system to realize a tunable electronic device with the desire features. The weak interactions between the layers could retain the electronic characteristic of each individual layer. The energy band modification can happen in a perturbative way as long as the interaction is small through electron tunneling and electrostatic effect. We also can obtain a strong hybridization between the systems when the corresponding hybridized bands have small energy difference. As each layer could have different periodicity, the new systems can have new commensurate configuration with different periodicity, which is identified by the existence of a Moiré pattern. The overall crystal translation symmetry also can be broken in effect that the Bloch theorem is not valid. In this case, the study of electronic structure can be performed by using perturbation method in the continuum model [83].

We have presented our study about the superconductivity in graphene-$NbSe_2$ heterostructures. We model the system using perturbation in the continuum model with the parameters obtained from first principals calculation. We showed that the superconductivity pairing can be induced on a graphene layer by proximity effect regardless their large

lattice constant difference. The nature of the induced pairing is very persistent to the external in-plane magnetic field which indicates the existence of the induced Ising SOC in graphene layer. This Ising SOC will lock the spin in out of plane direction which contributes to the protection of the superconducting pairing under external field. We also showed that the induced gap is a function of rotation angle between graphene and $NbSe_2$. Our model can be generalized to other TMD system such as NbS_2, TaS_2, or $TaSe_2$. We do not close the possibility to implement to other systems in general where the Fermi surface overlaps are important to realize the hybridization between these systems. There could be a significant change in the Fermi surface of monolayer $NbSe_2$ when charge density wave presences. When this happen, the relation between the rotation angle and the induced gap needs to be modified. So our results is limited to the situation where charge density wave does not strongly change the fermi surface of $NbSe_2$.

It is important to use the substrate as a platform to grow one or two-dimensional systems. One of the candidate is by using an inert material or insulator with a large band such as hBN. However, hBN can affect the low energy bands of graphene by opening a band gap at the Dirac point on the order of 50 meV [143]. Therefore, we studied the electronic properties of graphene nanoribbon (GNR) on monolayer hexagonal boron nitride (hBN) to see the effect of hBN in the ribbon for armchair (AGNR) and zigzag (ZGNR) types. The semiconducting properties of GNR are still preserved and pinned within the hBN band gap. For AGNR-hBN systems, we see that the AGNR band gap variation reaching up to 20% relative to the pristine AGNR band gap. For ZGNR-hBN system, we observe that the spin degeneracy is lifted due to the broken sublattice symmetry between the edges. The spin splitting energy can reach up to 40 meV. This implies that ZGNR-hBN can be used in spintronic device application where the spin transport is carried along this one-dimensional system. In general, our results demonstrate that monolayer hBN can be effectively used as the substrate of the ribbon considering small change in GNR electronic properties. There

are still many questions that remain to be answered for this heterostructures such as the effect of ripple on GNR or the presence of the impurity or phonon.

We also studied the heterostructures formed by GNR on monolayer transition metal dichalcogenides (TMD) materials. We considered two different TMDs with semiconducting and metallic properties. This study is motivated from a strong interest to realize Majorana bound state in the one-dimensional system such as InAs nanowire [9]. The key ingredients are spin orbit coupling and superconductivity which can be obtained from TMD substrate. We investigate the strength of SOC on GNR which is induced from $MoSe_2$ and $NbSe_2$ monolayer. We saw the SOC with Rashba characteristic when we placed AGNR on $MoSe_2$ with SOC strength about $5 - 7\,\text{meV}\text{Å}$. When we placed AGNR on $NbSe_2$ substrate, the induced SOC has larger magnitude due to strong hybridization between the two systems. The splitting can reach up to 40 meV. We also study the dependence of the induced SOC with respect to stacking configuration between GNR and TMD. There is a strong relation between the stacking and the induced SOC on GNR when we use $NbSe_2$ substrate.

BIBLIOGRAPHY

[1] S. Das Sarma, S. Adam, E. H. Hwang, and E. Rossi, Rev. Mod. Phys. **83**, 407 (2011).

[2] K. Bolotin, K. Sikes, Z. Jiang, M. Klima, G. Fudenberg, J. Hone, P. Kim, and H. Stormer, Solid State Communications **146**, 351 (2008).

[3] A. A. Balandin, S. Ghosh, W. Bao, I. Calizo, D. Teweldebrhan, F. Miao, and C. N. Lau, Nano Letters **8**, 902 (2008).

[4] C. L. Kane and E. J. Mele, Phys. Rev. Lett. **95**, 226801 (2005).

[5] S. Konschuh, M. Gmitra, and J. Fabian, Phys. Rev. B **82**, 245412 (2010).

[6] M. Gmitra and J. Fabian, Phys. Rev. B **92**, 155403 (2015).

[7] A. Y. Kitaev, Physics-Uspekhi **44**, 131 (2001).

[8] J. Alicea, Y. Oreg, G. Refael, F. von Oppen, and M. P. A. Fisher, Nature Physics **7**, 412 (2011).

[9] A. Das, Y. Ronen, Y. Most, Y. Oreg, M. Heiblum, and H. Shtrikman, Nature Physics **8**, 887 (2012).

[10] T. D. Stanescu, R. M. Lutchyn, and S. Das Sarma, Phys. Rev. B **84**, 144522 (2011).

[11] A. Tkatchenko, Advanced Functional Materials **25**, 2054, https://onlinelibrary.wiley.com/doi/pdf/10.1002/adfm.201403029 .

[12] G. W. Shim, K. Yoo, S.-B. Seo, J. Shin, D. Y. Jung, I.-S. Kang, C. W. Ahn, B. J. Cho, and S.-Y. Choi, ACS Nano **8**, 6655 (2014).

[13] K. Capelle, Brazilian Journal of Physics **36**, 1318 (2006).

[14] U. von Barth and L. Hedin, Journal of Physics C: Solid State Physics **5**, 1629 (1972).

[15] D. M. Ceperley and B. J. Alder, Phys. Rev. Lett. **45**, 566 (1980).

[16] J. P. Perdew and A. Zunger, Phys. Rev. B **23**, 5048 (1981).

[17] P. G. De Gennes, *Superconductivity of Metals and Alloys* (Chapman and Hall/CRC, 2018).

[18] J. Bardeen, L. N. Cooper, and J. R. Schrieffer, Phys. Rev. **108**, 1175 (1957).

[19] R. A. Bromley, R. B. Murray, and A. D. Yoffe, Journal of Physics C: Solid State Physics **5**, 759 (1972).

[20] K. F. Mak, C. Lee, J. Hone, J. Shan, and T. F. Heinz, Phys. Rev. Lett. **105**, 136805 (2010).

[21] S. Lebègue and O. Eriksson, Phys. Rev. B **79**, 115409 (2009).

[22] H. Rostami, A. G. Moghaddam, and R. Asgari, Phys. Rev. B **88**, 085440 (2013).

[23] E. Cappelluti, R. Roldán, J. A. Silva-Guillén, P. Ordejón, and F. Guinea, Phys. Rev. B **88**, 075409 (2013).

[24] J. P. Perdew, K. Burke, and M. Ernzerhof, Phys. Rev. Lett. **77**, 3865 (1996).

[25] J. Gusakova, X. Wang, L. L. Shiau, A. Krivosheeva, V. Shaposhnikov, V. Borisenko, V. Gusakov, and B. K. Tay, physica status solidi (a) **214**, 1700218, https://onlinelibrary.wiley.com/doi/pdf/10.1002/pssa.201700218 .

[26] K. F. Mak, K. He, J. Shan, and T. F. Heinz, Nature Nanotechnology **7**, 494 EP (2012).

[27] D. Xiao, G.-B. Liu, W. Feng, X. Xu, and W. Yao, Phys. Rev. Lett. **108**, 196802 (2012).

[28] D. Xiao, M.-C. Chang, and Q. Niu, Rev. Mod. Phys. **82**, 1959 (2010).

[29] Y. D. Chong, Phys. Rev. B **81**, 052303 (2010).

[30] G. Sundaram and Q. Niu, Phys. Rev. B **59**, 14915 (1999).

[31] D. Xiao, J. Shi, and Q. Niu, Phys. Rev. Lett. **95**, 137204 (2005).

[32] W. Feng, Y. Yao, W. Zhu, J. Zhou, W. Yao, and D. Xiao, Phys. Rev. B **86**, 165108 (2012).

[33] Y. Noat, J. A. Silva-Guillén, T. Cren, V. Cherkez, C. Brun, S. Pons, F. Debontridder, D. Roditchev, W. Sacks, L. Cario, P. Ordejón, A. García, and E. Canadell, Phys. Rev. B **92**, 134510 (2015).

[34] W. L. McMillan, Phys. Rev. **175**, 537 (1968).

[35] S. V. Borisenko, A. A. Kordyuk, V. B. Zabolotnyy, D. S. Inosov, D. Evtushinsky, B. Büchner, A. N. Yaresko, A. Varykhalov, R. Follath, W. Eberhardt, L. Patthey, and H. Berger, Phys. Rev. Lett. **102**, 166402 (2009).

[36] T. Dvir, F. Massee, L. Attias, M. Khodas, M. Aprili, C. H. L. Quay, and H. Steinberg, Nature Communications **9** (2018), 10.1038/s41467-018-03000-w.

[37] M. Tinkham, *Introduction to Superconductivity: Second Edition (Dover Books on Physics) (Vol i)*, second edition ed. (Dover Publications, 2004).

[38] X. Xi, Z. Wang, W. Zhao, J.-H. Park, K. T. Law, H. Berger, L. Forró, J. Shan, and K. F. Mak, Nature Physics **12**, 139 (2015).

[39] A. H. Castro Neto, F. Guinea, N. M. R. Peres, K. S. Novoselov, and A. K. Geim, Rev. Mod. Phys. **81**, 109 (2009).

[40] H. Min, J. E. Hill, N. A. Sinitsyn, B. R. Sahu, L. Kleinman, and A. H. MacDonald, Phys. Rev. B **74**, 165310 (2006).

[41] Y. Yao, F. Ye, X.-L. Qi, S.-C. Zhang, and Z. Fang, Phys. Rev. B **75**, 041401 (2007).

[42] J. C. Boettger and S. B. Trickey, Phys. Rev. B **75**, 121402 (2007).

[43] M. Gmitra, S. Konschuh, C. Ertler, C. Ambrosch-Draxl, and J. Fabian, Phys. Rev. B **80**, 235431 (2009).

[44] I. Nikiforov, E. Dontsova, R. D. James, and T. Dumitrică, Phys. Rev. B **89**, 155437 (2014).

[45] M. Gmitra, D. Kochan, P. Högl, and J. Fabian, Phys. Rev. B **93**, 155104 (2016).

[46] G. Lee and K. Cho, Phys. Rev. B **79**, 165440 (2009).

[47] K. Nakada, M. Fujita, G. Dresselhaus, and M. S. Dresselhaus, Phys. Rev. B **54**, 17954 (1996).

[48] D. Gunlycke and C. T. White, Phys. Rev. B **77**, 115116 (2008).

[49] L. Brey and H. A. Fertig, Phys. Rev. B **73**, 235411 (2006).

[50] H. Zheng, Z. F. Wang, T. Luo, Q. W. Shi, and J. Chen, Phys. Rev. B **75**, 165414 (2007).

[51] Y.-W. Son, M. L. Cohen, and S. G. Louie, Phys. Rev. Lett. **97**, 216803 (2006).

[52] A. Ramasubramaniam, Phys. Rev. B **86**, 115409 (2012).

[53] D. W. Latzke, W. Zhang, A. Suslu, T.-R. Chang, H. Lin, H.-T. Jeng, S. Tongay, J. Wu, A. Bansil, and A. Lanzara, Phys. Rev. B **91**, 235202 (2015).

[54] M. A. Cazalilla, H. Ochoa, and F. Guinea, Phys. Rev. Lett. **113**, 077201 (2014).

[55] Q. H. Wang, K. Kalantar-Zadeh, A. Kis, J. N. Coleman, and M. S. Strano, Nature Nanotechnology **7**, 699 (2012).

[56] Z. Wang, D. Ki, H. Chen, H. Berger, A. H. MacDonald, and A. F. Morpurgo, Nature Communications **6** (2015), 10.1038/ncomms9339.

[57] K.-A. N. Duerloo, Y. Li, and E. J. Reed, Nature Communications **5** (2014), 10.1038/ncomms5214.

[58] M. M. Ugeda, A. J. Bradley, Y. Zhang, S. Onishi, Y. Chen, W. Ruan, C. Ojeda-Aristizabal, H. Ryu, M. T. Edmonds, and H.-Z. e. a. Tsai, Nature Physics **12**, 92 (2015).

[59] X. Xi, L. Zhao, Z. Wang, H. Berger, L. Forró, J. Shan, and K. F. Mak, Nature Nanotechnology **10**, 765 (2015).

[60] X. Xu, W. Yao, D. Xiao, and T. F. Heinz, Nature Physics **10**, 343 (2014).

[61] T. Böker, R. Severin, A. Müller, C. Janowitz, R. Manzke, D. Voß, P. Krüger, A. Mazur, and J. Pollmann, Phys. Rev. B **64**, 235305 (2001).

[62] Y. Ding, Y. Wang, J. Ni, L. Shi, S. Shi, and W. Tang, Physica B: Condensed Matter **406**, 2254 (2011).

[63] J. M. Lu, O. Zheliuk, I. Leermakers, N. F. Q. Yuan, U. Zeitler, K. T. Law, and J. T. Ye, Science **350**, 1353 (2015).

[64] Y. Saito, Y. Nakamura, M. S. Bahramy, Y. Kohama, J. Ye, Y. Kasahara, Y. Nakagawa, M. Onga, M. Tokunaga, and T. e. a. Nojima, Nature Physics **12**, 144 (2015).

[65] S. C. de la Barrera, M. R. Sinko, D. P. Gopalan, N. Sivadas, K. L. Seyler, K. Watanabe, T. Taniguchi, A. W. Tsen, X. Xu, and D. e. a. Xiao, Nature Communications **9** (2018), 10.1038/s41467-018-03888-4.

[66] C. R. Dean, A. F. Young, I. Meric, C. Lee., L. Wang, S. Sorgenfrei, K. Watanabe, T. Taniguchi, P. Kim, K. L. Shepard, and J. Hone, Nature Nanotechnology **5**, 726 (2010).

[67] A. K. Geim and I. V. Grigorieva, Nature **499**, 419 (2013).

[68] L. Kou, B. Yan, F. Hu, S.-C. Wu, T. O. Wehling, C. Felser, C. Chen, and T. Frauenheim, Nano Letters **13**, 6251 (2013), https://doi.org/10.1021/nl4037214 .

[69] L. Zhang, Y. Yan, H.-C. Wu, D. Yu, and Z.-M. Liao, ACS Nano **10**, 3816 (2016), pMID: 26930548, https://doi.org/10.1021/acsnano.6b00659 .

[70] J. Zhang, C. Triola, and E. Rossi, Phys. Rev. Lett. **112**, 096802 (2014).

[71] A. Zalic, T. Dvir, and H. Steinberg, Phys. Rev. B **96**, 075104 (2017).

[72] M. Rodriguez-Vega, G. Schwiete, J. Sinova, and E. Rossi, Phys. Rev. B **96**, 235419 (2017).

[73] K. S. Novoselov, A. K. Geim, S. V. Morozov, D. Jiang, M. I. Katsnelson, I. V. Grigorieva, S. V. Dubonos, and A. A. Firsov, Nature **438**, 197 (2005).

[74] E. Rossi, S. Adam, and S. D. Sarma, Phys. Rev. B **79**, 245423 (2009).

[75] M. Rodriguez-Vega, J. Fischer, S. Das Sarma, and E. Rossi, Phys. Rev. B **90**, 035406 (2014).

[76] E. Khestanova, J. Birkbeck, M. Zhu, Y. Cao, G. L. Yu, D. Ghazaryan, J. Yin, H. Berger, L. Forró, T. Taniguchi, K. Watanabe, R. V. Gorbachev, A. Mishchenko, A. K. Geim, and I. V. Grigorieva, Nano Letters **18**, 2623 (2018), pMID: 29529377, https://doi.org/10.1021/acs.nanolett.8b00443 .

[77] M. Leroux, P. Rodière, L. Cario, and T. Klein, Physica B: Condensed Matter **407**, 1813 (2012), proceedings of the International Workshop on Electronic Crystals (ECRYS-2011).

[78] J. Kačmarčík, Z. Pribulová, C. Marcenat, T. Klein, P. Rodière, L. Cario, and P. Samuely, Phys. Rev. B **82**, 014518 (2010).

[79] E. Navarro-Moratalla, J. O. Island, S. Mañas-Valero, E. Pinilla-Cienfuegos, A. Castellanos-Gomez, J. Quereda, G. Rubio-Bollinger, L. Chirolli, J. A. Silva-Guillén, and N. e. a. Agraït, Nature Communications **7** (2016), 10.1038/ncomms11043.

[80] P. Giannozzi, S. Baroni, N. Bonini, M. Calandra, R. Car, C. Cavazzoni, D. Ceresoli, G. L. Chiarotti, M. Cococcioni, I. Dabo, A. Dal Corso, S. de Gironcoli, S. Fabris, G. Fratesi, R. Gebauer, U. Gerstmann, C. Gougoussis, A. Kokalj, M. Lazzeri, L. Martin-Samos, N. Marzari, F. Mauri, R. Mazzarello, S. Paolini, A. Pasquarello, L. Paulatto, C. Sbraccia, S. Scandolo, G. Sclauzero, A. P. Seitsonen, A. Smogunov, P. Umari, and R. M. Wentzcovitch, Journal of Physics: Condensed Matter **21**, 395502 (19pp) (2009).

[81] P. Giannozzi, O. Andreussi, T. Brumme, O. Bunau, M. B. Nardelli, M. Calandra, R. Car, C. Cavazzoni, D. Ceresoli, M. Cococcioni, N. Colonna, I. Carnimeo, A. D. Corso, S. de Gironcoli, P. Delugas, R. A. D. Jr, A. Ferretti, A. Floris, G. Fratesi,

G. Fugallo, R. Gebauer, U. Gerstmann, F. Giustino, T. Gorni, J. Jia, M. Kawamura, H.-Y. Ko, A. Kokalj, E. Küçükbenli, M. Lazzeri, M. Marsili, N. Marzari, F. Mauri, N. L. Nguyen, H.-V. Nguyen, A. O. de-la Roza, L. Paulatto, S. Poncé, D. Rocca, R. Sabatini, B. Santra, M. Schlipf, A. P. Seitsonen, A. Smogunov, I. Timrov, T. Thonhauser, P. Umari, N. Vast, X. Wu, and S. Baroni, Journal of Physics: Condensed Matter **29**, 465901 (2017).

[82] E. J. Mele, Phys. Rev. B **81**, 161405 (2010).

[83] R. Bistritzer and A. H. MacDonald, Proceedings of the National Academy of Sciences **108**, 12233 (2011), http://www.pnas.org/content/108/30/12233.full.pdf .

[84] J. Lopes dos Santos, N. Peres, and A. Castro Neto, Phys. Rev. Lett. **99**, 256802 (2007).

[85] H. Steinberg, L. A. Orona, V. Fatemi, J. D. Sanchez-Yamagishi, K. Watanabe, T. Taniguchi, and P. Jarillo-Herrero, Phys. Rev. B **92**, 241409 (2015).

[86] C.-P. Lu, M. Rodriguez-Vega, G. Li, A. Luican-Mayer, K. Watanabe, T. Taniguchi, E. Rossi, and E. Y. Andrei, Proceedings of the National Academy of Sciences **113**, 6623 (2016).

[87] Y. Cao, V. Fatemi, S. Fang, K. Watanabe, T. Taniguchi, E. Kaxiras, and P. Jarillo-Herrero, Nature **556**, 43 (2018).

[88] Y. Cao, V. Fatemi, A. Demir, S. Fang, S. L. Tomarken, J. Y. Luo, J. D. Sanchez-Yamagishi, K. Watanabe, T. Taniguchi, E. Kaxiras, R. C. Ashoori, and P. Jarillo-Herrero, Nature **556**, 80 (2018).

[89] M. Yankowitz, S. Chen, H. Polshyn, Y. Zhang, K. Watanabe, T. Taniguchi,

D. Graf, A. F. Young, and C. R. Dean, Science **363**, 1059 (2019), http://science.sciencemag.org/content/363/6431/1059.full.pdf .

[90] S. Huang, K. Kim, D. K. Efimkin, T. Lovorn, T. Taniguchi, K. Watanabe, A. H. MacDonald, E. Tutuc, and B. J. LeRoy, Phys. Rev. Lett. **121**, 037702 (2018).

[91] M. Ezawa, Phys. Rev. B **73**, 045432 (2006).

[92] V. Barone, O. Hod, and G. E. Scuseria, Nano Letters **6**, 2748 (2006), pMID: 17163699.

[93] M. Fujita, K. Wakabayashi, K. Nakada, and K. Kusakabe, Journal of the Physical Society of Japan **65**, 1920 (1996), https://doi.org/10.1143/JPSJ.65.1920 .

[94] L. Yang, C.-H. Park, Y.-W. Son, M. L. Cohen, and S. G. Louie, Phys. Rev. Lett. **99**, 186801 (2007).

[95] S. Dutta and S. K. Pati, Journal of Materials Chemistry **20**, 8207 (2010).

[96] J. J. Palacios, J. Fernandez-Rossier, L. Brey, and H. A. Fertig, Semiconductor Science Technology **25**, 033003 (2010).

[97] J. Cai, P. Ruffieux, R. Jaafar, M. Bieri, T. Braun, S. Blankenburg, M. Muoth, A. P. Seitsonen, M. Saleh, and X. e. a. Feng, Nature **466**, 470 (2010).

[98] P. Ruffieux, S. Wang, B. Yang, C. Sánchez-Sánchez, J. Liu, T. Dienel, L. Talirz, P. Shinde, C. A. Pignedoli, and D. e. a. Passerone, Nature **531**, 489 (2016).

[99] A. Narita, X. Feng, Y. Hernandez, S. A. Jensen, M. Bonn, H. Yang, I. A. Verzhbitskiy, C. Casiraghi, M. R. Hansen, and A. H. R. e. a. Koch, Nature Chemistry **6**, 126 (2013).

[100] M. Slota, A. Keerthi, W. K. Myers, E. Tretyakov, M. Baumgarten, A. Ardavan, H. Sadeghi, C. J. Lambert, A. Narita, K. Müllen, and L. Bogani, Nature **557**, 691 (2018).

[101] O. Gröning, S. Wang, X. Yao, C. A. Pignedoli, G. Borin Barin, C. Daniels, A. Cupo, V. Meunier, X. Feng, and A. e. a. Narita, Nature **560**, 209 (2018).

[102] D. J. Rizzo, G. Veber, T. Cao, C. Bronner, T. Chen, F. Zhao, H. Rodriguez, S. G. Louie, M. F. Crommie, and F. R. Fischer, Nature **560**, 204 (2018).

[103] R. M. Lutchyn, E. P. A. M. Bakkers, L. P. Kouwenhoven, P. Krogstrup, C. M. Marcus, and Y. Oreg, Nature Reviews Materials **3**, 52 (2018).

[104] A. C. Potter and P. A. Lee, Phys Rev B **83**, 184520 (2011).

[105] A. C. Potter and P. A. Lee, Phys Rev B **84**, 059906 (2011).

[106] A. M. Lobos, R. M. Lutchyn, and S. Das Sarma, Phys Rev Lett **109**, 146403 (2012).

[107] R. M. Lutchyn, T. D. Stanescu, and S. Das Sarma, Phys Rev B **85**, 140513 (2012).

[108] J. D. Sau and S. Das Sarma, Phys Rev B **88**, 064506 (2013).

[109] H.-Y. Hui, J. D. Sau, and S. Das Sarma, Phys Rev B **92**, 174512 (2015).

[110] J. Zhang, Y. Kim, E. Rossi, and R. M. Lutchyn, Physical Review B **93**, 024507 (2016).

[111] W. S. Cole, J. D. Sau, and S. Das Sarma, Phys Rev B **94**, 140505 (2016).

[112] D. E. Liu, E. Rossi, and R. M. Lutchyn, Phys. Rev. B **97**, 161408 (2018).

[113] A. E. Antipov, A. Bargerbos, G. W. Winkler, B. Bauer, E. Rossi, and R. M. Lutchyn, Phys. Rev. X **8**, 031041 (2018).

[114] B. D. Woods, T. D. Stanescu, and S. Das Sarma, Phys. Rev. B **98**, 035428 (2018).

[115] A. E. G. Mikkelsen, P. Kotetes, P. Krogstrup, and K. Flensberg, Phys. Rev. X **8**, 031040 (2018).

[116] J. Klinovaja and D. Loss, Physical Review X **3**, 011008 (2013), 1211.2739 .

[117] W. Yang, G. Chen, Z. Shi, C.-C. Liu, L. Zhang, G. Xie, M. Cheng, D. Wang, R. Yang, and D. e. a. Shi, Nature Materials **12**, 792 (2013).

[118] J. Xue, J. Sanchez-Yamagishi, D. Bulmash, P. Jacquod, A. Deshpande, K. Watanabe, T. Taniguchi, P. Jarillo-Herrero, and B. J. Leroy, Nat. Mat. **10**, 282 (2011).

[119] L. A. Ponomarenko, A. K. Geim, A. A. Zhukov, R. Jalil, S. V. Morozov, K. S. Novoselov, I. V. Grigorieva, E. H. Hill, V. V. Cheianov, V. I. Fal'Ko, K. Watanabe, T. Taniguchi, and R. V. Gorbachev, Nature Physics **7**, 958 (2011).

[120] M. Yankowitz, J. Xue, D. Cormode, J. D. Sanchez-Yamagishi, K. Watanabe, T. Taniguchi, P. Jarillo-Herrero, P. Jacquod, and B. J. Leroy, Nature Physics **8**, 382 (2012).

[121] K. S. Novoselov, A. K. Geim, S. V. Morozov, D. Jiang, Y. Zhang, S. V. Dubonos, I. V. Grigorieva, and A. A. Firsov, Science **306**, 666 (2004).

[122] K. Nomura and A. H. MacDonald, Phys. Rev. Lett. **96**, 256602 (2006).

[123] Y.-W. Tan, Y. Zhang, K. Bolotin, Y. Zhao, S. Adam, E. H. Hwang, S. Das Sarma, H. L. Stormer, and P. Kim, Phys. Rev. Lett. **99**, 246803 (2007).

[124] E. H. Hwang, S. Adam, and S. D. Sarma, Phys. Rev. Lett. **98**, 186806 (2007).

[125] S. D. Sarma, E. H. Hwang, and E. Rossi, Phys. Rev. B **81**, 161407(R) (2010).

[126] S. Das Sarma, S. Adam, E. H. Hwang, and E. Rossi, Rev. Mod. Phys. **83**, 407 (2011).

[127] S. Adam, E. H. Hwang, V. M. Galitski, and S. Das Sarma, Proceedings of the National Academy of Sciences **104**, 18392 (2007).

[128] M. M. Fogler, D. S. Novikov, and B. I. Shklovskii, Phys. Rev. B **76**, 233402 (2007).

[129] E. Rossi and S. Das Sarma, Phys. Rev. Lett. **101**, 166803 (2008).

[130] M. Polini, A. Tomadin, R. Asgari, and A. H. MacDonald, Phys. Rev. B **78**, 115426 (2008).

[131] S. Adam, S. Cho, M. S. Fuhrer, and S. Das Sarma, Phys. Rev. Lett. **101**, 046404 (2008).

[132] M. M. Fogler, Phys. Rev. Lett. **103**, 236801 (2009).

[133] E. Rossi and S. Das Sarma, Phys. Rev. Lett. **107**, 155502 (2011).

[134] Q. Li, E. H. Hwang, E. Rossi, and S. Das Sarma, Phys. Rev. Lett. **107**, 156601 (2011).

[135] D. S. L. Abergel, E. Rossi, and S. Das Sarma, Phys. Rev. B **86**, 155447 (2012).

[136] D. S. L. Abergel, M. Rodriguez-Vega, E. Rossi, and S. Das Sarma, Phys. Rev. B **88**, 235402 (2013).

[137] Q. Li, E. Hwang, and E. Rossi, Solid State Communications **152**, 1390 (2012), exploring Graphene, Recent Research Advances.

[138] J. Zhang and E. Rossi, Phys. Rev. Lett. **111**, 086804 (2013).

[139] J. Zhang, C. Triola, and E. Rossi, Phys. Rev. Lett. **112**, 096802 (2014).

[140] J. C. W. Song, A. V. Shytov, and L. S. Levitov, Phys. Rev. Lett. **111**, 266801 (2013).

[141] J. Jung, A. Raoux, Z. Qiao, and A. H. MacDonald, Phys. Rev. B **89**, 205414 (2014).

[142] J. C. W. Song, P. Samutpraphoot, and L. S. Levitov, Proc. National Acad. Sciences United States Am. **112**, 10879 (2015).

[143] J. Jung, A. M. DaSilva, A. H. MacDonald, and S. Adam, Nature Communicationsxxxx **6**, 6308 (2015).

[144] J. Jung, E. Laksono, A. M. DaSilva, A. H. MacDonald, M. Mucha-Kruczyński, and S. Adam, Phys. Rev. B **96**, 085442 (2017).

[145] L. Britnell, R. V. Gorbachev, R. Jalil, B. D. Belle, F. Schedin, A. Mishchenko, T. Georgiou, M. I. Katsnelson, L. Eaves, and S. V. e. a. Morozov, Science **335**, 947 (2012).

[146] B. Hunt, J. D. Sanchez-Yamagishi, A. F. Young, M. Yankowitz, B. J. LeRoy, K. Watanabe, T. Taniguchi, P. Moon, M. Koshino, and P. e. a. Jarillo-Herrero, Science **340**, 1427 (2013).

[147] L. A. Ponomarenko, R. V. Gorbachev, G. L. Yu, D. C. Elias, R. Jalil, A. A. Patel, A. Mishchenko, A. S. Mayorov, C. R. Woods, and J. R. e. a. Wallbank, Nature **497**, 594 (2013).

[148] C. R. Dean, L. Wang, P. Maher, C. Forsythe, F. Ghahari, Y. Gao, J. Katoch, M. Ishigami, P. Moon, and M. e. a. Koshino, Nature **497**, 598 (2013).

[149] C. R. Woods, L. Britnell, A. Eckmann, R. S. Ma, J. C. Lu, H. M. Guo, X. Lin, G. L. Yu, Y. Cao, and R. V. e. a. Gorbachev, Nature Physics **10**, 451 (2014).

[150] Y. Zhang, Y.-W. Tan, H. L. Stormer, and P. Kim, Nature **438**, 201 (2005).

[151] A. H. Castro Neto, F. Guinea, N. M. R. Peres, K. S. Novoselov, and A. K. Geim, Rev. Mod. Phys. **81**, 109 (2009).

[152] L. C. Campos, V. R. Manfrinato, J. D. Sanchez-Yamagishi, J. Kong, and P. Jarillo-Herrero, Nano Letters **9**, 2600 (2009).

[153] H. Zheng, Z. F. Wang, T. Luo, Q. W. Shi, and J. Chen, Phys. Rev. B **75**, 165414 (2007).

[154] L. Brey and H. A. Fertig, Phys. Rev. B **73**, 235411 (2006).

[155] H. Raza and E. C. Kan, Physical Review B **77**, 245434 (2008).

[156] B. Sahu, H. Min, A. H. MacDonald, and S. K. Banerjee, Physical Review B **78**, 045404 (2008).

[157] G. Lee and K. Cho, Phys. Rev. B **79**, 165440 (2009).

[158] H. Lee, Y.-W. Son, N. Park, S. Han, and J. Yu, Phys. Rev. B **72**, 174431 (2005).

[159] M. Kan, J. Zhou, Q. Sun, Q. Wang, Y. Kawazoe, and P. Jena, Phys. Rev. B **85**, 155450 (2012).

[160] P. Giannozzi, S. Baroni, N. Bonini, M. Calandra, R. Car, C. Cavazzoni, D. Ceresoli, G. L. Chiarotti, M. Cococcioni, I. Dabo, A. D. Corso, S. de Gironcoli, S. Fabris, G. Fratesi, R. Gebauer, U. Gerstmann, C. Gougoussis, A. Kokalj, M. Lazzeri, L. Martin-Samos, N. Marzari, F. Mauri, R. Mazzarello, S. Paolini, A. Pasquarello, L. Paulatto, C. Sbraccia, S. Scandolo, G. Sclauzero, A. P. Seitsonen, A. Smogunov, P. Umari, and R. M. Wentzcovitch, Journal of Physics: Condensed Matter **21**, 395502 (2009).

[161] D. Soriano and J. Fernández-Rossier, Phys. Rev. B **85**, 195433 (2012).

[162] Y.-W. Son, M. L. Cohen, and S. G. Louie, Nature **444**, 347 (2006).

[163] J. Yu and W. Guo, The Journal of Physical Chemistry Letters **4**, 951 (2013).

[164] X. Qian, J. Liu, L. Fu, and J. Li, Science **346**, 1344 (2014), http://science.sciencemag.org/content/346/6215/1344.full.pdf .

[165] J. A. Reyes-Retana and F. Cervantes-Sodi, Scientific Reports **6** (2016), 10.1038/srep24093.

[166] E. J. Sie, C. M. Nyby, C. D. Pemmaraju, S. J. Park, X. Shen, J. Yang, M. C. Hoffmann, B. K. Ofori-Okai, R. Li, and A. H. e. a. Reid, Nature **565**, 61 (2019).

[167] V. Fatemi, S. Wu, Y. Cao, L. Bretheau, Q. D. Gibson, K. Watanabe, T. Taniguchi, R. J. Cava, and P. Jarillo-Herrero, Science **362**, 926 (2018), http://science.sciencemag.org/content/362/6417/926.full.pdf .

[168] N. R. Pradhan, S. Talapatra, M. Terrones, P. M. Ajayan, and L. Balicas, IEEE Nanotechnology Magazine **11**, 18 (2017).

[169] S.-J. An, Y. H. Kim, C. Lee, D. Y. Park, and M. S. Jeong, Scientific Reports **8**, 12957 (2018).

[170] Y. Li, A. Chernikov, X. Zhang, A. Rigosi, H. M. Hill, A. M. van der Zande, D. A. Chenet, E.-M. Shih, J. Hone, and T. F. Heinz, Phys. Rev. B **90**, 205422 (2014).

[171] S. Onishi, M. M. Ugeda, Y. Zhang, Y. Chen, C. Ojeda-Aristizabal, H. Ryu, S.-K. Mo, Z. Hussain, Z.-X. Shen, M. F. Crommie, and A. Zettl, physica status solidi (b) **253**, 2396, https://onlinelibrary.wiley.com/doi/pdf/10.1002/pssb.201600235 .

[172] Y. Yang, S. Fang, V. Fatemi, J. Ruhman, E. Navarro-Moratalla, K. Watanabe, T. Taniguchi, E. Kaxiras, and P. Jarillo-Herrero, Phys. Rev. B **98**, 035203 (2018).

[173] E. Navarro-Moratalla and P. Jarillo-Herrero, Nature Physics **12**, 112 EP (2016).

[174] J. D. Sau, R. M. Lutchyn, S. Tewari, and S. Das Sarma, Phys. Rev. Lett. **104**, 040502 (2010).

[175] R. M. Lutchyn, J. D. Sau, and S. Das Sarma, Phys. Rev. Lett. **105**, 077001 (2010).

[176] C. Nayak, S. H. Simon, A. Stern, M. Freedman, and S. Das Sarma, Rev. Mod. Phys. **80**, 1083 (2008).

[177] P. Cui, J.-H. Choi, W. Chen, J. Zeng, C.-K. Shih, Z. Li, and Z. Zhang, Nano Letters **17**, 1097 (2017).

[178] M. Gibertini and N. Marzari, Nano Letters **15**, 6229 (2015), pMID: 26291826, https://doi.org/10.1021/acs.nanolett.5b02834 .

[179] X. Liu, T. Xu, X. Wu, Z. Zhang, J. Yu, H. Qiu, J.-H. Hong, C.-H. Jin, J.-X. Li, X.-R. Wang, L.-T. Sun, and W. Guo, Nature Communications **4**, 1776 EP (2013), article.

[180] A. Kumar and P. Ahluwalia, Journal of Alloys and Compounds **587**, 459 (2014).

[181] R.-L. Chu, G.-B. Liu, W. Yao, X. Xu, D. Xiao, and C. Zhang, Phys. Rev. B **89**, 155317 (2014).

[182] Y. Chen, P. Cui, X. Ren, C. Zhang, C. Jin, Z. Zhang, and C.-K. Shih, Nature Communications **8**, 15135 EP (2017), article.

[183] W. Zan, Z. Zhang, Y. Yang, X. Yao, S. Li, and B. I. Yakobson, Nanotechnology **30**, 075701 (2018).

[184] A. C. Dias, F. Qu, D. L. Azevedo, and J. Fu, Phys. Rev. B **98**, 075202 (2018).

[185] T. Chen, G. Hao, G. Wang, B. Li, L. Kou, H. Yang, X. Zheng, and J. Zhong, 2D Materials **6**, 025002 (2019).

[186] S. Li, Y.-C. Lin, W. Zhao, J. Wu, Z. Wang, Z. Hu, Y. Shen, D.-M. Tang, J. Wang, Q. Zhang, H. Zhu, L. Chu, W. Zhao, C. Liu, Z. Sun, T. Taniguchi, M. Osada, W. Chen, Q.-H. Xu, A. T. S. Wee, K. Suenaga, F. Ding, and G. Eda, Nature Materials **17**, 535 (2018).

[187] H. J. Monkhorst and J. D. Pack, Phys. Rev. B **13**, 5188 (1976).

[188] G. Z. Magda, X. Jin, I. Hagymási, P. Vancsó, Z. Osváth, P. Nemes-Incze, C. Hwang, L. P. Biró, and L. Tapasztó, Nature **514**, 608 (2014).

[189] J. Jung, T. Pereg-Barnea, and A. H. MacDonald, Phys. Rev. Lett. **102**, 227205 (2009).

[190] R. Winkler, *Spin-orbit coupling effects in two-dimensional electron and hole systems* (Springer, 2010).

[191] Y. S. Gani, D. S. L. Abergel, and E. Rossi, Phys. Rev. B **98**, 205415 (2018).

[192] Y. S. Gani, H. Steinberg, and E. Rossi, arXiv e-prints , arXiv:1903.00475 (2019), arXiv:1903.00475 [cond-mat.mes-hall] .

VITA

Yohanes Satrio Gani

Yohanes Satrio Gani was born on November 14, 1986 in Bandung, West Java, Indonesia. He began his formal education in 1992 at Santo Yusup 2 elementary school in Bandung, Indonesia. From his youth, he was always curious about science and spent a lot of time understanding how things work. In 1998, he entered Santa Angela Middle and High school in Bandung, Indonesia. He was fortunate to have a wonderful high school physics teacher who inspired him to delve into physics in college. In 2004, he entered Bandung Institute of Technology in Bandung, Indonesia where he majored in Physics. Beside, he also actively taught science for high school students. After graduation from college, he worked for an education company where he became a physics lecturer and book editor. He continued his advanced degree at College of William & Mary, Virginia, USA in Fall 2011. In 2013, he joined Dr. Enrico Rossi's group investigating the electronic structure of two-dimensional systems. Under the guidance and supervision of Dr. Rossi, he researched many fascinating topics that are of current interest in the condensed matter field.